

博士論文

論文題目 Detection of Angular
Momentum Transfer from a Single Photon
to a Single Electron Spin in a Lateral
Double Quantum Dot
(横型二重量子ドットにおける単一光子偏光
から単一電子スピンへの角運動量転写の実証)

氏名 藤田 高史

Abstract of the Dissertation

Detection of Angular Momentum Transfer from a Single Photon to a Single Electron Spin in a Lateral Double Quantum Dot

by

Takafumi Fujita

The information transfer from a photon to an electron spin in semiconductors is predicted to forward the realization of quantum computation. Gate defined lateral quantum dots is an attractive platform in this sense since the electrical single and two quantum bit (qubit) gate operations have been demonstrated only in this system. However, realization of quantum media conversion is limited up to the single photon to charge conversion due to the large disturbance of electrostatic potentials by the irradiation of light. It is still challenging to achieve high visibility of single-shot photoelectron spin measurements and the detection of angular momentum transfer from a single photon polarization to a single photoelectron spin.

This work presents the detection of single photoelectron spins excited by single circularly polarized photons and confirm the optical selection rules associated with the conversion. Double heterostructure GaAs quantum wells (QWs) were prepared to selectively excite electron spins from the discrete heavy and light hole bands. The QWs are also designed to meet the requirement of the coherent transfer scheme. The out of plane electron g -factors were measured from resistively detected electron spin resonance experiments and we determined the well width implying the near zero in-plane electron g -factor.

To overcome the disturbance due to light irradiation, a double quantum dot (DQD) was formed on the chosen QW. DQDs are preferable for high visibility detection of spin states using Pauli spin blockade. Additionally, under

a resonant condition the repetitive signal of inter-dot electron tunneling offers non-destructive single photoelectron detection. Tuning the DQD to the few electron regime with lowered tunneling rates realizes real-time charge sensing and observation of single charge and spin dynamics within the DQD. The robust detection scheme helped the detection of single photoelectrons that were selectively excited from the heavy hole band.

Distinguishing between two electron spin signals in real-time measurements is necessary in order to combine our scheme of photoelectron trapping in a resonant condition. However, the magnetic field dependence of the real-time inter-dot tunneling has not been investigated before. We measured the $(1,1) \rightarrow (0,2)$ inter-dot tunneling times and obtained characteristic time constants representing the parallel and anti-parallel spin configurations in a finite magnetic field. We outline the possible mechanisms that determine the spin dependent tunneling times and elucidate that the electron g -factors can be quantitatively discussed in this tunneling regime. With sufficient gate voltage tuning, high distinguishability of the spin states is realized.

Finally we combine our techniques of photoelectron trapping in a QW and the spin detection in a DQD. Two distinct photoelectron spin signals are resolved between subsequent inter-dot tunneling or blocked tunneling upon single photoelectron trapping corresponding to the up- or down-spin detection depending on the magnetic field direction. By varying the incident photon polarization and taking the statistics of measured spins for each polarization, we confirmed that the conversion to electron spins correspond to the selection rules. Our result verified the classical angular momentum transfer between single quanta. The detection of angular momentum transfer to a single electron spin is a prominent step in this field towards future realization of the coherent transfer and the study of photon-spin entanglement physics.

Table of Contents

1	Introduction	1
1.1	General introduction	1
1.2	Purpose of this study	3
1.3	Dissertation outline	4
2	Theoretical background of angular momentum transfer	7
2.1	Optical selection rules of GaAs	8
2.1.1	Band structures of GaAs	8
2.1.2	Optical selection rules	9
2.2	Quantum wells	12
2.2.1	Selective spin excitation with polarization	12
2.2.2	Landé g -factor in quantum wells	14
2.2.3	Towards coherent transfer between quantum bits	18
3	Basics of Quantum dots	25
3.1	Single quantum dots	26
3.2	Double quantum dots	28
3.2.1	Charge transport in a double dot	28
3.2.2	Pauli spin blockade	34
3.3	Charge sensing and spin detection techniques	38
3.3.1	Charge sensing	39
3.3.2	Single-shot readout of electron spins	42
3.3.3	Non-destructive spin state measurement	48

TABLE OF CONTENTS

4	Preceding studies on single photon detection	51
5	Experimental conditions	55
5.1	Characterization of quantum wells	55
5.1.1	Wafer structures and band calculations	56
5.1.2	2DEG electron spins	57
5.1.3	Summary of wafer profiles	61
5.2	Lateral quantum dot devices	63
5.3	Electronic and optical measurement systems	65
6	Single photoelectron trapping in a double quantum dot	73
6.1	Photoelectron trapping process	74
6.2	Non-destructive photon detection in a double quantum dot . . .	75
6.3	Photoelectron trapping in a double heterostructure device . . .	81
6.3.1	Single photon detection	82
6.3.2	Wavelength selectivity of photon response	85
6.3.3	Initial evidence of photoelectron spin detection	87
6.4	Conclusions	88
7	Spin dependent tunneling in a double quantum dot	89
7.1	Pauli spin blockade	89
7.2	Real-time measurement of spin blockade	91
7.3	Analysis of real-time spin blockade	95
7.3.1	Evaluation of spin dependent tunneling times	95
7.3.2	Distinguishability of electron spins	101
7.4	Conclusions	102
8	Transfer of single photon polarization to single electron spin	105
8.1	Single photoelectron spin detection	106
8.2	Angular momentum transfer between single quanta	109
8.3	Discussions on single photon polarization detection	111
8.4	Conclusions	114

9 Summary and future prospects	115
A <i>g</i>-factors in quantum dots	119
A.1 <i>g</i> -factor evaluation from Kondo effect	119
A.2 Nuclear spin effect in double quantum dots	126
B Calculation of photon absorption	129
References	135

Acknowledgements

Any accomplishment made during my Ph.D course would have never been realized on my own without the contributions of many other people.

First I would like to greatly thank my supervisor Prof. Seigo Tarucha for giving me the great opportunity to do research in his lab for many years. It was a valuable time to make discussions and perform experiments in such a magnificent environment. In contrast to his devoting to such a large group, he gave me a large amount of support. His view points enlightened my way not only on physics but on skills of writing and presenting, which he was attentive for every piece of work, offering me invaluable experiences I had never imagined.

I would like to express deep gratitude for Dr. Akira Oiwa. He constantly kept in touch with all my research progress but even more with the complications occurring all around. He encouraged me whenever I was becoming negative to the results or having technical difficulty, by thinking together and never giving up. I enjoyed my research time thanks to his deep and gentle way of advising me. He gave me the biggest encouragement to continue with my research life.

Dr. Giles Allison helped me on the quantum well project while he had other projects running in parallel. He was the main person helping me with my English and was always a gentleman even though I made quite a lot of irritating mistakes. Dr. Marcus Larsson joined our group a few years ago and quickly absorbed our measurement knowhow, including my messy setup. It was comfortable working together with his calm character while giving us sharp thoughts. Mr. Haruki Kiyama advised me as an elder member in the group. Talk on optics with him often revealed significant points in the discussion. Thanks to

TABLE OF CONTENTS

these colleagues I had a good time being a member in the photon-group.

I would like to thank my former colleagues, Mr. Kazuhiro Morimoto for fabricating the devices shown for my main results and researching together being an excellent junior fellow, researcher Mr. Soichiro Teraoka for setting up the fridges and instructing about crafting, and Mr. Yosuke Sato, our latest fellow, who helped me continue the measurement while I was writing this thesis.

I am also really grateful to my brilliant colleagues. Mr. Jun Yoneda was a refreshing and uplifting guy. He was always positive and impressed me with his way of thinking in any kind of affairs. It was very stimulating for me while spending time alongside of him from the early university days. Mr. Shintaro Takada was always bright and energetic. He often made it easier for me to overcome my weakness, mainly giving presentations and to play soccer. It was an enjoyable time learning together for 6 years.

Last, but not least, I would like to dedicate this work to my family and friends. Especially my family supported me in both mental and health aspects. Here, I would like to thank them all.

Tokyo, February 2014

Takafumi Fujita

Chapter 1

Introduction

1.1 General introduction

Theory of quantum mechanics has played a roll in the advancement of semiconductor electronics that is vital to the modern society. In research fields these technologies can be utilized to control single quanta of fundamental particles. Detailed studies on the quantum mechanical features of these fundamental particles have revealed their potential to further advance the existing technologies. Among many of the offered physical systems, electron systems and photon systems have an advantage on the possible compatibility to the present nanoscale electronics. As the investigation of these particles has further advanced, a more fundamental physical quanta has been focused on, namely their angular momentum: the spin of an electron and the polarization of a photon.

As electronic devices become smaller down to nanoscales, the effect of individual spins becomes crucial in the function of magnetic elements. Optical measurement of this magnetism is currently applied in memories or sensors. When we consider integration of both optically and electrically accessible devices, faster and more accurate measurement of electron spins as well as photon angular momentum is preferable. For instance silicon has a well established fine structure fabrication process, however, the optical response tends to be slow compared to the spin relaxation rate due to its indirect optical transition.

Electrical spin detection could offer measurement times mainly determined by the electronics. Therefore electrical measurement of the photon angular momentum is an advantage towards adopting the well established Si-based fine structured electronics that is crucial for scalability and future industrial application. Furthermore, these fundamental particles present another application towards the development of quantum information technology.

The next extension of information technology is believed to be the quantum information where a quantum system stores and encodes the information. Electron spin and photon polarization allow the simplest quantum system consisting a natural two level system that represent the information unit of a so-called quantum bit (qubit). Since the respective qubit systems have the distinct physical properties they have their own specialties and shortcomings. Photons have weak interaction with the environment and are therefore suitable for long distant transport of information, however, for the same reason they are difficult to be stored and processed effectively within a desired time frame. On the other hand electron spins confined in semiconductors have excellent capability for information processing because they strongly interact with each other. Quantum information transfer from photon qubits to electron spin qubits is one way for utilizing both advantages of transportability and operation ability of qubits. Detection of a single spin created by a polarized photon is a primary step towards verification of quantum information transfer.

Detecting single polarized photons is also an essential ingredient in certain functional devices in quantum communication. For instance, a quantum repeater was proposed to extend the distance of a single photon carrying information. Due to the no cloning theorem in quantum mechanics, amplification of a single qubit is not possible. However, using a chain of entangled photon pairs, loss of photons could be avoided and single qubit information could be sent over longer distances. A quantum repeater creates the needed entanglement by manipulating and detecting the electron spin qubits that were transformed from photon qubits. This kind of technical requirement further motivates the study on the detection of a single polarized photon that is transferred to a single

electron spin.

1.2 Purpose of this study

Electron spins in semiconductor quantum dots (QDs) are of interest in current research partly because of their possible application to classical information systems [1] and quantum information systems [2]. Especially, the electron spins confined in GaAs based quantum dots have been extensively researched and the usefulness of spins for quantum information has been revealed such as sufficiently long coherence time as a quantum memory [3] and full single qubit manipulation [4, 5] along with two qubit gate operations [6, 7]. In addition, semiconductors are optically active materials subject to certain selection rules that have already been extensively studied [8].

In terms of using the photon to spin conversion for absolutely safe quantum communication [9], a quantum repeater was proposed [10, 11] to extend the current limitation of photon information transmission length [12]. Up to now several experiments demonstrated entanglement of optical qubits with trapped ions [13], atoms [14, 15], solid state systems such as InAs self-assembled QDs [16–19] and NV centers [20–22]. However they suffer from the time needed to create the entanglement through post selection of photons which make them unsuitable for quantum repeaters. Compared to these devices, laterally defined QDs are suitable types of devices that are capable of concentrating and scaling up the desired functions by suitable fabrication [23]. Indeed, this is the only system in which two electron spin entanglement and spin qubit operations have been demonstrated. For this purpose GaAs based lateral QDs are suitable for combining its optically active properties and functionality of operations on electron spins [24]. Research in the physics of electron-photon entanglement generation is also interesting.

Regarding these backgrounds, our group has been investigating a fundamental technology for transferring quantum states from individual photon polarization to individual electron spin in lateral QDs. Coherent angular momentum

transfer was previously demonstrated between ensembles of photons to ensembles of spins in a quantum well (QW) [25, 26]. The two dimensional system that they used is suitable for combining with the lateral QDs. Several demonstrations of single photoelectron trapping have been reported [27, 28] towards transfer between single quanta, imperative for future quantum information network, but these electrons have still not been detected in a controlled manner. The control of the trapped photoelectrons is an important ingredient for storage and operation of the transferred quantum information [29]. Viewing these preceding studies we set the following steps to accomplish the transfer.

- (i) Energy transfer from a single photon to a single electron
- (ii) Angular momentum transfer from a single photon polarization to a single electron spin
- (iii) Superposition state transfer from a single photon polarization to a single electron spin

The first step was earlier realized by A. Pioda *et al.* [30] here in a controlled manner, and the second step was partly demonstrated by T. Asayama *et al* [31]. Both preceding works have been done using a conventional single heterostructure that are not adaptable for the coherent transfer. This dissertation shows detailed research continued from this progress, starting from the sophistication of the first step to straightforward verification of the second step using both single and double heterostructures (QW). The latter is suitable for the third step. Additional discussion is made foreseeing the third step.

1.3 Dissertation outline

This dissertation discusses backgrounds and experiments towards the detection of angular momentum transfer from single circularly polarized photons to single electron spins.

Chapter 2 introduces the theoretical background on the optical transitions of spins in a GaAs heterostructure. Chapter 3 provides the background on lateral QDs with the recent progress towards single shot electron spin detection. Chapter 4 shows preceding experiments of single photon detection measurements in lateral QDs that may be helpful in understanding the experiments described in the following chapters.

Chapter 5 briefly summarizes the measurements on GaAs QWs partly about the selective spin excitation and partly about g -factor engineering towards future coherent transfer demonstration. Chapter 6 discusses measurements of single photon detection using a new scheme with a double QD (DQD), which is more reliable than preceding measurements with single QDs. Chapter 7 explains our newly developed single-shot spin detection scheme utilizing real-time measurement of spin blockade. Chapter 8 presents our main results on the photoelectron spin detection. By combining the arguments in the previous chapters, we discuss the evidence of angular momentum transfer from a single circularly polarized photon to a single electron spin. Chapter 9 summarizes and discusses the future prospects of the study.

Additional information on the electron g -factor evaluation in QDs are described in Appendix A. Simulation on the photon propagation through the sample structures are shown in Appendix B.

Chapter 2

Theoretical background of angular momentum transfer

The research of III-V semiconductors, especially GaAs has attracted great interest in terms of both optical and transport properties of electron and hole systems. In comparison with Si-based semiconductors, GaAs-based semiconductors have several striking features such as direct band gap at $k = 0$ in Brillouin zone, bulk inversion asymmetry with zinc blende crystal structure, and the presence of ensemble nuclear spins originating from certain amount of Ga and As isotopes with $3/2$ spin. Further studies and applications of these features can be promoted for low-dimensional carrier systems as prepared using crystal growth techniques such as Molecular Beam Epitaxy (MBE), and nanolithography. One of the most commonly used approaches for investigating the low dimensional electron system in semiconductors is to play with the quantum well (QW) structures made by MBE. GaAs QWs are typical systems consisted of three neighboring layers in a sandwiched structure (AlGaAs/GaAs/AlGaAs). The wider band gap of the AlGaAs barriers compared to the GaAs layer in between leads to the confining potential for electrons and holes, and well-designed wafer structures provide high mobility two-dimensional electron/hole systems.

The confinement of carriers is not only of importance for the fundamental study of quantum mechanics in semiconductors, but also for the engineering

of physical quantities such as spin-orbit coupling constant and g -factor which play crucial roles for future optical and electrical applications with spin or angular momentum degrees of freedom. On the other hand, QWs are suitable for optical measurements focusing on exciton dynamics. For future application of spintronics and quantum information networks, QW systems provide basic tools for optical spin manipulation, since the confining effect lifts the degeneracy of the heavy hole (HH) and light hole (LH) bands with different selection rules, and therefore pure up- and down-spin states of electrons can be readily prepared by circularly polarized light with 100% certainty.

2.1 Optical selection rules of GaAs

2.1.1 Band structures of GaAs

The band structure of GaAs consists of two-fold degenerate conduction bands with s-type orbital, four-fold valence bands (the LH and HH levels) and two-fold split-off valence bands with p-type orbital. As shown in Figure 2.1, the conduction band minimum and the valence band maximum exist at the Γ point of the Brillouin zone, and the split-off band is separated from the LH and HH bands by energy Δ . This splitting is explained as follows. In the vicinity of the Γ point, the electron wave function of the valence bands forms a p-type orbital with finite angular momentum $l = 1$. Taking the spin-orbit interaction term ($H_{SO} \propto \mathbf{l} \cdot \mathbf{s}$) into account, the additional term $\mathbf{l} \cdot \mathbf{s}$ is decomposed in the following way:

$$\mathbf{l} \cdot \mathbf{s} = \frac{1}{2}[(\mathbf{l} + \mathbf{s})^2 - \mathbf{l}^2 - \mathbf{s}^2] = \frac{1}{2}(\mathbf{j}^2 - \mathbf{l}^2 - \mathbf{s}^2), \quad (2.1)$$

where \mathbf{j} is a total angular momentum operator. As $\mathbf{l} \cdot \mathbf{s}$ commutes with \mathbf{j}^2 and j_z , six-fold p-type bands split into four-fold bands $|j = \frac{3}{2}, j_m = \pm \frac{3}{2}\rangle$ and $|j = \frac{3}{2}, j_m = \pm \frac{1}{2}\rangle$ corresponding to the HH and LH bands, and the two-fold split-off bands $|j = \frac{1}{2}, j_m = \pm \frac{1}{2}\rangle$. Note that the energy splitting width directly

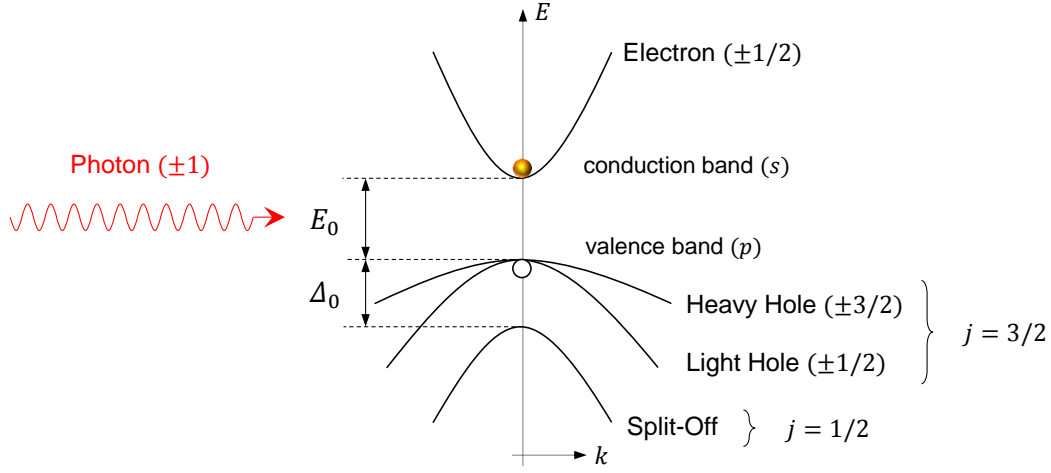


Figure 2.1: A schematic picture of the band structure of GaAs. The conduction band is separated from the top of the valence band by the band gap E_0 , and the HH and the LH bands are degenerate at $k = 0$. The split-off band is below the heavy and LH bands, and their energy spacing is defined by the spin-orbit energy Δ_0 .

represents the spin-orbit coupling strength and is about 0.34 eV and 0.30 eV for bulk GaAs and AlAs respectively [32].

The major difference between the LH and the HH bands is seen in the effective mass near Γ point. Furthermore, due to the size quantization effect, the confinement in one direction lifts the degeneracy of the LH and the HH bands at $k = 0$. The separation of these bands is critical for opto-electrical application, since optical orientation for either the LH excitation or the HH excitation should be independently accessible by tuning the incident laser wavelength.

2.1.2 Optical selection rules

One of the most effective methods to excite spin-polarized carriers in semiconductors is to use the selection rules [8]. The selection rules determine the excitation or recombination probability of electron-hole spin states. In the example of GaAs, s-type orbital of the conduction band and p-type orbital of the light and HH valence bands can be expressed using the following Bloch

functions:

$$\Psi_{km}^c = u_m e^{i\mathbf{k}\cdot\mathbf{r}}, m = \pm\frac{1}{2}, \quad (2.2)$$

$$\Psi_{kj_z}^v = e^{i\mathbf{k}\cdot\mathbf{r}} \sum_{\mu} \chi_{j_z\mu}(\mathbf{k}) u_{\mu}^{(3/2)}, j_z = \pm 1/2, \pm 3/2, \quad (2.3)$$

where $u_{\pm 1/2}$ corresponds to $\pm 1/2$ spin, and $j_z = \pm 3/2$, and $j_z = \pm 1/2$ corresponds to the HH, and LH bands, respectively. By expressing the wave function with the symmetry of s, p_x, p_y, p_z as S, X, Y, Z, u is explicitly presented as follows,

$$\begin{aligned} u_{1/2} &= S \uparrow, u_{-1/2} = S \downarrow, \\ u_{3/2}^{(3/2)} &= -\frac{1}{2}\sqrt{2}(X + iY) \uparrow, \\ u_{-3/2}^{(3/2)} &= -\frac{1}{2}\sqrt{2}(X - iY) \downarrow, \\ u_{1/2}^{(3/2)} &= \frac{1}{3}\sqrt{3} \left[-\frac{1}{2}\sqrt{2}(X + iY) \downarrow + \sqrt{2}Z \uparrow \right], \\ u_{-1/2}^{(3/2)} &= \frac{1}{3}\sqrt{3} \left[-\frac{1}{2}\sqrt{2}(X - iY) \downarrow + \sqrt{2}Z \downarrow \right]. \end{aligned} \quad (2.4)$$

Here the correspondence principle is a useful tool for calculating the direct interband transition probability with circularly polarized photons transferring angular momentum of $l_z = \pm 1$. The correspondence between a quantum transition from state a to state b and a classical dipole with frequency $\omega_{ab} = (E_b - E_a)/\hbar$ indicates that the amplitude of the dipole moment is equal to the transition matrix element

$$D_{ab} = \langle b | \hat{D} | a \rangle, \quad (2.5)$$

where \hat{D} is the dipole moment operator. To deduce the excitation probability, one needs to bear the following things in mind; (i) the angular momentum needs to be conserved in the transition, (ii) the only non-zero matrix elements

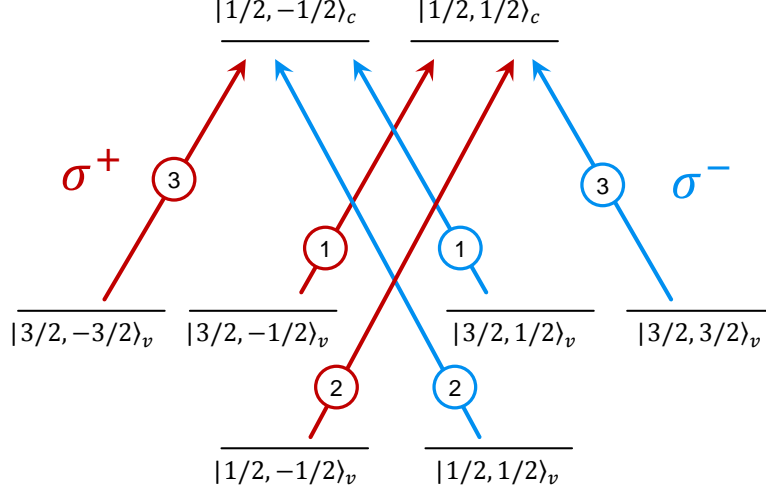


Figure 2.2: A schematic view of the selection rules in GaAs. Blue and red arrows depict the permitted transition with polarized light σ^+ and σ^- respectively. The relative excitation probabilities for different light polarizations are noted in blue and red circles.

are $\langle S|D_x|X\rangle = \langle S|D_y|Y\rangle = \langle S|D_z|Z\rangle$.

Table 2.1: Matrix elements of the dipole moment. λ, μ are the unit vectors perpendicular to the propagation axis. \mathbf{v} is the unit vector along the propagation axis.

	ValenceBand(v)	ConductionBand(c)	
		1/2	-1/2
hh	3/2	$-\sqrt{1/2}(\lambda + i\mu)$	0
	-3/2	0	$\sqrt{1/2}(\lambda - i\mu)$
lh	1/2	$\sqrt{2/3}\mathbf{v}$	$-\sqrt{1/6}(\lambda + i\mu)$
	-1/2	$\sqrt{1/6}(\lambda - i\mu)$	$\sqrt{2/3}\mathbf{v}$

Degree of polarization

Assume that one excites the electron from the degenerate light and HH bands with σ^\pm circularly polarized photons. The dipole operator can be expressed as $\propto (X \pm iY) \propto Y_1^{\pm 1}$ where Y_l^m is the spherical harmonic function. With σ^+

polarized light the ratio of excitation probabilities from the LH and the HH bands is calculated as:

$$\frac{P_{\text{HH-c}}}{P_{\text{LH-c}}} = \frac{|\langle 1/2, -1/2 | Y_1^1 | 3/2, -3/2 \rangle|^2}{|\langle 1/2, 1/2 | Y_1^1 | 3/2, -1/2 \rangle|^2} = 3, \quad (2.6)$$

which implies three times larger probability of creating electron spin -1/2 states compared to 1/2 states. The relative excitation probability for the respective valence bands is summarized in Figure 2.2.

Similarly we can calculate the degree of electron-spin polarization P_S . For instance for σ^+ polarized light P_S is calculated as:

$$P_S \equiv \left| \frac{N_+ - N_-}{N_+ + N_-} \right| \quad (2.7)$$

$$= \frac{|\langle \frac{1}{2}, \frac{1}{2} | Y_1^1 | \frac{3}{2}, -\frac{1}{2} \rangle|^2 - |\langle \frac{1}{2}, -\frac{1}{2} | Y_1^1 | \frac{3}{2}, -\frac{3}{2} \rangle|^2}{|\langle \frac{1}{2}, \frac{1}{2} | Y_1^1 | \frac{3}{2}, -\frac{1}{2} \rangle|^2 + |\langle \frac{1}{2}, -\frac{1}{2} | Y_1^1 | \frac{3}{2}, -\frac{3}{2} \rangle|^2} = 0.5, \quad (2.8)$$

where $N_+(N_-)$ is the number of electrons with spin up (down), respectively.

2.2 Quantum wells

2.2.1 Selective spin excitation with polarization

We have seen that the optical excitation of bulk GaAs with circularly polarized light can create spin polarized electrons in the conduction band in a degree of polarization $P_S = 0.5$. When the system becomes two-dimensional such as in QWs, the HH and LH state degeneracy is lifted due to the difference of effective mass, which can be used to selectively excite individual hole states. The benefits of using the HH excitation is that it has a larger absorption efficiency and, since it is the ground state, no mixing occurs with other bands. This results in $P_S \approx 1$ for large range of QW parameters. On the other hand, the LH states can create a superposition state of electron spins, needed for coherent transfer that is currently not possible with the HH states as explained later on.

The electron spin polarization created from various hole states were extensively studied in QW structures. The various origins of polarization effects were studied by tuning the well widths to vary the confinement strength. Tuning the well width is also a conventional strategy to control the g -factor as an important parameter in spintronics.

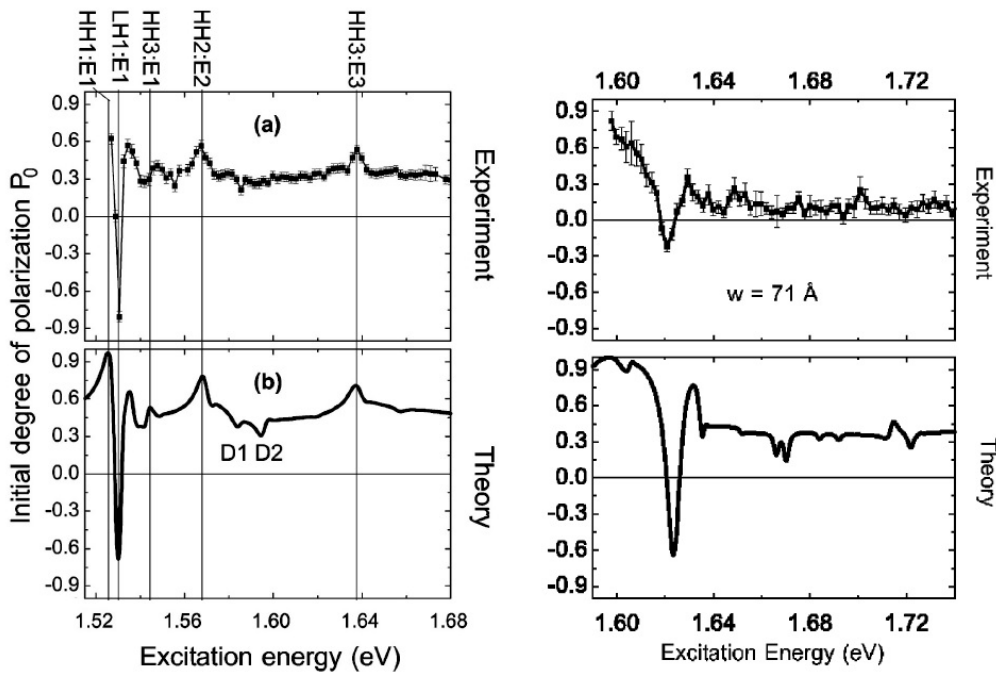


Figure 2.3: (a) Measured and (b) calculated initial degree of spin polarization P_0 as a function of excitation energy of the 198-Å-wide GaAs/AlAs QW. The vertical lines label the resonances in (a) and (b) according to the dominantly contributing electron (E) and hole (LH or HH) subbands. (Right) Degree of spin polarization in a well width of 71 Å [33].

The optically excited spins from the HH state can be polarized with a degree of spin polarization over 0.9 [33, 34] (Fig. 2.3). The reason of reduction from 1 mainly comes from spin relaxation before the detection which is merely an artifact of the detection scheme. For the excitation from the LH state, additional reduction is observed originating from the exciton continuum that could have an opposite effect on the spin polarization [35]. The latter is a crucial matter for

pure spin injection however tuning is possible with variation of well width [36], magnetic field [37] and electric field [38] to suitable avoid the effect of exciton states. Furthermore, in lower-dimensional systems such as in a quantum dot, holes can be extracted under an intense electric field to leave only the electron inside the dot with its spin conserved [39].

2.2.2 Landé g -factor in quantum wells

The Landé g -factor is one of the most important material parameters to characterize spin-related phenomena in semiconductors. The value of the g -factor in III-V semiconductor systems often differs from that of a free electron in vacuum, where $g_e = 2$. For example bulk GaAs, AlAs, InAs and InSb show the electron g -factor value of -0.44, 1.52, -14.9 and -51.56, respectively. The deviation from the free electron value was theoretically explained by L. M. Roth *et al.* [40] using $\mathbf{k} \cdot \mathbf{p}$ perturbation theory. The authors deduced the general formula of the electron g -factor as a function of energy band gap E_g at the Γ point:

$$g_e = 2 - \frac{2}{3} \frac{E_p \Delta}{E_g (E_g + \Delta)}, \quad (2.9)$$

where E_p is the energy of interband momentum matrix element and Δ the spin-orbit energy splitting. This equation implies that the g -factor of conduction band electrons are indirectly affected by the spin-orbit interaction via orbital interband mixing with the valence band, and narrower band gap and stronger spin-orbit interaction result in a larger negative correction to the g -factor from 2.

The electron or hole g -factor is also strongly influenced by the quantum confinement effect in low-dimensional electron systems. A typical example is the QW structure in which the g -factor is determined by material composition and confinement energy. Intuitive understanding of the g -factor modulation in a QW is explained in the following way. In the case of a typical AlGaAs/GaAs/AlGaAs QW, the wave function of the confined electron or hole is not only in the GaAs

layer but also penetrates into the AlGaAs walls which has a positively larger g -factor compared to GaAs. Owing to this penetration of wave function, the averaged effective g -factor of carriers is the admixture of the g -factor values in the well and wall materials. Furthermore, in lower-dimensional systems such as a quantum dot, further deviation of the g -factor would appear due to three dimensional confinement. The degree of deviation can be qualitatively discussed by comparing dot size with magnetic length [41].

Electron g -factor engineering in quantum wells

The g -factor engineering in semiconductors is an essential technique for application of spintronics and quantum computation because it directly determines the operability of carrier spins. As mentioned in the previous section, qualitative explanation for the g -factor modulation in a QW is given by considering the penetration of electron wavefunction into barrier layers. However, G. Lommer *et al.* [42] argued that the realistic probability of finding the subband electron on the AlGaAs layers is too small to reproduce the g -factor change observed in experiments. The authors proved that this discrepancy is compensated by taking into account the nonparabolicity of the bulk conduction band structure. The behavior of the g -factor in semiconductor systems expressed in equation (2.9) by L. M. Roth *et al.* is extended to a QW structure by E. L. Ivchenko and A. A. Kiselev [43]. Their work focused on the QW width dependence of the electron g -factor confined in a well structure using second-order $\mathbf{k} \cdot \mathbf{p}$ perturbation theory, and further predicted the anisotropy of the g -factor values originating from reduced symmetry of two-dimensional electron system.

Experimental demonstrations were later reported in various methods, such as electron spin resonance, Hanle effect, and spin quantum beats (QB). In particular P. Le Jeune *et al.* first experimentally showed the anisotropy of the electron g -factor in GaAs/AlGaAs QWs using QB method [44]. Figure 2.4 shows assembled data of the electron g -factor in GaAs/AlGaAs QWs as a function of QW width. They observed the crossing of the g -factor from negative through zero to positive values by reducing well width and hence increasing

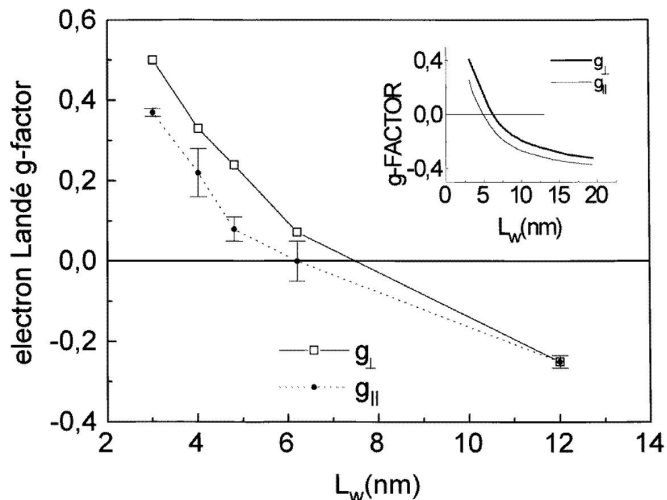


Figure 2.4: The longitudinal and transverse electron Landé g -factors in GaAs/Al_{0.35}Ga_{0.65}As QWs deduced from spin quantum beats [44]. The index \perp and \parallel indicate the perpendicular and parallel directions to the growth direction, respectively. The curves are guides for the eye (the error bars for the g -factor values are smaller than the symbol size). (Inset) Dependence of the calculated longitudinal and transverse g -factor components on the QW width according to Ref. [43].

the confinement energy. In GaAs/Al_{0.33}Ga_{0.67}As QW a g -factor near zero is realized at the well width of 6.2 nm for magnetic field parallel to the growth direction. They also depicted the larger anisotropy of the g -factor in narrower wells, while negligible anisotropy in wider wells up to 12 nm. The discrepancy between experiment and theory in the g -factor for magnetic field parallel to the growth direction (shown in the inset) is due to coupling with the HH band.

g -factor of holes

In contrast, theoretical study of the g -factor of the valence bands is much more complicated, since nonparabolicity and anisotropy of the Hamiltonian play crucial roles. The Zeeman interaction of a bulk hole is written by the following 4×4 matrix operator:

$$H_0 = -2\mu_B[\kappa(\mathbf{J} \cdot \mathbf{B}) + q(J_x^3 B_x + J_y^3 B_y + J_z^3 B_z)], \quad (2.10)$$

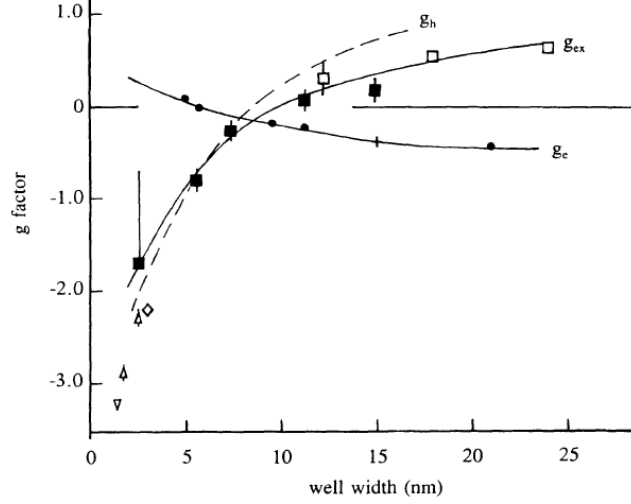


Figure 2.5: The electron (g_e), heavy-hole exciton (g_{ex}), and heavy-hole (g_h) g -factors in GaAs/AlGaAs QWs. The dashed curve is the difference of the two solid curves to guide the eye [45].

where \mathbf{J} is the total angular momentum vector, and κ and q are band structure parameters, named Luttinger parameters.

First, the HH g -factor in a QW for in-plane magnetic field shows the strong dependence on crystal growth direction. For high-symmetric growth direction such as [001] and [111], a dominant term of the HH g -factor is known to vanish. In contrast, low-symmetric growth direction leads to the finite HH g -factor. In a specific case of growth direction $[n\overline{n}(2m)]$ where n and m are integer, the HH g -factor anisotropy is given as follows:

$$\frac{g_{[n\overline{n}(2m)]}^{HH}}{g_{[110]}^{HH}} = -\frac{\sqrt{4 - 3\sin^2\theta}}{\sin\theta}, \quad (2.11)$$

where θ is the angle between [100] and $[mmn]$. Experimental reports for the in-plane HH g -factor in [001] QWs show values less than 0.05 [46–48].

Second, the HH g -factor for magnetic field parallel to the growth direction usually has a finite value given by $g_{hh} = 6\kappa + 13.5q$ using Luttinger parameters.

M. J. Snelling *et al.* reported a systematic investigation of the HH g -factor in GaAs/AlGaAs QWs with various well widths, using the Zeeman splitting of luminescence line at low temperature [45] (Fig. 2.5). Similar to the electron g -factor in QWs, the HH g -factor ranged from positive to negative with decreasing QW width. The authors mentioned that the origin of well-width dependence of the HH g -factor cannot be explained solely by the nonparabolicity of the bulk conduction band structure, indicating that the above Luttinger parameters are also well-width dependent.

On the other hand, systematic investigation of the g -factor of the LH subband in both theoretical and experimental works is not yet completed. One reason for this is the smaller effective mass compared to the HH subband, resulting in higher quantization energies. The LH g -factor for in-plane magnetic field is discussed by A. A. Kiselev *et al.* [49], in which the authors focus on unstrained and strained InGaAs/InP QWs. In contrast, the theoretical study of the LH g -factor for out of plane magnetic field is reported only recently [50]. In this study they took into account the proximity of the second HH subband and ground LH subband, and predicted the giant Zeeman splitting of the LH subband where the g -factor is enhanced by several orders of magnitude. Still there are only few experimental data for the out of plane LH g -factor [51, 52].

2.2.3 Towards coherent transfer between quantum bits

Up to these days, many physical forms of quantum information media have been investigated intensively. Each quantum system has its own advantages not to mention its drawbacks. For instance, a quantum bit (qubit) based on a photon can transmit information through long distances. There are several proposals for establishing all optical quantum networks [53–56], however they might be unsuitable for effective gate operations. Whereas a quantum bit based on a stationary electron spin in semiconductors has its strength on quantum information processing and storage. The significant synergy effect is expected by establishing a state-preserving quantum media conversion technology between

different quantum systems. From this perspective, demonstration of coherent transfer, the transfer of quantum mechanical superposition state, between different types of media will be a milestone for constructing a future quantum information network.

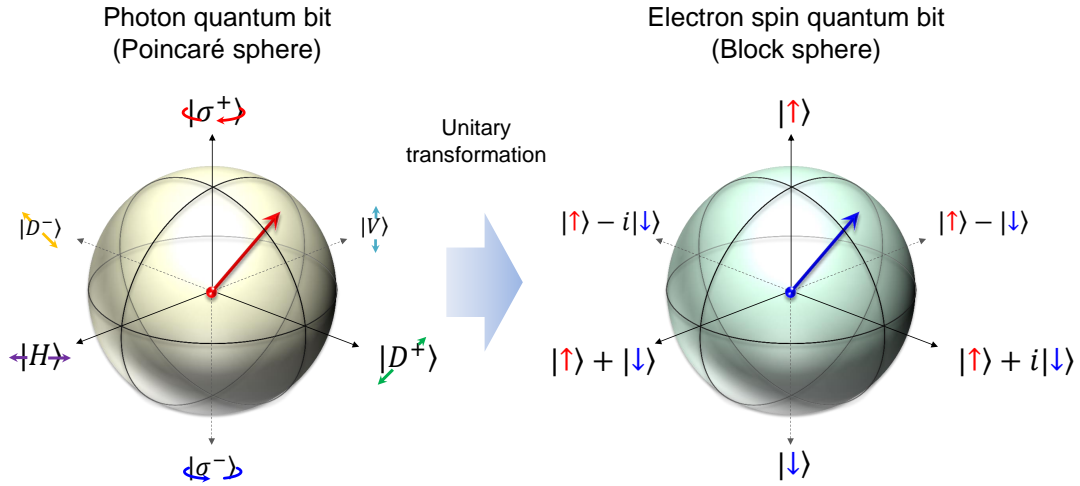


Figure 2.6: A schematic view of the coherent transfer from photon to electron spin with the unitary transform. The left figure is the Poincaré sphere for photon polarization states, and the right shows the Bloch sphere for electron spin states.

Let us focus on a photon polarization qubit and electron spin qubit as a representative of flying qubits and stationary qubits. Both qubits are basically described by a two-level system, i.e. $|\sigma^+\rangle$ and $|\sigma^-\rangle$ for photon polarization, and $|\uparrow\rangle$ and $|\downarrow\rangle$ for electron spin. Figure 2.6(left) exhibits the Poincaré sphere, where each point on the surface corresponds to a superposition of the above two states, whereas Figure 2.6(right) shows a Bloch sphere for electron spin superposition states. Significantly, both the Poincaré sphere and the Bloch sphere can be expressed by an identical Hilbert space $SU(2)$, allowing us to perform the unitary transfer between these two qubit systems as long as energy and angular momentum are conserved during the transformation process. In this section, the principle of the unitary transformation from photon polarization to electron spin in a g -factor engineered QW is introduced.

Scheme of coherent transfer

A coherent transfer scheme of quantum states from photon polarization qubit to electron spin qubit was proposed by R. Vrijen and E. Yablonovitch in 2001 [11]. In this proposal, they claimed that transfer of superposition states from photon polarization to electron spin can be performed in a QW system under magnetic field by utilizing selection rule. Figure 2.7 is the schematic view of the V-shaped

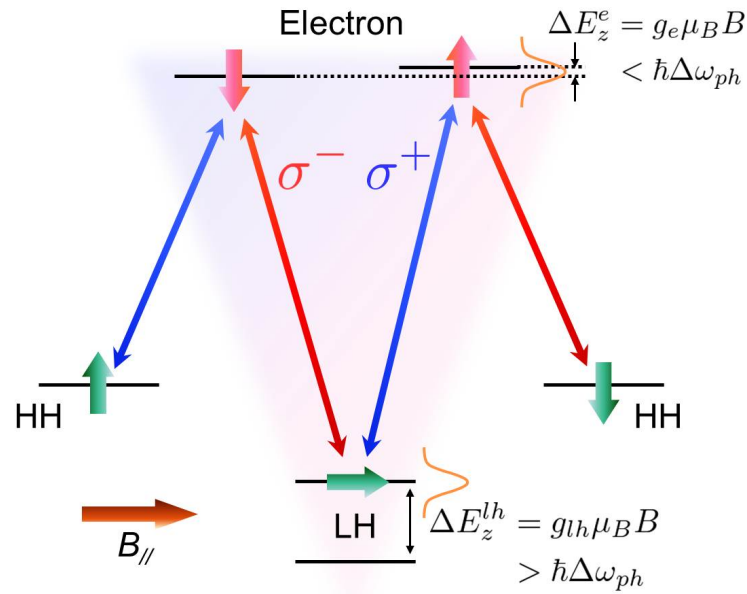


Figure 2.7: The schematic of V-shaped three level system for the coherent transfer from photon polarization to electron spin. The HH bands are assumed to be separated from the LH bands, and the in-plane magnetic field splits the two-fold degenerate LH energy levels, while the energy splitting of the conduction band remains within the range of incident laser bandwidth.

three-level system required in the above coherent transfer scheme. The authors assume a QW system based on III-V semiconductor, and the advantages of using QW structure are given as follows,

- (i) The LH bands and the HH bands are energetically separated

- (ii) The electron g -factor can be tuned considerably smaller than the LH g -factor,

however both are usually difficult to achieve in a single heterostructure.

When polarized photons are irradiated to bulk GaAs, electrons in both the LH and the HH bands are simultaneously excited, and the ratio of generated electron up- and down-spin is no better than 3:1 even with circularly polarized light. Thus, quantum state transfer is imperfect unless the light and HH bands are intentionally separated. The problem is solved by making use of a quantum confinement effect with which the degeneracy of the valence bands with different effective masses is lifted.

Still, excitation of either the light or HH bands does not preserve any phase information of polarized photons. For instance, when an electron is excited from the HH band by a polarized photon $|\phi\rangle_{ph} = \alpha|\sigma^+\rangle + \beta|\sigma^-\rangle$, the state of the electron-hole pair created is given by the following expression.

$$|\phi\rangle = \alpha| -3/2\rangle_h \otimes | -1/2\rangle_e + \beta|3/2\rangle_h \otimes |1/2\rangle_e. \quad (2.12)$$

Here, the photo-generated electron and hole are obviously entangled, and the lifetime of the electron-hole state is limited by the shorter of the two individual relaxation times. In GaAs the electron spin coherence time is known to be several μ s, whereas that of the hole spin is much shorter, of the order of 10 ps. The significant difference of spin coherence time arises from the fact that the conduction band consists of an s-type orbital with orbital angular momentum $L = 0$ leading to no entanglement between spin and orbital parts of the wavefunction, while the valence band consists of a p-type orbital with $L = 1$ which suffers considerably from the spin-orbit coupling effect.

The immediate spin decoherence due to electron-hole entanglement is avoided by applying a magnetic field to completely separate electron and hole states. The HH has an almost zero g -factor for the (001) GaAs QWs as explained in the previous section, therefore the HH excitation is unsuitable for the coherent transfer scheme that we are going to discuss. In the following discussion, the

HH band is assumed to be energetically separated from the LH and can be neglected. The two-fold degenerate LH states are written by:

$$|+\Psi\rangle_{lh} = \sqrt{\frac{2}{3}}|m_l = 0, m_s = 1/2\rangle + \sqrt{\frac{1}{3}}|m_l = 1, m_s = -1/2\rangle, \quad (2.13)$$

$$|-\Psi\rangle_{lh} = \sqrt{\frac{2}{3}}|m_l = 0, m_s = -1/2\rangle + \sqrt{\frac{1}{3}}|m_l = -1, m_s = 1/2\rangle. \quad (2.14)$$

With in-plane magnetic field applied, the degenerate LH states form bonding and anti-bonding states. The anti-bonding state is expressed as follows.

$$\begin{aligned} |-\rangle_{lh} &= \sqrt{\frac{1}{2}}[|+\Psi\rangle_{lh} - |-\Psi\rangle_{lh}] \\ &= \sqrt{\frac{1}{2}} \left[\sqrt{\frac{2}{3}}|0, 1/2\rangle + \sqrt{\frac{1}{3}}|1, -1/2\rangle - \sqrt{\frac{2}{3}}|0, -1/2\rangle - \sqrt{\frac{1}{3}}|-1, 1/2\rangle \right]. \end{aligned} \quad (2.15)$$

Assume that the laser wavelength is tuned to excite only the $|-\rangle_{lh}$ state. Since a polarized photon $|\sigma^+\rangle$ ($|\sigma^-\rangle$) excites an electron from the $m_l = -1$ ($m_l = +1$) state to the conduction band, a superposition state of the polarized photon $|\phi\rangle_{ph}$ creates the electron-hole superposition state:

$$|\phi\rangle_{eh} = |-\rangle_{lh} \otimes [\alpha|0, 1/2\rangle + \beta|0, -1/2\rangle], \quad (2.16)$$

where electron and hole states are separated from each other. In this condition, decoherence of a hole spin does not affect the electron spin state, and thus coherent transfer from photon polarization to electron spin with one-to-one correspondence is realized.

Experimental verification of the proposed coherent transfer scheme discussed above was reported by H. Kosaka *et al.* in 2008 [25]. In this work, the authors prepared a Ti:sapphire laser with bandwidth 0.38 nm as a photon-source, and GaAs/AlGaAs QW as a photo-detector. They evaluated the electron and the LH g -factors about -0.21 and -3.5 under in-plane magnetic field, which satisfy

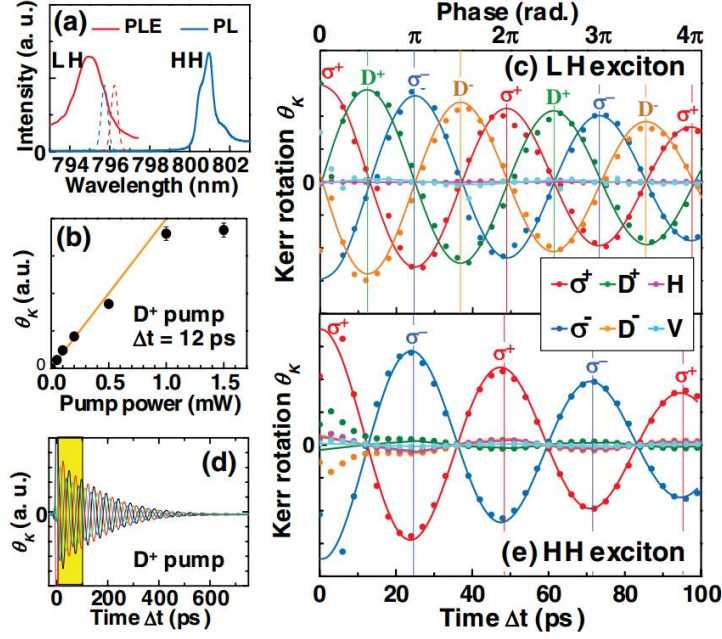


Figure 2.8: (a) (blue) PL and (red) PLE spectra of a g -factor engineered GaAs/AlGaAs QW detected at HH exciton emission under $B_x = 7$ T [25]. The broken lines show the spectra of the (red) pump and (blue) probe lights. (b) Pump power dependence of the Kerr rotation angle with D^+ under $B_x = 7$ T at $t = 12$ ps. (c) Temporal evolution of the Kerr rotation angle with six basis polarizations under $B_x = 7$ T. (d) Large-timescale view of (c). (e) HH-excitation case for comparison.

the requirement of the transfer scheme. As described in Fig. 2.8(a), excitation wavelengths of the HH and the LH are extracted from the photoluminescence (PL) and photoluminescence excitation (PLE) spectrum. Photo-generated electron spins are detected by Kerr rotation measurement, in which the polarization angle of the probe light is modified by electron spin polarization created by the pump light.

Figure 2.8(c) is the temporal evolution of Kerr rotation angle θ_K with six basis polarizations, where electrons are excited from the LH band under in-plane magnetic field $B = 7$ T. Noticeably, each of the consecutive phase shifts in the cyclic order of $|\sigma^+\rangle \rightarrow |D^+\rangle \rightarrow |\sigma^-\rangle \rightarrow |D^-\rangle \rightarrow |\sigma^+\rangle$ in $\pi/2$ steps, strongly indicating the superposition state transfer on a meridian of the Poincaré

sphere to that of the Bloch sphere. In contrast to the LH excitation, the HH excitation only demonstrates the considerable spin polarization with $|\sigma^+\rangle$ and $|\sigma^-\rangle$, showing that created spins are always projected along the z -axis. Note that in this experiment, spin readout is performed only in the y - z plane of the Poincaré and Bloch spheres. Further verification of state transfer in the x - z plane is later reported by the same group with tomographic Kerr rotation measurement [26].

Chapter 3

Basics of Quantum dots

Recent development of semiconductor fabrication techniques allows us to construct an artificial nanostructure which has gained much interest in the context of industrial application for nanoscale devices and fundamental study of quantum mechanics in solids. Especially quantum dots, often referred to as “artificial atoms”, are epoch-making technology to access charge and spin states of carriers confined in nano-scale region. Charge and spin states of carriers are readily detected with electrical transport measurement, as well as optical methods. To be concrete, quantized energy states and the behavior of individual carriers are resolved by only weakly coupling quantum dots to reservoirs via tunnel barriers. In such a device structure, but having stronger dot-reservoir couplings, carrier spin is often affected by other carrier spins in reservoirs, the example of which is the Kondo effect observed in single quantum dot. Furthermore, scalable systems are achieved by coupling more than one dots through tunnel barriers, which act as “artificial molecules”. In this section, fundamental properties of single and double quantum dots which are helpful in understanding the experiments in this work are outlined.

3.1 Single quantum dots

The quantum state of charge carriers trapped in a three-dimensional confinement potential can be investigated with various transport measurements. The constant interaction (CI) model is a well established model to describe experimental results of carrier transport through single and multiple quantum dots, such as Coulomb oscillation and Coulomb blockade. This model is based on the following two assumptions:

- (i) The Coulomb interactions of an electron on the dot with all other electrons, both inside and outside the dot, are parametrized by a constant capacitance C .
- (ii) The discrete, single-particle energy spectrum, calculated for non-interacting electrons, is unaffected by the interactions.

In the first assumption, the capacitance C is given by $C = C_S + C_D + C_G$, where C_S , C_D , and C_G are the capacitance between dot-source, dot-drain, and dot-gate respectively. The ground state energy of a quantum dot with N electrons is represented as follows:

$$U(N) = \frac{[-|e|(N - N_0) + C_S V_S + C_D V_D + C_G V_G]^2}{2C} + \sum_{n=1}^N E_n(B), \quad (3.1)$$

where $N_0|e|$ is a background charge of ionized donors in a semiconductor, V_S , V_D and V_G are the voltage applied to source, drain and gate, respectively. The chemical potential for the quantum dot can be defined by:

$$\begin{aligned} \mu(N) &= U(N) - U(N - 1) \\ &= (N - N_0 - \frac{1}{2})E_C - \frac{E_C}{|e|}(C_S V_S + C_D V_D + C_G V_G) + E_N, \end{aligned} \quad (3.2)$$

with $E_C = e^2/C$ being a charging energy. The corresponding addition energy, the difference of electrochemical potential between neighboring ground state

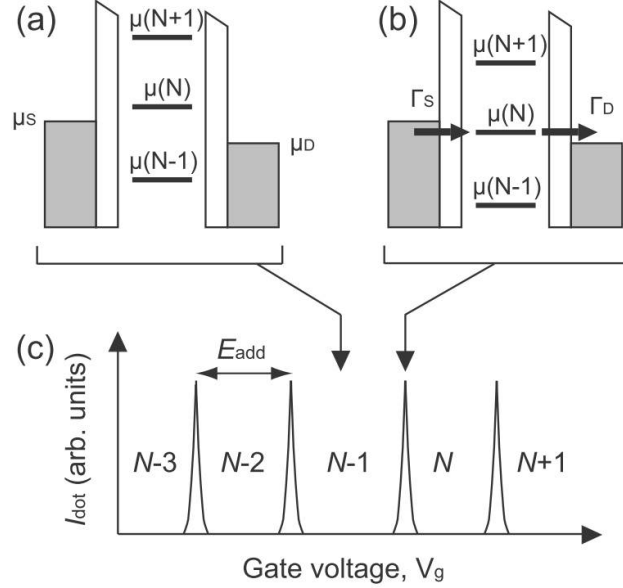


Figure 3.1: Quantum dot in the regime of low bias [23]. (a), (b) Schematic diagrams of the electrochemical potential levels of a quantum dot in the low-bias regime. (a) If no level in the dot falls within the bias window set by μ_S and μ_D , the electron number is fixed at $N - 1$ due to Coulomb blockade. (b) The $\mu(N)$ level is in the bias window, so the number of electrons can alternate between $N - 1$ and N , resulting in a single electron tunneling current. (c) Schematic plot of the current I_{DOT} through the dot as a function of gate voltage V_G . The gate voltages where the level alignments of (a) and (b) occur are indicated.

energy level, can then be written by:

$$E_{add}(N) = \mu(N + 1) - \mu(N) = E_C + \Delta E. \quad (3.3)$$

Note that addition energy is equivalent to charging energy when two spin degenerate electrons are added in the same orbital level.

The transport characteristics of electrons through a quantum dot are determined by the relative position of energy levels to source and drain electrochemical potentials. With a finite bias voltage, electrons can tunnel through the dot only when one or more discrete energy levels are present in the bias window. As energy levels are linearly modulated by gate voltage, the relative position of

levels are accessed by probing dot current from source to drain. In particular, in the low-bias regime ($|eV_{SD}| > E_C, \Delta E$) a finite dot current is expected only when one energy level is aligned in the bias window, and hence the Coulomb oscillation, the oscillation of dot current, should be observed by sweeping the gate voltage (see Figure 3.1).

3.2 Double quantum dots

Considering application of quantum dots in the context of a scalable electron spin-qubit system, double quantum dots are essential devices to achieve spin initialization, spin manipulation, high-fidelity spin readout, and quantum entanglement. We use double quantum dots as well in the photoelectron trapping experiments.

3.2.1 Charge transport in a double dot

Honeycomb structure in a stability diagram

First of all the charge state of double quantum dot is briefly discussed. Assume that two dots are connected in series with a center tunnel barrier and the energy levels of each dot are independently modified by gate voltages V_{G1} and V_{G2} . When two dots are not capacitively coupled, the charge states of a double quantum dot is expected to be a grid pattern as in Figure 3.2(a), where each separated rectangle region corresponds to a different charge state and each line to a charge state transition line. This diagram is called the charge stability diagram. If we take finite capacitive coupling between the two dots into consideration, the stability diagram deforms into a so-called honeycomb structure, which can be seen in Figure 3.2(b). In this condition each crossing point of charge transition lines splits into two “triple points” where three charge states are degenerate, since change of the electron number in one dot affects the energy levels of the other dot via capacitive coupling. The capacitive coupling between two dots is simply deduced by measuring the distance between neigh-

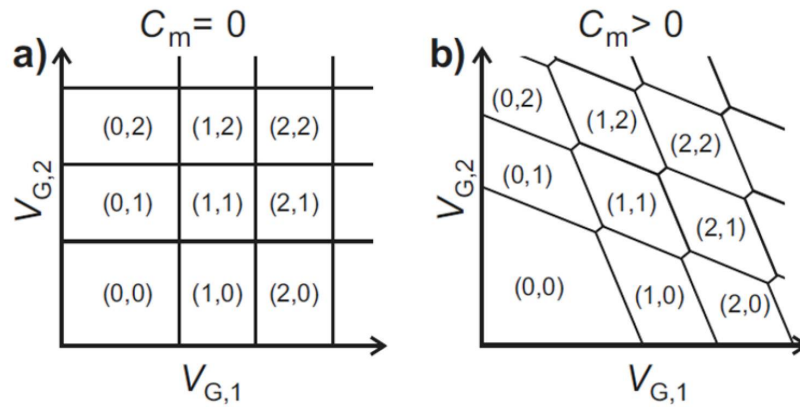


Figure 3.2: Charge stability diagrams for (a) uncoupled and (b) coupled double dots, depicting the equilibrium electron numbers (N_1 , N_2) in dots 1 and 2, respectively [23]. The lines indicate the gate voltage values at which the electron number changes. In (b), a finite cross capacitance between gate 1(2) and dot 2(1) is taken into account.

boring triple points. Note that in the low-bias condition, finite dot current is observed only near a triple point and any other condition is in blockade, while all the transition lines including inter-dot transitions are visible with the charge sensing technique.

In the few-electron double quantum dot, electron numbers trapped in two dots are counted from the $(0, 0)$ charge state where no more charge transition lines are found in negatively larger gate voltage condition. Figure 3.3 shows the stability diagram of a few-electron lateral double dot taken with the charge sensing method. In the left-bottom region, no charge transition lines are observed, which indicates that the double dot is emptied, with the $(0, 0)$ state. Charge state transition with total electron number constant, i.e. between $(n, m+1)$ and $(n+1, m)$ are distinguished in light color near the triple points.

Bias triangle on a triple point

As discussed previously for the single dot case, excited states as well as ground states of a double dot contribute to electron transport in the high-bias regime. With higher bias voltage, triple points develop into a triangle shape “bias tri-

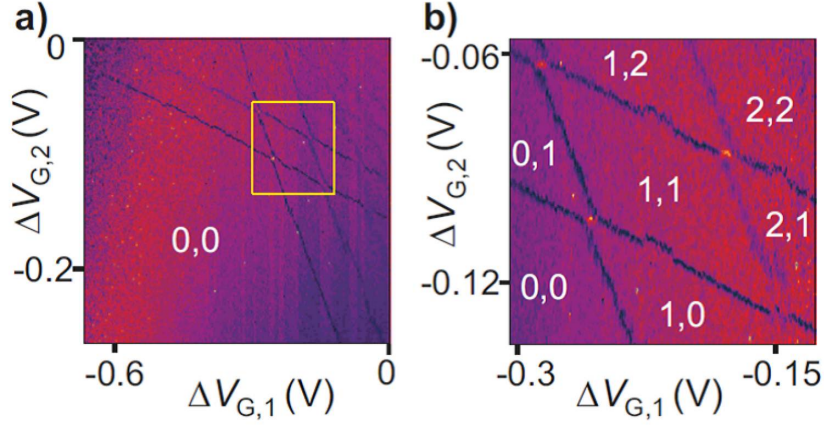


Figure 3.3: Charge sensing data on a double dot in the few-electron regime [57]. Dark lines signal the addition of a single electron to the double dot system. The absolute number of electrons in dots 1 and 2 is indicated in each region as N_1, N_2 .

angle”. The schematic diagram of a bias triangle is shown in Fig. 3.4. The bottom apex of the left triangle corresponds to a condition that the $(1, 0)$ and $(0, 1)$ ground states are energetically aligned to the Fermi level of the source, and the right apex of the left triangle to a condition that they are aligned to the Fermi level of the drain. These two points are linked with a resonance line, on which two energy states are aligned. In a dot current measurement, current can flow only within the triangle region, and conductance is often enhanced when any tunneling events through excited states are permitted. The effect of excited states is reflected on triangles in the form of additional lines parallel to the charge transition lines or resonance lines. It should be noted that the left triangle in a diagram is fully explained by single electron transport. In contrast, one needs to consider a state that two electrons exist in the double dot in the right triangle. However, the discussion is much simplified when regarding the situation as a single hole transport from the drain to the source, which is symmetrical with a single electron transport in the left triangle. In this sense, the left and the right triangles are often called “electron triangle” and “hole triangle”, respectively.

To obtain characteristic energy scales from experiment, gate voltages V_{G1}

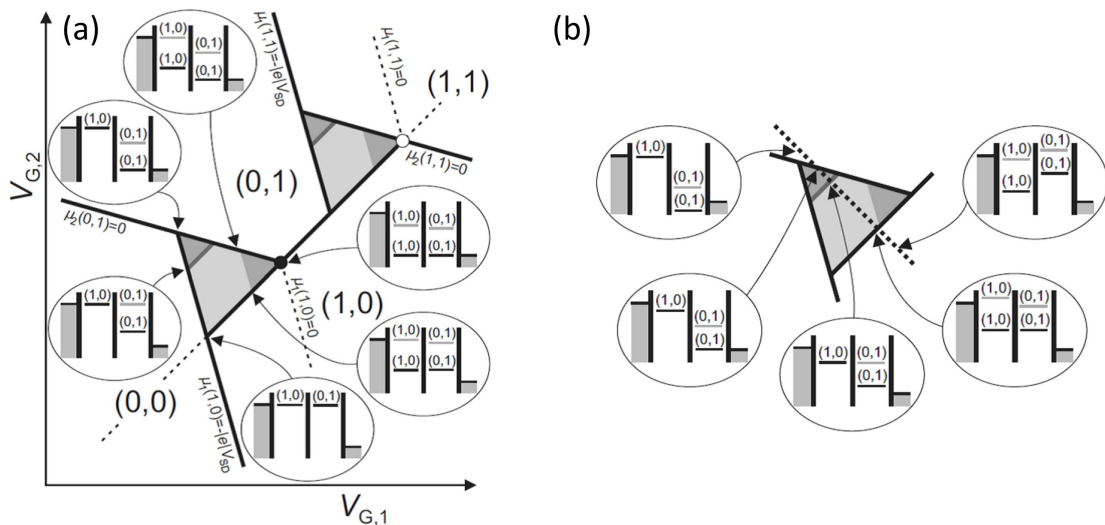


Figure 3.4: (a) A sketch of the triple points for an applied source-drain bias V_{SD} with the drain kept at ground. A triangle is formed from each triple point. Within this bias triangle charge transport through the dot is energetically allowed. Gray lines and regions in the triangles illustrate the gate voltages at which transitions involving excited-state levels play a role. (b) Level diagrams for different detunings ε between dot 1 and dot 2 (dotted line in the bias triangle).

and V_{G2} must be converted to the unit of energy. In double quantum dots the detuning energy ε , giving the energy difference between the two levels in each dot, is often used to discuss certain phenomena occurring through tunnel coupling between the dots. The detuning remains constant along lines parallel to the resonance line on the diagram, and especially on zero detuning, the energies of the focused electron states of the two dots are energetically aligned. In contrast, by sweeping two gate voltages along a dashed line in Figure 3.4(b), the energy difference between the two states can be tuned. Since the size of the bias triangle is set by the applied bias voltage on the dot, energy scales inside the triangle can be easily calculated. In this way certain excited state energies can be obtained from the resonance line separations.

Two electron spin states

Next the electron spin states of two electrons in a double quantum dot, often referred to as “artificial hydrogen molecule”, is introduced. When two electrons are both stored in one dot, i.e. (0, 2) state, four states can be formed. The spin part of the wavefunction for each state is written as:

$$\begin{aligned}
 S(0, 2) &= (|\uparrow_2\downarrow_2\rangle - |\downarrow_2\uparrow_2\rangle)/\sqrt{2}, \\
 T_+(0, 2) &= |\uparrow_2\uparrow_2\rangle, \\
 T_0(0, 2) &= (|\uparrow_2\downarrow_2\rangle + |\downarrow_2\uparrow_2\rangle)/\sqrt{2}, \\
 T_-(0, 2) &= |\downarrow_2\downarrow_2\rangle,
 \end{aligned} \tag{3.4}$$

where the spin index depicts the dot in which electrons are confined. Triplet states T_+ , T_0 , and T_- are degenerate without magnetic field, and the singlet state S is lower than the triplet states by E_{ST} . The energy difference E_Z between T_{\pm} and T_0 , which is equivalent to the Zeeman splitting energy, is modified by both perpendicular and in-plane magnetic field, whereas E_{ST} is changed only by the perpendicular magnetic field.

Similar to the (0, 2) state, the (1, 1) state consists of a singlet state and three-fold degenerate triplet states.

$$\begin{aligned}
 S(1, 1) &= (|\uparrow_1\downarrow_2\rangle - |\downarrow_1\uparrow_2\rangle)/\sqrt{2}, \\
 T_+(1, 1) &= |\uparrow_1\uparrow_2\rangle, \\
 T_0(1, 1) &= (|\uparrow_1\downarrow_2\rangle + |\downarrow_1\uparrow_2\rangle)/\sqrt{2}, \\
 T_-(1, 1) &= |\downarrow_1\downarrow_2\rangle.
 \end{aligned} \tag{3.5}$$

The energy difference J between singlet and triplet states is dependent on inter-dot tunnel coupling t_c and single dot charging energy E_C . The Hubbard approximation gives a relation of $J = 4t_c^2/E_C$ at the zero-detuning point. In Figure 3.5(a), two electron states in a double quantum dot with a weak tunnel coupling as a function of detuning ϵ is described. A finite tunnel coupling hy-

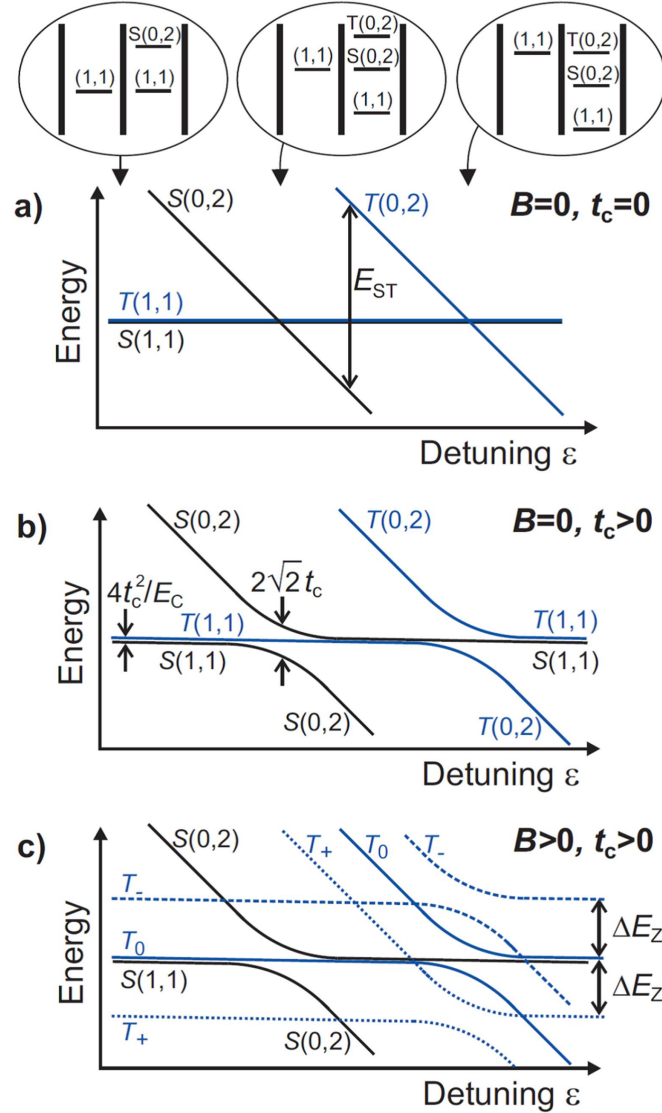


Figure 3.5: Energies of the two-electron spin singlet and triplet levels in a double dot as a function of detuning ε between the levels in the two dots for (a) $B = 0$ and negligible tunnel coupling t_c , (b) $B = 0$ but significantly high t_c , and (c) finite B and significantly high t_c .

bridizes the $(1, 1)$ and $(0, 2)$ states. Without taking the spin degree of freedom into account, avoided crossing between the $(1, 1)$ and $(0, 2)$ states characterized by a tunnel splitting $2\sqrt{2}t_c$ is expected. In reality, the $(1, 1)$ singlet and triplet

states only couple to the (0, 2) singlet and triplet states respectively, since spin should be conserved. Therefore the ground state singlets are only hybridized (Fig. 3.5(b)). At a zero magnetic field, E_{ST} , which is the order of 0.4-1 mV in GaAs lateral dots, pushes the avoided crossing of the triplets far away from that of the singlets. With a finite magnetic field the triplet states split by the Zeeman energy as mentioned above. The schematic diagram is shown in Fig. 3.5(c). A large magnetic field results in the separation of T_+ and T_- from T_0 state, and one can confine the relevant state space to S and T_0 .

3.2.2 Pauli spin blockade

In a series coupled quantum dot, transport current is rectified under a specific condition of Pauli exclusion. This is called Pauli spin blockade (PSB), and is applicable to a high-fidelity electron spin readout in multi-quantum dots. First observation of spin blockade is reported in a vertical double quantum dot [58], and further investigated in lateral quantum dots in terms of both transport and charge sensing measurement [59, 60]. Figure 3.6 shows the dot current through a double quantum dot as a function of bias voltage. The double dot is adjusted to achieve transition from the (1, 1) to (0, 2) states via inter-dot tunneling. In the main I-V curve, electron transport through the singlet states in the linear transport regime is observed at $|V| < 1$ mV. For nonlinear transport in larger bias, the spin blockade suppresses the dot current at $1 < V < 7$ mV, while finite current flows for negative side. In the spin blockade regime, both up- and down-spin electrons can come into the left dot, and down-spin electron tunnels to the right dot within a time scale determined by inter-dot coupling. In contrast, current is blocked as soon as an up-spin electron comes into the left dot and forms a triplet state. The blockade condition lasts for a spin relaxation time T_1 which is typically much longer than the inter-dot tunneling time of a singlet state, and thus the averaged current is greatly suppressed.

At $B = 0$ T, the spin blockade in a double quantum dot is found to be lifted by random nuclear field fluctuation [59]. Figure 3.7(1A) and (1B) are

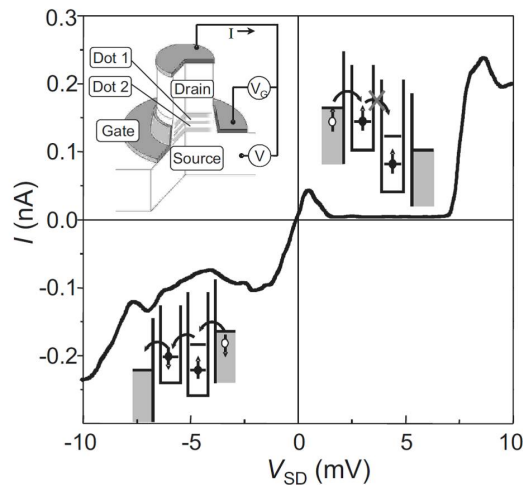


Figure 3.6: I - V curve showing electron transport through the singlet states in the linear response region for $V < 1$ mV [58]. For nonlinear transport in forward bias, the spin blockade region associated with the formation of the $(1, 1)$ triplet is for V from 1 to 7 mV. The two potential diagrams illustrate the situations for spin blockade in forward bias and continuous electron transport via the singlet states in reverse bias. The upper left figure is the device structure of the vertical double quantum dot.

color-scale plots of dot current showing bias triangles where tunnel coupling is small and spin blockade is expected to occur. The dotted region indicates spin blockade. In the absence of an external magnetic field, leakage current is seen along resonance line (Fig. 3.7(1A)). Furthermore, the leakage current is strongly reduced under a finite magnetic field. The existence and suppression of leakage current is a direct consequence of the hyperfine interaction between electron spins and nuclear spins, which hybridizes the singlet and the triplet states and hence lifts the spin blockade. Figure 3.7(2A) and (2B) show the magnetic field and detuning dependence for leakage current at weak and strong inter-dot couplings. Since the external magnetic field separates two triplet states T_+ and T_- out of the energy scale of hyperfine mixing, spin blockade occurs when the above two triplet states are formed, and suppression of leakage current results. The authors further deduced the magnitude of the inhomogeneous field $\sqrt{\langle B_N^2 \rangle} = 1.73 \pm 0.02$ mT. The inhomogeneous field is interpreted as the fluctuation of

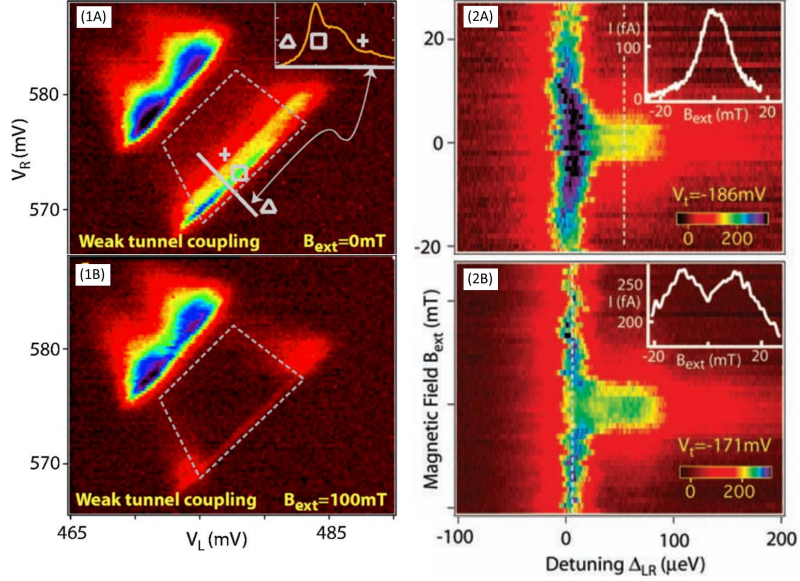


Figure 3.7: (1A) Bias triangle measured in a lateral double quantum dot for smaller inter-dot tunnel coupling, where spin blockade is expected to occur [59]. A marked increase of leakage current is seen in the lower part of the Pauli blocked area (the green and yellow band). (Inset) One-dimensional trace along the solid gray line, with Coulomb blocked, resonant, and inelastic transport regimes. (1B) Analogous data for the same tunnel coupling as in (1A), but for $B_{ext} = 100$ mT. The leakage current from (1A) is strongly suppressed. (2A) Leakage current as a function of detuning and magnetic field for small tunnel coupling ($< E_N$). Both the resonant and inelastic leakage currents drop monotonically with B_{ext} . Inset: Magnetic field dependence of the inelastic current along the dotted line ($\Delta_{LR} = 40$ meV). (2B) For larger t ($> E_N$).

the nuclear spin field difference between the two dots.

It is clearly proved in charge sensing measurements that the current rectification originates from a blocked inter-dot charge transition. Figure 3.8 shows the charge sensor conductance measured as a function of two gate voltages V_L and V_R in the one- and two-electron regimes. Plotted gray-scale color directly reflects the time-averaged occupation probability of electrons in two dots. In contrast to the transition between (1, 0) and (0, 1), the transition between (1, 1) and (0, 2) is not symmetric for the opposite bias case. With positive bias in the latter case, charge states evolve in the order (0, 1) \rightarrow (0, 2) \rightarrow (1, 1) \rightarrow (0, 1),

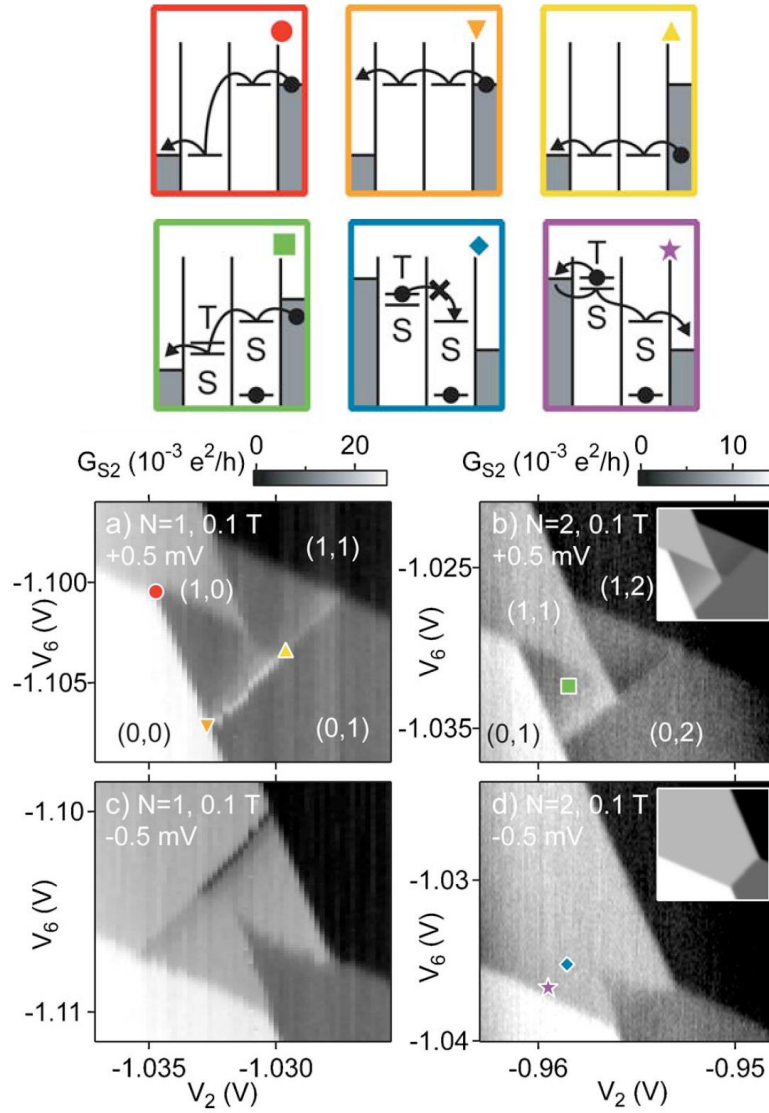


Figure 3.8: Charge sensor signal measured in a lateral double quantum dot [60]. A plane is subtracted from each panel to remove direct gate-QPC coupling. Inset shows the corresponding simulation result using a rate equation model. The charge transitions for several gate voltage conditions are illustrated at the top of the figure.

where the electron spin from the source is filtered so as to form a singlet state and always enables tunneling to the left dot. On the other hand, both up- and down-spin can enter the right dot at negative bias, and once the triplet state is formed, a trapped electron can neither tunnel to the right dot nor return to the lead. As a result, the charge sensing signal in the spin blockade region coincides with that of the $(1, 1)$ state, strongly suggesting that current rectification is mostly attributed to a transition process of $(1, 1) \rightarrow (0, 2)$.

3.3 Charge sensing and spin detection techniques

Fast and sensitive single electron charge sensing allows deep investigation to detect dynamical response of charge and spin states of quantum dots. The technology of charge sensing was earlier developed using SETs in superconductors [61]. They applied the concept of driving a small current beside the measured structure to create electrometers that could sense down to a single electron. The technique is then applied to gate defined GaAs nano-structures such as QDs with tunable electron charge states. The tunneling of single electrons and the related spin dependent tunneling in QDs are observable with the charge sensor. The physical properties such as spin relaxation mechanisms are identified through measurement of the spin dynamics with combined techniques of charge sensing and spin to charge information conversion. Additionally, fast spin measurement can offer an ingredient to realize error correction or teleportation in quantum information processing. Here, the basics of charge sensors and techniques to measure single spin information are introduced.

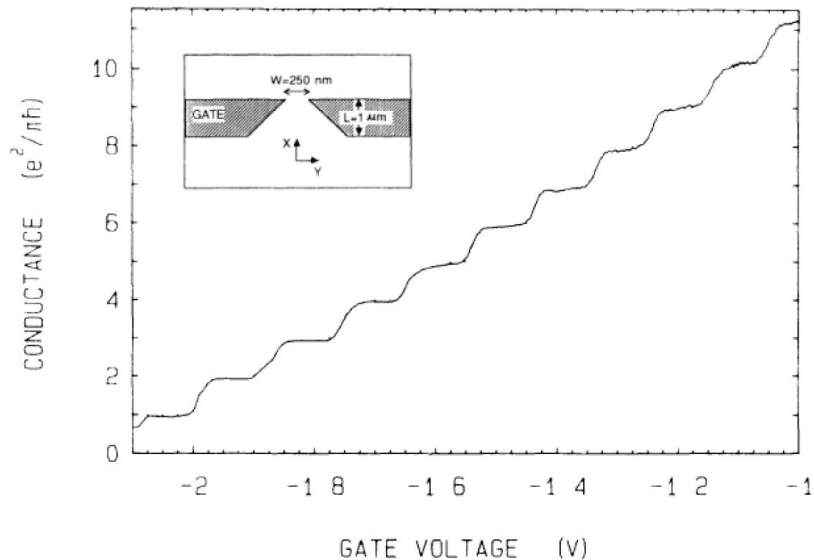


Figure 3.9: Conductance through a gate-defined point contact as a function of gate voltage after subtraction of the lead resistance [62]. The conductance shows plateaus at multiples of $2e^2/h$.

3.3.1 Charge sensing

Quantum point contact charge sensor

The conductance in a ballistic one-dimensional quantum wire is given by:

$$G = N_C \frac{2e^2}{h}, \quad (3.6)$$

with N_C the number of subbands below the Fermi energy. One can interpret this relation as a quantization of one-dimensional conductance since N_C is an integer, and the one-dimensional system showing the quantized conductance is called a quantum point contact (QPC). Figure 3.9 is the first experimental observation of conductance quantization through a QPC in a two-dimensional electron gas [62]. As shown in the inset, two gates are fabricated on a high electron mobility transistor (HEMT) to deplete the two-dimensional electron gas, and with further applying negative gate voltage, a series of conductance

steps with a unit of $2e^2/h$ is observed. This result indicates that as the gate voltage is made more negative, N_C decreases one by one.

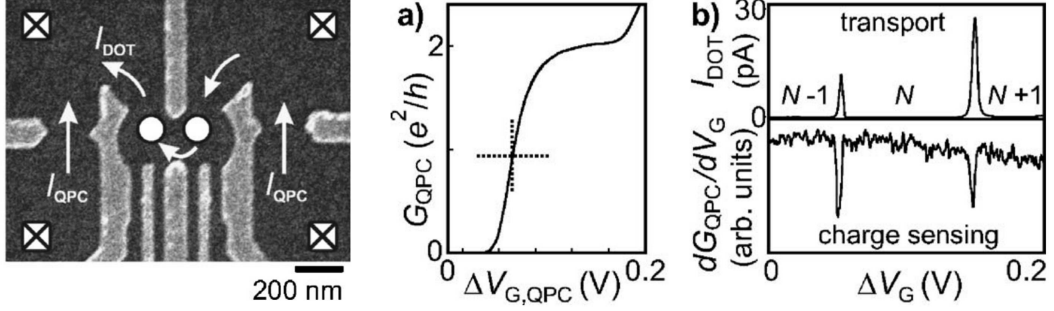


Figure 3.10: (left) SEM image of a double quantum dot with QPC charge sensors on left and right sides [57]. (a) Conductance through QPC sensor with sweeping gate voltage. (b) (top) Coulomb oscillation in dot current and (bottom) the corresponding QPC signal. Sharp peaks in numerical derivative of QPC conductance indicate charge state transitions in the quantum dot.

The current through the QPC is insensitive to change of background electrostatic potential if the voltage is set at a conductance plateau, while it is highly sensitive to the outside environment at a gate voltage between the plateaus. Therefore, with this gate voltage setting the QPC is a high-sensitivity mesoscopic electrometer. The left picture in Fig. 3.10 is a scanning electron microscope (SEM) image of a gate-defined double quantum dot [57]. Two QPC charge sensors are fabricated at the right and left side of the dot. The center figure is the first conductance step, and the gate voltage $V_{G,QPC}$ is set at a point halfway to the plateau. The right figure depicts the Coulomb peaks in the dot current in the upper panel, and the corresponding QPC signal or a numerical derivative dI_{QPC}/dV_G in the lower panel. Because charge state transition in the quantum dot changes the electrostatic potential at the QPC, the QPC signal shows peaks when the electron number in the dot changes, as identified by the Coulomb peak.

Quantum dot charge sensor

By constraining the charge sensor current in a lower dimension, a more sophisticated type of charge sensor is realized with higher sensitivity and better signal to noise ratio. Here, a charge sensor consisted of a three-dimensionally confined QD is introduced. An additional sensor QD can be placed near the target QD (Fig. 3.11) [63]. Conductance of the QD sensor shows peaks as a function of gate voltages. The greater slope of the peak, compared to the slope of the QPC sensor, indicates the higher sensitivity as a charge sensor. Reduced screening and small characteristic energy needed to change transmission in the quantum dot are responsible for the improved performance.

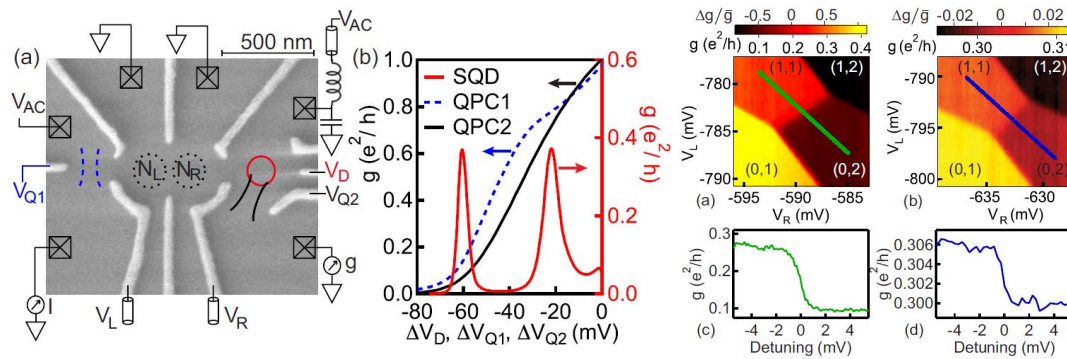


Figure 3.11: (a) Micrograph of a double quantum dot sample with an additional sensor dot on the right. Gate voltages V_L and V_R control the double-dot charge. Plunger gate V_D can also be operated as a point contact. (b) Single QD measured by rf reflectometry.

Real-time charge sensing

In addition, charge sensing is useful for a real-time measurement of the change of electron number in quantum dots. The first demonstration of the real-time detection was reported by W. Lu *et al.* using an integrated radio-frequency single-electron transistor charge sensor [64]. Later, a similar experiment was performed using a QPC charge sensor [65]. Figure 3.12(a) shows an atomic

force microscope (AFM) image of a quantum dot fabricated with surface probe lithography. In Fig. 3.12(b), top left shows the time-dependent trace of a typical charge sensing signal near the charge transition point, and the histogram is seen in the top right figure. The QPC conductance fluctuates between two values corresponding to N_0 and $N_0 + 1$ electron states, indicating the real-time observation of electron tunneling. The authors further showed the change of averaged electron number occupied in a quantum dot by sweeping gate voltage across the charge transition point (Fig. 3.12(b) bottom).

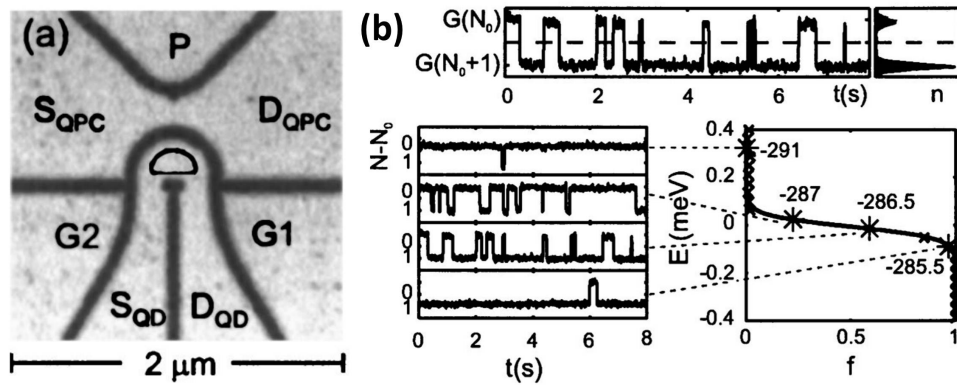


Figure 3.12: (a) Atomic force micrograph of the structure with designations of gates created by surface probe lithography [65]. (b) Single oscilloscope trace of the QPC conductance vs time (top left). The dot was tuned to a point near a step in the QPC conductance. Histogram of the data and 19 similar sweeps is shown at top right. Changing the voltage V_{G1} modifies the electrochemical potential of the dot and allows a transition from the N electron state to the $N + 1$ electron state (bottom).

3.3.2 Single-shot readout of electron spins

A difficult task in quantum information processing and spintronics is the direct measurement of a single electron spin. Single-shot readout implies that the measurement must have high fidelity (ideally 100%) since only one copy of the state is available and no averaging is possible. Readout of single spin states has been achieved using optical techniques in 1988 [66]. Several ideas for electrical single electron spin measurement was proposed using various spin-dependent energy

terms [67–70]. The first demonstration of electrical single-shot measurement of the state of an individual electron spin in a semiconductor quantum dot was reported in Reference [71]. Each electron spin is first influenced directly by an external magnetic field via the Zeeman energy $E_Z = S_z g \mu_B B$, where S_z is the spin z component. This generally leads to a spin state with a different energy. By correlating the spin states to different charge states and subsequently measuring the charge on the dot, the spin state can be determined. This way, the measurement of a single spin is replaced by the measurement of a single charge, which is a much easier task. Until now, various kinds of spin readout have been demonstrated using single and double QDs. Some of the general techniques are introduced in this section.

First demonstration of spin readout

The first demonstration of spin detection in Reference [71] uses a difference in energy between the spin states for spin-to-charge conversion. In this energy-selective readout, the electrochemical potential of the reservoir is positioned between the Zeeman substates in the dot (Fig. 3.13(a)). The Zeeman splitting is larger than the thermal broadening in the reservoir. One electron can tunnel off the dot from the spin excited state (ES) and then tunnel in the ground state (GS), whereas in the GS it cannot tunnel off the dot. This difference of temporal charge movement can be detected by the charge sensing to determine the initial electron state, either ES or GS.

A gate voltage pulse procedure was used here to, (i) empty the dot, (ii) inject one electron spin, and then (iii) measure its spin state. Experimental traces of the pulse response show spin detection at an in-plane field of 10 T (Fig. 3.13(b)). When the electron is in GS (spin-up), its energy level is below μ_{res} , so the electron remains on the dot (red line region in Fig. 3.13(b)(top)). When the electron is in ES (spin-down), its energy level is above μ_{res} , so the electron tunnels to the reservoir after a typical time $\approx \tau$. Then an extra electron can tunnel onto the dot leaving a step signal (red line region in Fig. 3.13(b)(bottom)).

This scheme is simple but it has some drawbacks.

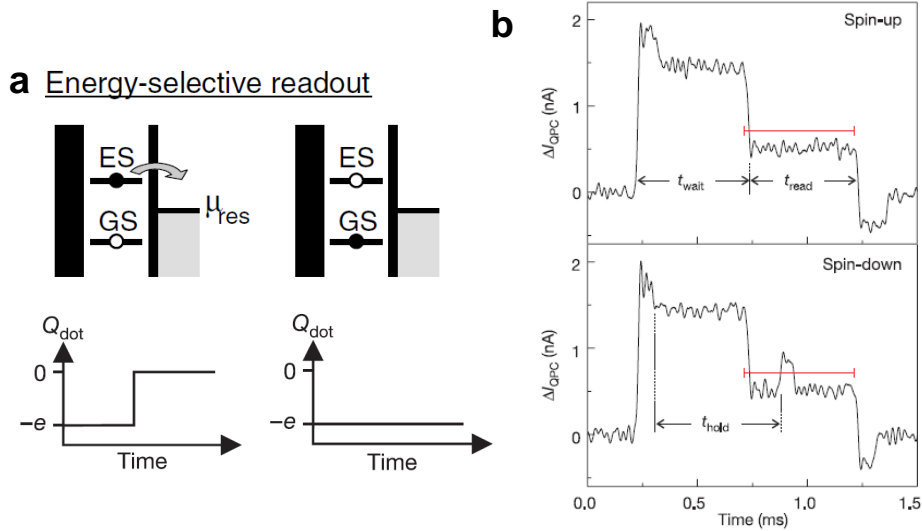


Figure 3.13: (a) Energy diagrams explaining the scheme for spin-to-charge conversion. Tunneling is energetically allowed from ES, but not from GS. (b) Single-shot read-out of one electron spin. Typical time-resolved measurements of the QPC current in response to a two-level pulse. In the top panel, an electron is injected during t_{wait} and is declared ‘GS’ during t_{read} . In the lower panel, the injected electron is declared ‘ES’ by the characteristic step which crosses the threshold (red line) during t_{read} .

- (i) The Zeeman splitting must be larger than the thermal energy of electrons in the reservoir. Thus single spin readout is only effective at very low electron temperature and high magnetic fields ($k_{BT} \ll \Delta E_Z$).
- (ii) The positioning of the spin levels with respect to the reservoir is very sensitive to fluctuations in the electrostatic potential. Background charge fluctuations induced electrically or optically can easily degrade the readout configuration.
- (iii) High-frequency noise can spoil the measurement, because photon-assisted tunneling can induce transition from the spin ground state to the reservoir [72]. In addition, since the QPC is a source of shot noise, this limits the current through the QPC and thereby the bandwidth of the charge detection.

These constraints have motivated the search for a different method for spin-to-charge conversion, and have led to the demonstration of the tunnel rate selective readout.

Tunneling rate selective spin readout

Spin-to-charge conversion can be achieved by exploiting the difference in the tunneling rate of the different spin states to the reservoir. Similarly, the different tunneling rates can be achieved for inter-dot tunneling to the discrete levels of a second dot. The concept of the tunnel rate selective spin readout is outlined in this section. The first demonstration of this technique uses the tunneling rate difference between ES and GS to the reservoir (Fig. 3.14(a)).

Here, spin dependent tunneling was demonstrated for a two-electron dot, where GS is the spin-singlet (S), and ES is the spin-triplet state (T). Since the wave function in this excited orbital has more weight near the edge of the dot, the coupling to the reservoir is stronger than for the lowest orbital. Therefore the tunneling rate from the triplet state to the reservoir Γ_T is much larger than the rate from the singlet state Γ_S , i.e., $\Gamma_T \gg \Gamma_S$. The spin readout was tested experimentally by applying gate voltage pulses as depicted in Fig. 3.14(b). Figure 3.14(c) shows the expected response of I_{QPC} to the pulse. During the readout process either of the electron spin can leave the dot giving an additional step in I_{QPC} as indicated by an arrow in Fig. 3.14(c). Tunneling rates were tuned such that the tunneling event of S is clearly visible but most of the tunneling events of T are not resolved. In order to discriminate between S and T , the number of electrons on the dot is determined at the readout time (vertical dashed line in Fig. 3.14(d)). If I_{QPC} is below the threshold, it means $N=2$ and the state is declared ‘S’. If it is above the threshold, it follows that $N=1$ and the state is declared ‘T’.

A major advantage of the tunneling rate selective readout scheme is that it does not rely on a large energy splitting between spin states. Furthermore, it is robust against background charge fluctuations, since these cause only a small variation in the tunneling rates. Finally, photon-assisted tunneling is not

harmful since tunneling is energetically allowed regardless of the initial spin state. Thus, the tunneling rate selective readout overcomes several constraints of energy selective readout. In general, the best choice of readout method will depend on the specific demands of the experiment.

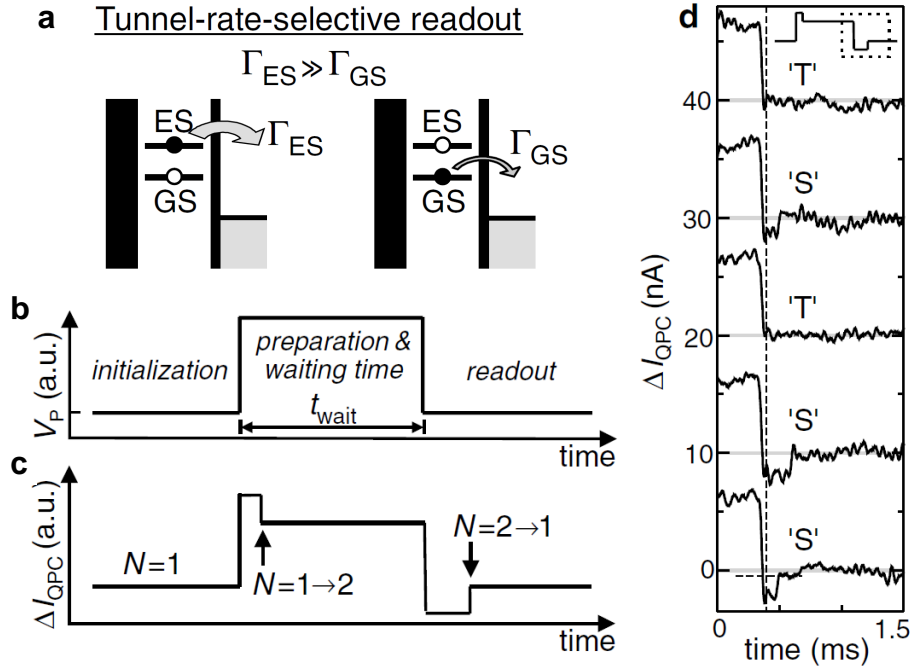


Figure 3.14: (a) Tunnel rate selective readout. One electron is allowed to tunnel off the dot, regardless of the spin state, but the tunnel rate depends strongly on the spin state: $\Gamma_{ES} \gg \Gamma_{GS}$. If a charge measurement after a time τ , where $\Gamma_{GS}^{-1} \gg \tau \gg \Gamma_{ES}^{-1}$, indicates that one electron has (not) tunneled, the state is declared ‘ES’ (‘GS’). (b) Pulse waveform applied in Reference [73]. (c) Response of the QPC current to the waveform of (b). In the readout stage, spin is converted to charge information due to the difference in tunneling rates for states GS and ES. (d) Real-time traces of ΔI_{QPC} during the last part of the waveform (dashed box in the inset). At the vertical dashed line, N is determined by comparison with a threshold (horizontal dashed line in bottom trace) and the spin state is declared ‘ES’ (‘T’) or ‘GS’ (‘S’) accordingly.

Degree of spin measurement accuracy

For application in quantum information processing it is important to know the accuracy, or fidelity of the single-shot spin readout. The measurement fidelity is characterized by two parameters, α and β (inset of Fig. 3.15), where α (β) corresponds to the probability of measuring ‘ES’ (‘GS’) though the initial state is GS (ES). This kind of readout error is caused by for instance, thermally acti-

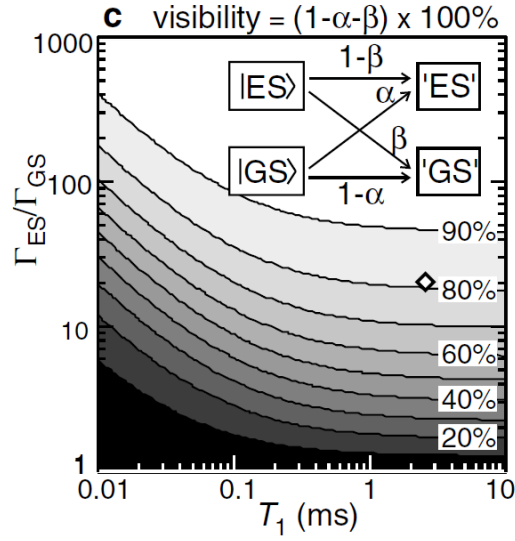


Figure 3.15: Visibility of the tunneling rate selective readout as a function of the spin relaxation time T_1 and the ratio Γ_{ES}/Γ_{GS} , for $\Gamma_{GS}=2.5$ kHz. The diamond corresponds to the readout parameters of Reference [73]. Inset: definition of the error rates α and β . If the initial state is GS, there is a probability α that the measurement gives the wrong outcome, i.e., ‘ES’ (β is defined similarly).

vated tunneling or electrical noise, similar to dark counts in photon detectors. An ES electron can relax to GS before the spin measurement which is modeled by a rate $1/T_1$. Analytically this gives,

$$\alpha = 1 - e^{-\Gamma_{GS}\tau} \quad (3.7)$$

$$\beta = \frac{(1/T_1)e^{-\Gamma_{GS}\tau} + (\Gamma_{ES} - \Gamma_{GS})e^{-(\Gamma_{ES}1/T_1)\tau}}{\Gamma_{ES} + 1/T_1 - \Gamma_{GS}} \quad (3.8)$$

where τ is the threshold time. The optimal value of the threshold is obtained for which the ‘visibility’ $1 - \alpha - \beta$ is maximal. Figure 3.15 plots the visibility as a function of T_1 and the ratio of the tunneling rates Γ_{ES}/Γ_{GS} .

3.3.3 Non-destructive spin state measurement

It is interesting to think about a measurement protocol that would leave the spin state unaffected, a so-called quantum non demolition (QND) measurement. QND measurement is known for a possibility to realize a partial Bell-state measurement that can consist in a measurement-based quantum computation. With this, two-qubit gates could be replaced with the measurement, so it simplifies the realization of a scalable quantum computer [74]. In terms of single spin measurement, QND measurement can give repeated spin state signals with the same output, offering a higher accuracy of the spin measurement [68].

The usage of the term ‘demolition’ has different interpretations depending on the measurement one is focusing on, for example losing the spin quantum state or losing the particle. Charge measurements that may not have an effect on the spin state can be non-demolishing for spin states. On the other hand, spin measurements inevitably demolishes the spin state by its projection measurement but can still conserve the electron number or the spin state projected onto some eigenstate. The measurement we focus in this study is the spin measurements in double dots that preserves the total electron number in the dot. If the measurement is faster than T_1 , spin readout is possible after spin manipulation. To emphasize this fact, we would like to use the term ‘non-destructive’ for indicating the conservation of the measured electron within the dot structure, and not the spin state.

With the readout schemes that make use of tunneling to a reservoir, non-destructive measurements are not possible because the electron is lost after tunneling. In single dots, though non-demolishing measurement of spins by re-initializing the dot spin state is possible [75], further manipulation such as partial Bell-state measurement is not possible. By making the electron tun-

nel not to a reservoir but to a second dot, the electron can be preserved and non-destructive measurements are in principle possible. Additionally, the non-destructiveness is crucial in the photon to spin conversion. The converted electron spin in the dot must be measured or manipulated after electron detection thus requires the non-destructiveness subsequent to photoelectron trapping. Non-destructive detection is realized in optical measurements [76, 77] but subsequent manipulation is yet to be realized.

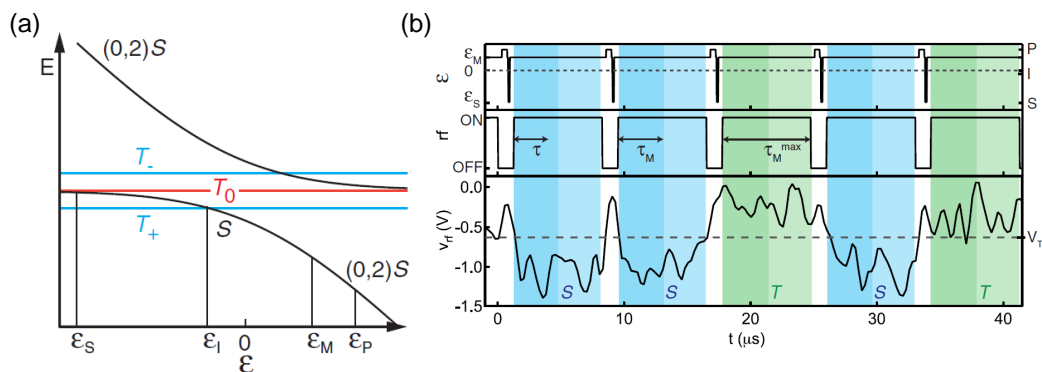


Figure 3.16: (a) Two-electron energy levels as a function of detuning ε from (0,2)-(1,1) degeneracy. Markers indicate gate voltages used in single-shot mode. Preparation of (0,2) singlet (P); separation for $S - T_0$ mixing (S) and $S - T_+$ mixing (I); measurement (M); operating point with 0 V pulse amplitude (D). (b) Pulse sequence of ε , controlled by V_R and V_L , cycling through the points P, S, M . Sensor signal v_{rf} indicates triplet (green, marked T) or singlet (blue, marked S) outcome.

An important example of a non-destructive spin detection scheme is the readout of singlet and triplet states in a DQD using Pauli spin blockade. Measurements of the two electron spin state is utilized to measure spin qubits operating in a singlet-triplet basis [78]. The singlet and triplet spin states are mapped to (1,1) and (0,2) charge states which are measured by a QPC. Recent reports demonstrate rapid single-shot measurements that can also give access to the dynamics of the environment, for instance the nuclear spin field environment [79].

Figure 3.16 shows an example of such single-shot measurement. Energy

levels of the system as a function of detuning, ε , from the (1,1)-(0,2) charge degeneracy are shown in Fig. 3.16(a). A pulse cycle (Fig. 3.16(b)(top)) first at P where a spin singlet in (0,2) is prepared and then to S changes the detuning point, where S and T_0 (S and T_+) are nearly degenerate. Finally the system is brought to the measurement point M for a time τ_M^{\max} . If the separated electrons are in the singlet configuration of (1,1) at M, the system will return to (0,2), which will be detected by the QPC. If the two electrons are in the triplet state, they will remain in (1,1) at M, and detected accordingly (Fig. 3.16(b)(bottom)).

Replacing the single-shot measurement with a continuous real-time measurement of S and T can give similar information. Utilizing the spin blockade in a resonance condition has a possibility of continuous real-time spin measurements. This could serve as a reliable readout mechanism, currently implemented in optical spin measurements, for the purpose of quantum computing [80].

Chapter 4

Preceding studies on single photon detection

The experiment explained in §2.2.3 is undoubtedly an innovative achievement demonstrating the applicability of the coherent transfer scheme based on V-shaped three level systems. Still, in the context of practical use of quantum media conversion and construction of a quantum information network there remains another critical issue to be solved, that is, the information transfer between a single photon and a single electron spin. The preceding works by Kosaka *et al.* employed a two-dimensional system where incident light creates a large amount of electron-hole pairs. As a consequence, one can only observe the ensemble spin state instead of individual electron spin states. For direct measurement of single electron spin states in semiconductors, a QD with three-dimensional confining of electrons is a promising system.

Natural extension of the method on the above two-dimensional system is a lateral QD fabricated on a QW, in which individual electron spin states can be detected. There are several advantages of utilizing a lateral QD. First, implementation of a QPC charge sensor enables the real-time non-destructive readout of charge and spin states of photo-excited electrons. Next, established electrically driven spin manipulation methods can be directly applied to the photo-electron spins. In addition, separation of optically created holes is expected to

be relatively easy since in a plane perpendicular to the growth direction, the electrostatic potential for the holes gives a local-maximum at the dot region, resulting in the escape of holes from simultaneously generated electrons.

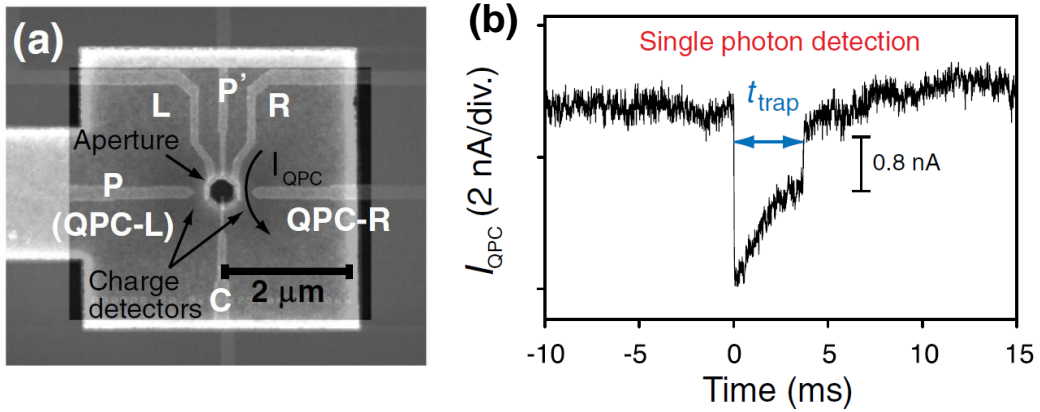


Figure 4.1: (a) Graphical superposition of two scanning electron microscopy images of a lateral QD device taken before and after the deposition of the metal mask [30]. (b) Measured I_{QPC} traces when a photo-generated electron is trapped.

For the first step toward the verification of coherent transfer from single photons to single electron spins, A. Pioda *et al.* realized the real-time detection of a single photo-generated electron using a QPC charge sensing technique [30]. In this work, they fabricated a single QD on a GaAs HEMT wafer, with the important part of the dot covered by an insulator and a metal mask with an aperture just above the dot. The SEM image of the device is seen in Fig. 4.1(a). The change of electron number is monitored by a nearby QPC, and the tunnel rate is modulated by gate voltage, and a laser pulse is irradiated from the top side of the sample to selectively excite electrons in a QD region. Note that in this scheme electrons generated in the buffer layer of GaAs are attracted to the GaAs/AlGaAs interface due to the internal built-in electric field, while created holes move to the back of the wafer. Figure 4.1(b) depicts the photo-response of the QPC current with gate voltage set in the Coulomb blockade regime. The downward signal jump at $t = 0$ suggests the photo-excited electron trapping, followed by an upward signal jump originating from escape

of the trapped electron. The authors proved that the electron trapping time is tunable by gate voltage from shorter to longer time range than the spin-flip time T_1 . Further discussion about spin dependent tunneling caused by the spin-resolved edge states under finite magnetic field implies the possibility of photoelectron spin readout in this system.

The upper experiment showed the trapping and resetting of single photoelectrons using a GaAs HEMT wafer. Disadvantage of this scheme is the discrimination strongly relies on the low noise and stable charge sensing, which depends on sample to sample and sometimes difficult to control. where the absorption of photons occur in the GaAs buffer layer. Moreover, though conduction band electrons are confined in the triangular potential, the buffer layer is assumed as a bulk-like property for a photo-excitation. GaAs bulk states do not satisfy the coherent transfer scheme. Nevertheless selective electron spin excitation is not perfect since LH and HH states are degenerate, therefore double heterostructure QWs are preferable for spin excitation experiments.

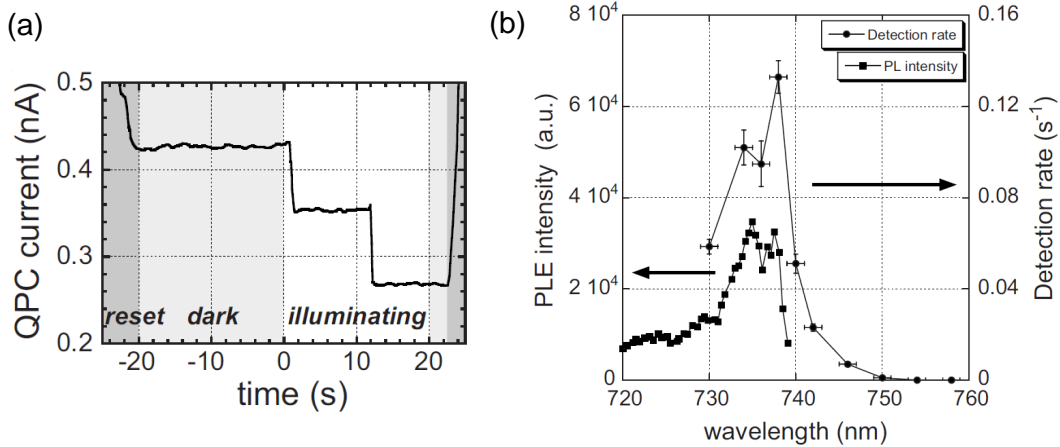


Figure 4.2: (a) Time dependence of the QPC current with and without the light exposure. The QPC current suddenly decreases due to a change in the electron number. (b) The detection rate of the photoexcited electrons and the PLE spectrum of the same QW structure as a function of incident photon wavelength. Single photoelectron trapping efficiency obeys the two dimensional nature of absorption.

Evidence of trapping the photoelectron excited from a QW structure is re-

ported in Reference [28]. In this work, they fabricated a single QD on a QW wafer, and photons were irradiated continuously in the order of seconds. The experimental response of the QPC current while irradiation is shown in Fig. 4.2(a) where single photoelectron trapping is eventually observed as a step decrease in the current. They took the statistics of the photoelectron trapping events and plotted with respect to the incident laser wavelength (Fig. 4.2(b)). Plots are also shown for photoluminescence excitation measurements done on a QW describing the selective absorption at the HH and LH states. The roughness of the plot differs but these two traces have similar dependence with two peaks around $\lambda = 735$ nm. The result shows that absorption properties for exciting the lateral dot would also obey the bare QW nature. This implies that the coherent transfer scheme explained by the QW structure modulation is applicable to the lateral dots, an additional support towards single photon to single electron spin coherent transfer. However, using a cw laser cannot control the timing of the photoelectron trapping and the reset of photoelectrons has not been demonstrated in their experiments. Towards the high fidelity coherent transfer between single quanta, pulsed measurement, more accurate and electrically controllable single photoelectron spin detection has to be developed using QD devices based on the QW.

Chapter 5

Experimental conditions

5.1 Characterization of quantum wells

One of the most crucial issues in this study is to design and characterize QW wafers which are suitable for the coherent transfer experiment. In general, the wafer profiles should be investigated in terms of g -factor engineering, QD fabrication, and optical properties. First, the electron g -factor in the QW has to be small enough, ideally zero, compared to the light hole g -factor, but a too small g -factor is not desirable since a finite Zeeman splitting is practically required for spin readout and manipulation. Second, the 2DEG in the QW should be well-designed and clean enough to form lateral QDs. In particular, the carrier density and mobility are important parameters to form QDs having just a few electrons. Third, it is necessary to estimate the excitation energy of electrons from the heavy and light hole bands to the conduction band in the QW. In this section, systematic characterization of QW wafers by means of magnetotransport measurement, fabrication of DQDs, and setup for photon irradiation onto the QD are introduced.

5.1.1 Wafer structures and band calculations

Double heterostructure wafers with various QW widths are grown by molecular beam epitaxy (MBE) by the NRC-CNRC group (N-J63, N-J65, N-J67, N-J107, N-J108, and N-J109) and Ruhr-University Bochum group (B-14155). Figure 5.1 shows the structure of these wafers and the corresponding band profile calculated by a self-consistent 1D-current Poisson method using Nextnano++ (Walter Schottky Institut). A GaAs capping layer is deposited on top of the wafers,

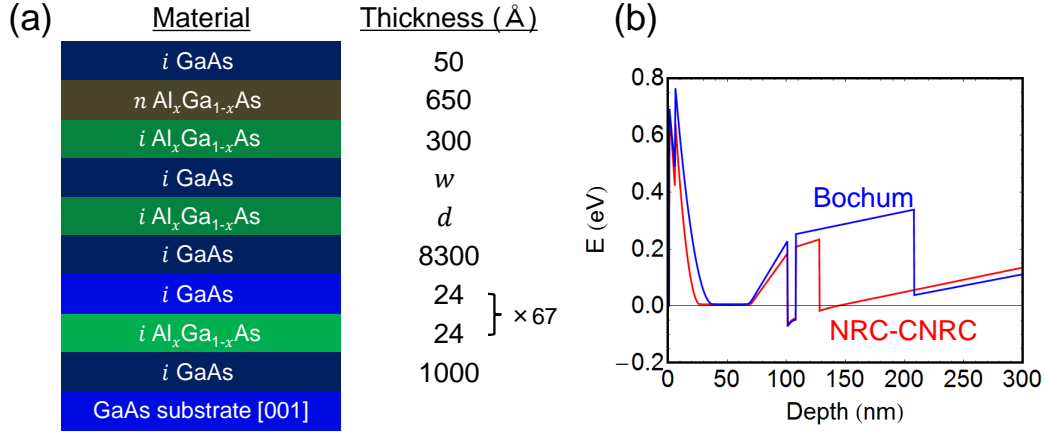


Figure 5.1: (a) A schematic view of the wafer structure for the g -factor engineered QWs. Thickness of each layer is listed in the right side of the figure. (b) The calculated band profiles of each designed wafer with QW thickness $w = 7$ nm, where the depth is measured from the surface of the wafers. The barrier layer d was made thicker to reduce the tunneling of photoelectrons created at the GaAs buffer layer [81].

in order to avoid oxidization of the AlGaAs layer. A Si-doped AlGaAs layer with thickness of 65 nm is spatially separated from the AlGaAs/GaAs/AlGaAs QW by a 30 nm intrinsic AlGaAs layer. Underneath the well structure are an intrinsic GaAs layer, a GaAs/AlGaAs superlattice structure, and another GaAs layer on top of a semi-insulating [001] GaAs substrate.

The varied parameters of each wafer are summarized in table 5.1. In the wafers from NRC-CNRC the QW width dependence of the electron g -factor for both two-dimensional electron gas and QD is systematically studied. Espe-

cially in the QD measurement, the designed wafers are found to suffer from frequent charge noise which causes a serious difficulty in performing spin-readout measurements. For this reason, we decreased the Si doping concentration and increased the aluminum content for the Bochum wafer to suppress tunneling of electrons from the top gates to the two-dimensional electron gas. We also found in the magnetotransport measurement and 1D-band calculation that some wafers from NRC-CNRC showed parallel conduction at the interface between the AlGaAs barrier layer and the GaAs buffer layer. As in Fig. 5.1(b), the conduction band at depth = 130 nm is below the Fermi level, leading to unintentional accumulation of a considerable amount of charge. To avoid this we made the bottom well barrier thicker, which also resulted in the improvement of the photon irradiation experiments as discussed in Ch. 6.

Table 5.1: Summary of wafer parameters

	Si dope conc. [cm^{-3}]	Al content	w [nm]	d [nm]
NRC-CNRC	2×10^{18}	0.265	4.8 ~ 13	20
Bochum	1×10^{18}	0.34	7.3	100

5.1.2 2DEG electron spins

Several important parameters characterizing a 2DEG in the QW wafers are extracted from magnetotransport measurement. The samples are prepared by etching the wafers into a Hall-bar pattern of size $300 \mu\text{m} \times 90 \mu\text{m}$. The following measurements were performed in a variable temperature cryostat and Heliox ^3He insert (Oxford) which can apply perpendicular magnetic field up to 10 T. Magnetoresistivity is measured by a conventional four-probe method, and the sample is inserted at the end of a cavity waveguide to enable resistivity-detected electron spin resonance measurements [82].

Figure 5.2(a1) shows the longitudinal and transverse magnetoresistivity (ρ_{xx} and ρ_{xy}) for wafer N-J65 ($w = 7 \text{ nm}$) at various temperature conditions. Typical

5. Experimental conditions

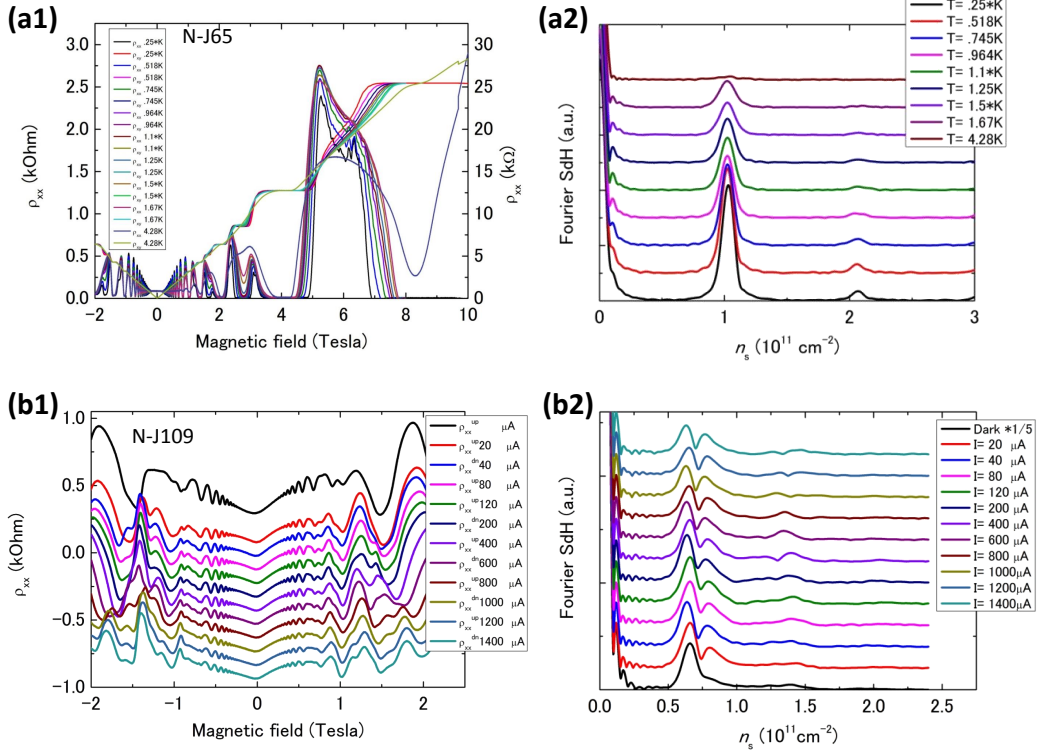


Figure 5.2: (a1) Measured transverse and longitudinal resistivity for wafer N-J65 as a function of magnetic field for several temperatures. Shubnikov-de Haas (SdH) oscillations and quantum Hall effect are clearly observed. (a2) The corresponding Fourier transform of the SdH signals. (b1) SdH oscillations measured for wafer N-J109. (b2) The corresponding Fourier transform of the SdH signals, showing the clear peak splitting with increasing intensity of light illumination.

Shubnikov-de Haas (SdH) oscillations with period proportional to $1/B$ are observed in the longitudinal resistivity. The peaks correspond to different Landau levels, and clear peak splitting emerges as magnetic field is increased and the temperature is decreased. A step-like structure can be seen in the corresponding transverse resistivity coming from the quantum Hall effect. Resistivity plateaus at $h/e^2 = 25.8 \text{ k}\Omega$ at $B > 7 \text{ T}$, where we can determine the filling factor $\nu = 1$. The Fourier transform of the longitudinal resistivity with $1/B$ is plotted in Fig. 5.2(a2). At low temperature, there is a small peak at the carrier density

$n_s = 2.1 \times 10^{11} \text{ cm}^{-2}$, originating from the total population of electrons in the QW. The populations of both up- and down-spin electrons are $n_s = 1 \times 10^{11} \text{ cm}^{-2}$, which can be seen as a large peak at the corresponding carrier density. Furthermore, the mobility μ is calculated from the conductivity $\sigma_{xx}(B = 0)$ and carrier density using the Drude model ($\sigma_{xx}(B = 0) = n_s e \mu$).

Although the carrier density for most of the wafers are correctly determined, wafers with well width about 6 nm (N-J63 and N-J109) showed two neighboring peaks in the Fourier transform of longitudinal resistance (Fig. 5.2(b1) and (b2)). This unexpected result infers the contribution from two distinct types of carriers. We speculated that an electron channel exists not only in the QW but also at the deeper AlGaAs/GaAs heterostructure. As can be seen in Fig. 5.1(b), the conduction band at depth = 130 nm is below the Fermi level, indicating the possibility of an unintentionally formed 2D electron system. We further performed 1D Schrödinger-Poisson band calculation using Nextnano++ for various well widths, and found the considerable electron accumulation at the deeper heterointerface for well widths less than 7 nm. Especially for much thinner wells, most electrons are confined at the heterointerface instead of the QW region, which agrees with the case of wafer N-J108 where only a single peak in the Fourier transform is observed. The calculation also suggests that to avoid parallel conduction, the bottom AlGaAs barrier should be designed thick enough to lift the conduction band above the Fermi surface at the heterointerface.

Next, electron spin resonance measurements are carried out to deduce the electron g -factor in QWs with various well widths. The electron g -factor calculated from spin splitting of Landau subbands is known to be largely enhanced by the exchange interaction [83]. Instead, the “bare” g -factor of electron is accessible by the above ESR technique. Figure 5.3 top is the magnetoresistivity difference between the cases with and without microwave excitations for various frequencies. To see the electron spin flip excitation, the magnetic field is swept in the odd number filling factors, where a peculiarity in the conductivity is expected at the condition $hf_{\text{MW}} = g\mu_B B$, where f_{MW} is the excita-

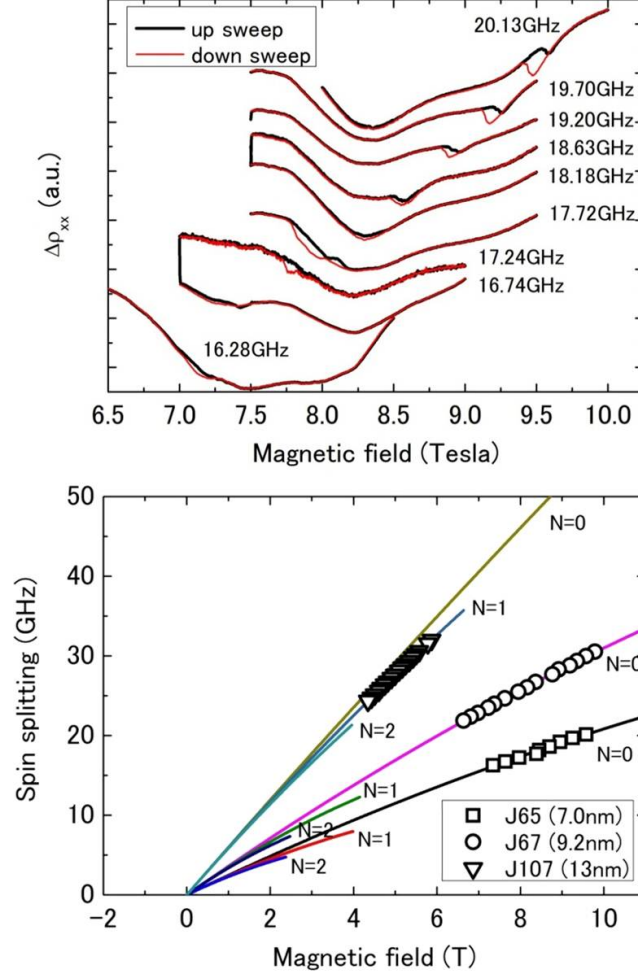


Figure 5.3: (Top) Difference of magnetoresistivity with and without applying microwave in the wafer N-J65. Small peak in the up sweep originates from the electron spin resonance. The up and down sweep shows the hysteresis, indicating the dynamical nuclear polarization. (Bottom) Extracted spin splitting energy from the electron spin resonance signal as shown in the upper figure. To evaluate the electron g -factor in the perpendicular magnetic field, measured splitting energy values for three different wafers are fitted with the equation introduced in the main text.

tion microwave frequency and μ_B is the Bohr magneton. One can see small peak structures in the up sweep (black curves), indicating that the spin flipped electrons are scattered to the opposite edge channel and hence suppress the

conductivity. The existence of microwave excitation involving electron spin flip process is more clearly seen from the hysteresis between up and down sweeps, since the ESR signal measured in the downward sweep suffers from dynamically polarized nuclear spins, which is known as the Overhauser effect. The magnetic field dependence of resonant frequency, Zeeman splitting energy is plotted in Fig. 5.3 bottom. Here, solid lines are fitting curves with an expression $hf_{\text{MW}} = [g_0 + c(N + 1/2)]\mu_B B$, where g_0 is the bare g -factor, c is a parameter depending on heterostructure, and N is the Landau level index [84].

5.1.3 Summary of wafer profiles

The extracted parameters for each wafer are listed in Fig. 5.4(a). As discussed above, two values of carrier density are obtained for N-J63 and N-J109, one of which corresponds to the unintentionally accumulated carriers at the deeper heterojunction. For these wafers, we could not find any ESR signal under microwave excitation. For wafer N-J108 with thinner well, the obtained g -factor is consistent with the typical g -factor in a GaAs/AlGaAs heterostructure [82]. This supports the hypothesis that the contribution from electrons in QW is negligibly small compared to the unintentionally formed electron system because the lowest electronic state in the thin well could be above the Fermi energy, and thus the g -factor value reflects the single-heterostructure case rather than the double-heterostructure case.

In Fig. 5.4(b), the estimated g -factor values for wafers N-J65, N-J67, N-J107 and B-14155 are plotted in comparison with experimental data reported in Ref. [44]. With the well width of 13 nm, the g -factor value is similar to that of the conventional HEMT case, and the g -factor decreased down to 0.12 in narrower QWs. Note that although it may be difficult to experimentally determine the sign of the electron g -factor in an electrical measurement, one can readily deduce it by referring to the previous study demonstrating the monotonic change of the g -factor with decreasing well width performed in optical measurements. The behavior of the g -factor is in good agreement with the previous results and

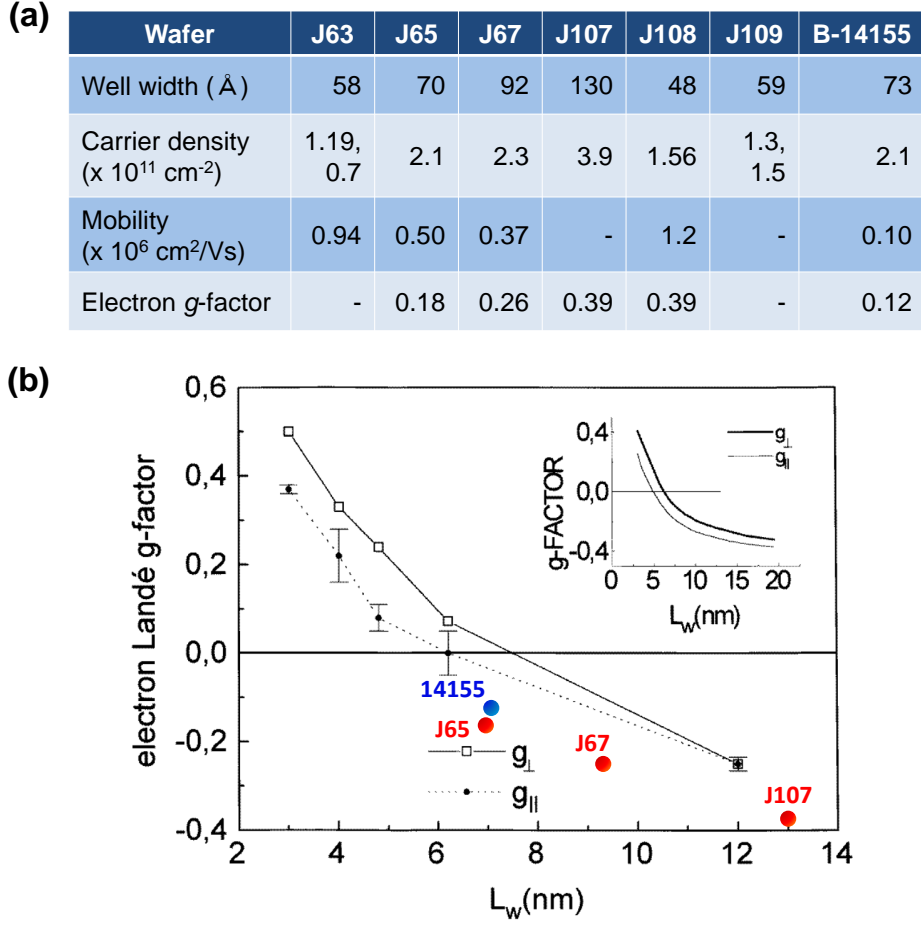


Figure 5.4: (a) Summary of the extracted parameters for the QW wafers. Two values of carrier density are shown for N-J63 and N-J109, due to the parallel conduction. (b) Comparison of the measured g -factors with a previous study [44].

theoretical calculation if one assumes that all the obtained g -factor values are negative. The offset from the previous study may come from the difference of wafer structure particularly the Al content. It should be emphasized that the g -factor is measured for an out of plane magnetic field, while the coherent transfer experiment must be performed in an in-plane magnetic field. As in Ref. [44], the g -factor for in-plane magnetic field is anticipated to be positively larger. By taking the anisotropy into consideration, we can expect that the in-plane electron g -factor is less than 0.1, which should be small enough to

perform the coherent transfer in V-shaped three-level systems. Quantitatively, in the QW with electron g -factor of 0.1, the Zeeman splitting energy $g_e\mu_B B$ at $B = 6$ T is $35 \mu\text{eV}$, which is about 20 times smaller than the bandwidth of the wavelength-tunable Ti:Sapphire laser.

5.2 Lateral quantum dot devices

In this section, the design of the QDs and the experimental setup for detection of single photon response in the QD is briefly introduced. Using the same wafer profiles as in the magnetoconductance measurement, we initially fabricated single QDs to estimate the electron g -factor in a QD, which may differ from that of a 2DEG due to additional confinement. The results are summarized in Appendix A. Simultaneously, we designed and made DQD devices to see the single photon response and construct an electron spin-readout scheme. The combination of these two techniques enables us to perform the real-time detection of transfer from single photon polarization to single electron spin.

Double quantum dots

In high-mobility two-dimensional electron systems with carrier density about $10^{11} - 10^{12} \text{ cm}^{-2}$ and mobility about $10^5 - 10^6 \text{ cm}^2/\text{Vs}$, the long Fermi wavelength and large screening length allows us to locally deplete electrons by applying voltage to the top gates. From this point of view the gate structure should be carefully designed based on the depth and the carrier density of the 2DEG. We performed an electrostatic potential calculation for various gate designs to optimize the dot structure, and one of the results for two types of the DQDs are demonstrated in Figs. 5.5(a) and 5.5(c). Although this calculation does not give quantitative results for e.g. pinch-off voltage between two gates, it is still instructive to check whether the confinement potential to make the QD is formed in the intended position. Figures 5.5(b) and 5.5(d) show the scanning electron micrograph pictures of fabrication test samples. The device shown in Fig. 5.5(b) is fabricated on a single heterojunction wafer from Sumitomo

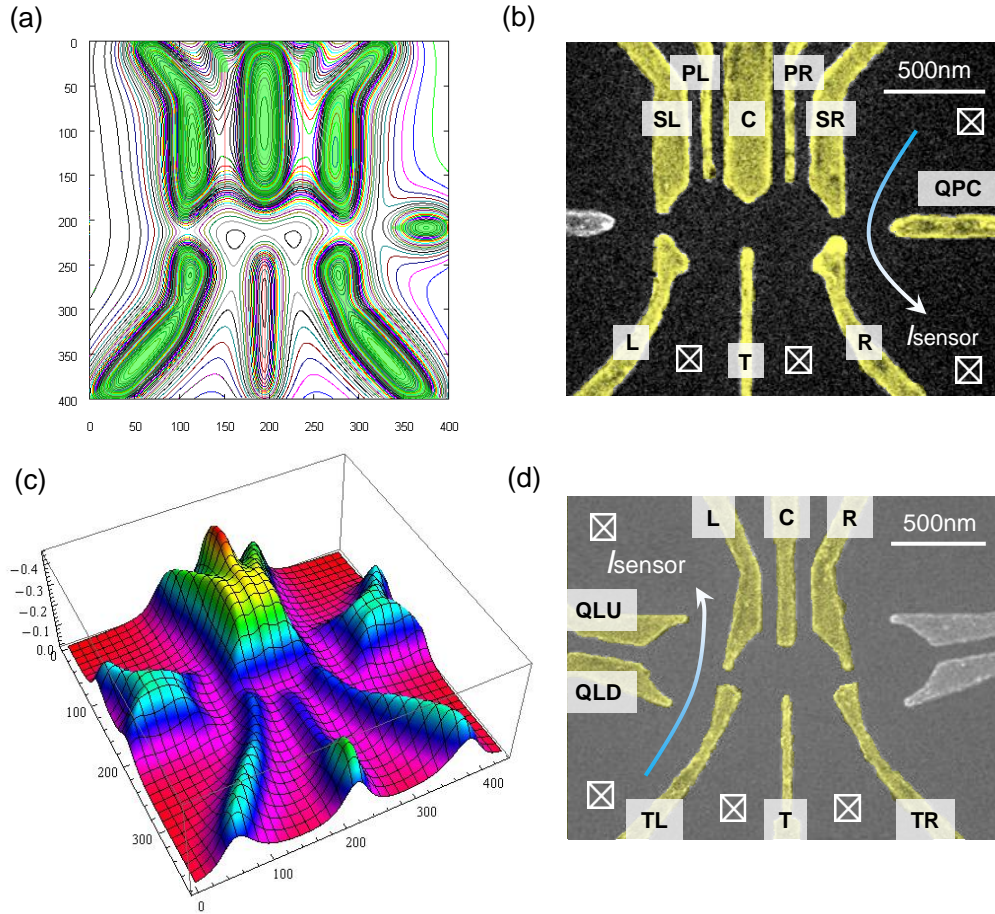


Figure 5.5: (a) A 2D and (c) a 3D contour plot of the electrostatic potential calculation for a designed DQD, corresponding to the SEM images of fabricated DQDs on (b) a HEMT wafer (S-72) and (d) a QW wafer (B-14155).

Denko (S-72) for the initial measurements on the single photon detection using resonance inter-dot tunneling. The current through the dot is monitored using Ohmic contacts, and a QPC charge sensor is fabricated for electron number counting. The device in Fig. 5.5(d) is made on wafer B-14155 to carry out the real-time spin blockade and photoelectron spin detection experiments. In these devices a QD charge sensor is implemented instead of a QPC charge sensor, which is revealed to achieve higher sensitivity to electron charging in

the measured QDs [63].

The schematic view of the DQD device structure is depicted in Fig. 5.6. Calixarene resist acting as an insulating layer is coated on top of the wafer, and a 300 nm thick Ti/Au metal aperture mask with a 400 nm diameter hole is put such that light irradiated from the top side can only reach the QD region. The combined SEM image of the DQD and aperture mask are shown in Figs. 5.6(a) and 5.6(b). Transmission rate of 780 nm wavelength light through the 400 nm diameter aperture to the 2DEG is $\sim 1/3$, derived by FDTD calculation.

In the following experiments a bias-cooling technique is effectively utilized to reduce charge noise. In this technique a positive voltage is applied to each metal gate during sample cooling such that carriers flowing from the 2DEG to the gates are gradually trapped by DX centers or other trap sites making these noise sources inactive [85]. Furthermore, the metal aperture mask is used as a capping gate, which is also crucial for noise reduction [86].

5.3 Electronic and optical measurement systems

Electronics setup

Electrical transport measurement and real-time photon detection in lateral QD samples are executed in a setup shown in Fig. 5.7. Most experiments including photon irradiation measurement are performed in a cryogen free $^3\text{He}/^4\text{He}$ dilution refrigerator ‘Triton 200’ (Oxford Instruments) with an optical window on the bottom and base temperature of 25 mK. The exception is the irradiation measurement of a DQD on wafer S-72 for which we used a ‘Spectromag’ with a top loading ^3He insert (Oxford Instruments). The voltage applied to Schottky gates and Ohmic contacts are controlled by voltage sources in an ‘IVVI-DAC2-Rack’ (Delft University of Technology), and current signals through the dots and QPC charge sensors are translated into voltage by current amplifiers ‘model 1211’ (DL Instruments) and are read out by voltage meters in ‘HP 4142B’ (Ag-

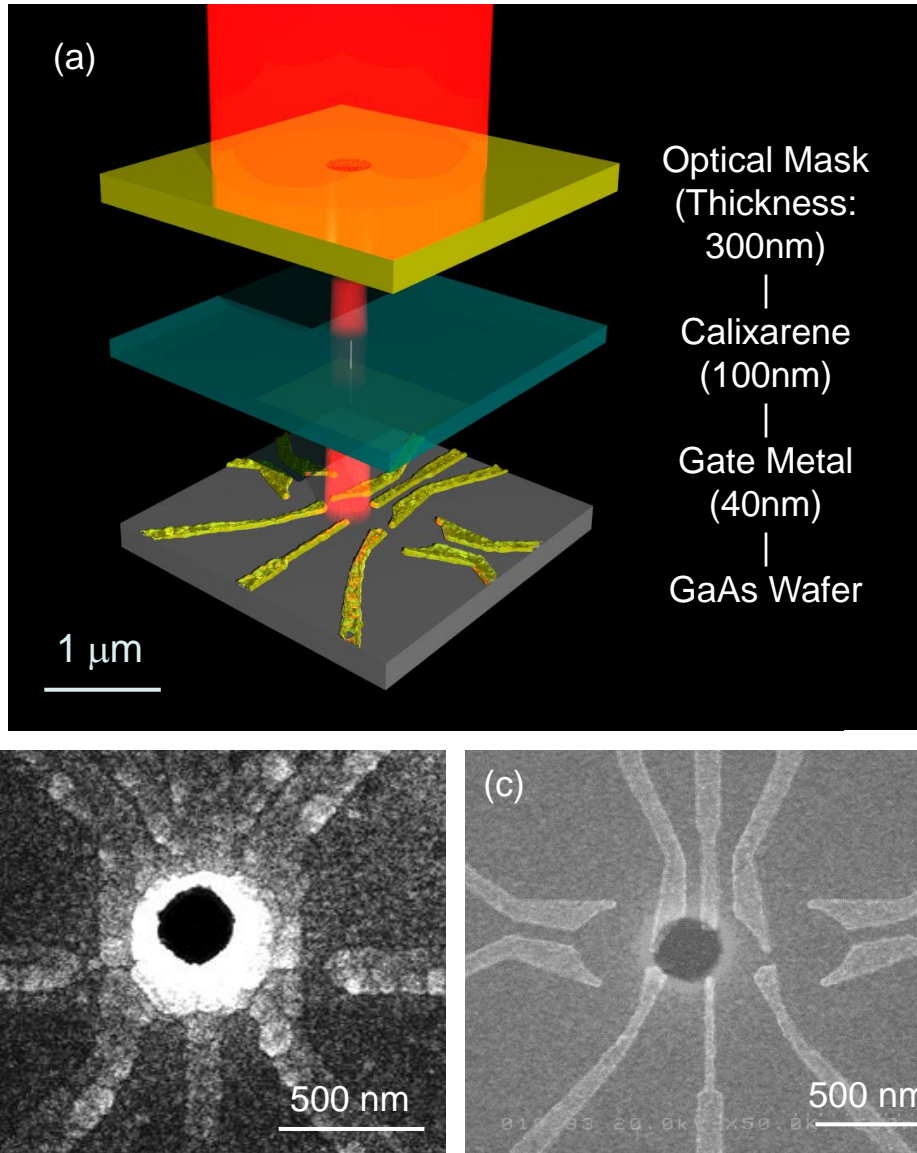


Figure 5.6: (a) A schematic of the DQD for photon irradiation measurements. 100 nm thick insulating layer is coated to avoid electrical short circuit between aperture mask and fine gates forming the dot. (b) An SEM picture taken for the S-72 wafer sample after the fabrication of the top most metal optical mask. The diameter of the aperture is 400 nm centered on the double dot. (c) A synthesized image for the B-14155 wafer of a DQD with a metal aperture mask.

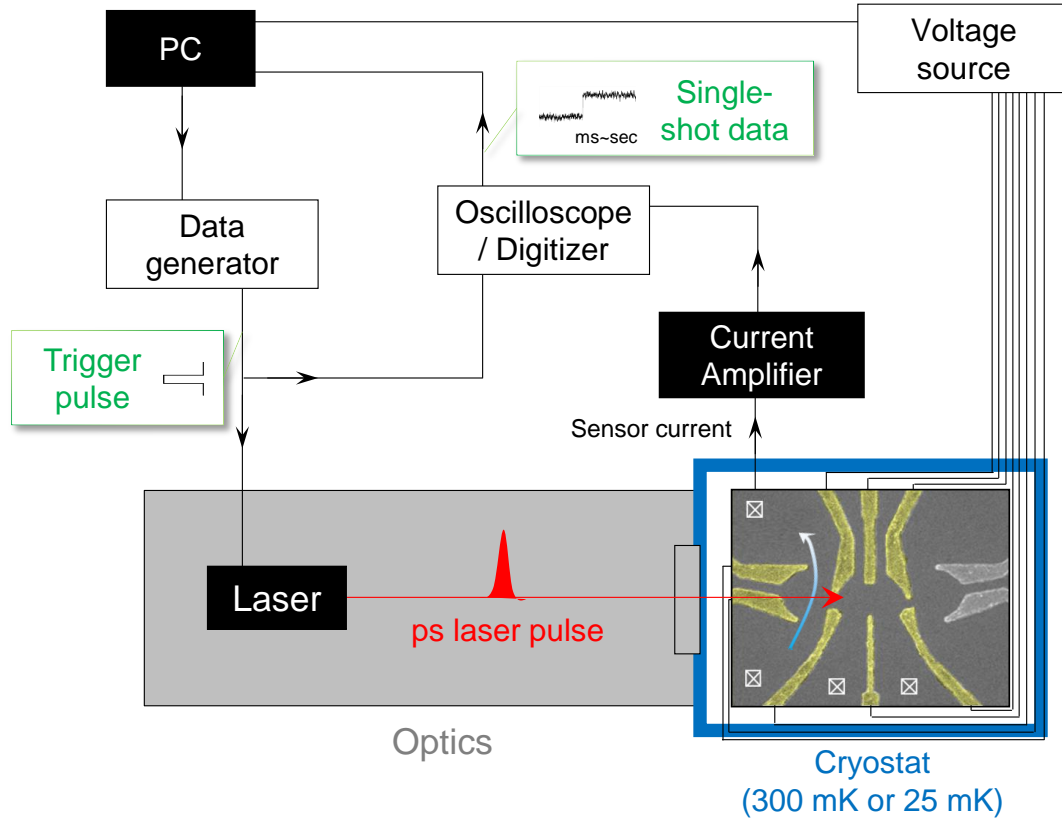


Figure 5.7: Experimental setup for electrical and optical measurement of DQDs.

ilent). In parallel, the transformed voltage signal from the QPC current can be monitored by a digitizer ‘PXI-4462’ (National Instruments) for fast data acquisition. The real-time QPC signal is measured on an oscilloscope ‘DPO4032’ (Tektronix) or the digitizer. It should be noted that the minimum rise time is limited by a circuit inside the current amplifier. The rise times are $40 \mu\text{s}$ and $250 \mu\text{s}$ for the mainly used gains 10^8 A/V and 10^9 A/V respectively.

Single-shot irradiation measurements are triggered by a pulse pattern generated from a Data Generator ‘DG2040’ (Tektronix). The trigger pulse is sent to the laser source and to the digitizer/oscilloscope simultaneously so that the real-time response of before and after pulse irradiation is acquired. Note, the

laser pulse width is in the scale of picoseconds which is unresolvable to the electronics. Finally the single-shot time resolved voltage data is sent to the PC with the desired data length and resolution permitted by the digitizer/oscilloscope.

Optics setup (0.3 K fridge)

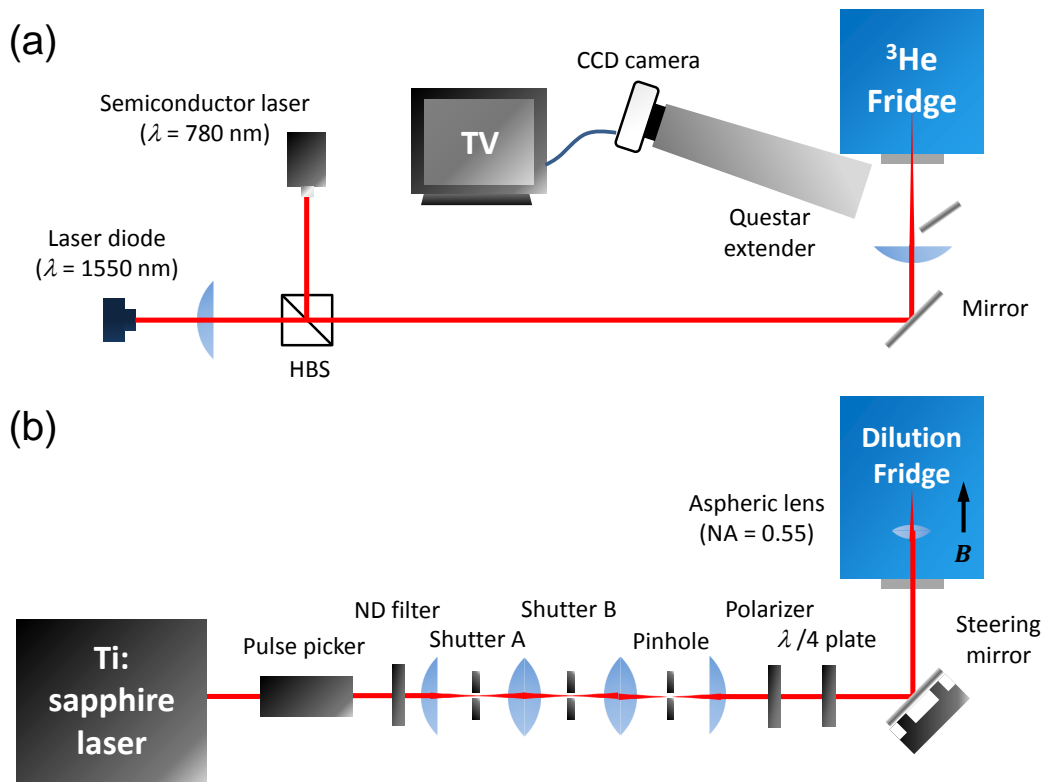


Figure 5.8: Optics setup for the photon irradiation experiment. (a) A setup with a semiconductor laser. (b) A setup with a wavelength-tunable Ti:Sapphire laser. A pulse picker and shutters are used to enable single-shot irradiation.

Next, two types of optics setup are illustrated in Fig. 5.8. Figure 5.8(a) is adopted for the photon-charge conversion experiment. In this setup, a pulsed semiconductor laser ‘PiLas’ (Advanced Laser Diode Systems) with wavelength $\lambda = 780 \text{ nm}$ and a near infrared laser diode ‘ML925B45’ (Mitsubishi electric) with wavelength $\lambda = 1550 \text{ nm}$ are aligned to focus on a GaAs QD sample loaded

in a ^3He cryostat. The position of the laser beam spot is directly monitored on a TV display by either a Si or InGaAs CCD camera (Hamamatsu Photonics) through a Questar extender QM100. Beam spot diameters of the semiconductor laser and the near infrared laser diode are the order of $300\ \mu\text{m}$ and $1\ \text{mm}$ on the sample. The photon irradiation experiment is performed by generating a single pulse of width of $34\ \text{ps}$, and the laser power is adjusted by the controller. The near infrared laser diode is used not only for rough alignment of the laser beam with InGaAs CCD camera, but also for resetting excited charges from DX centers inducing persistent photo-conductivity in GaAs systems [87, 88].

Optics setup (wavelength-tunable)

Figure 5.8(b) depict a specialized setup in a polarized photon irradiation experiment using a wavelength-tunable laser. In this setup, picosecond-pulses are generated by a mode-locked Ti:Sapphire laser ‘MIRA Model 900-P Laser’ (Coherent) and a single pulse is extracted by ‘Model 9200 Pulse Picker’ (Coherent). However due to the finite on-off ratio of $500 : 1$ of the pulse picker, a weak leakage pulse train of $72\ \text{MHz}$ is present. To cut off the leakage light from the pulse picker two mechanical shutters are prepared. The first shutter is ‘normally on’ and the second is ‘normally off’ state. Just before a laser pulse is picked the second shutter is opened, and after the pulse emission the first shutter closes. Consequently the time duration with both shutters opened is tuned to be roughly $10\ \mu\text{s}$, avoiding unintentional passage of laser pulses. The laser power is tuned by ND filters integrated into a wheel filter selector ‘FW102’ (Thorlabs). Again, the near infrared laser diode is aligned to the wavelength-tunable laser beam. The linear polarization of the laser beam is created by a polarizer (Thorlabs) and tuned by a $\lambda/4$ quartz waveplate ‘WPQ-7800-4M’ (Sigma Koki). The focused position of the laser beam spot is finely controlled by a fast steering mirror ‘OIM202 FSM’ (Optics In Motion) placed on bottom of the cryostat.

The alignment of the laser beam is achieved by measuring the photocurrent while scanning the laser beam by sweeping the angle of the steering mirror. Ob-

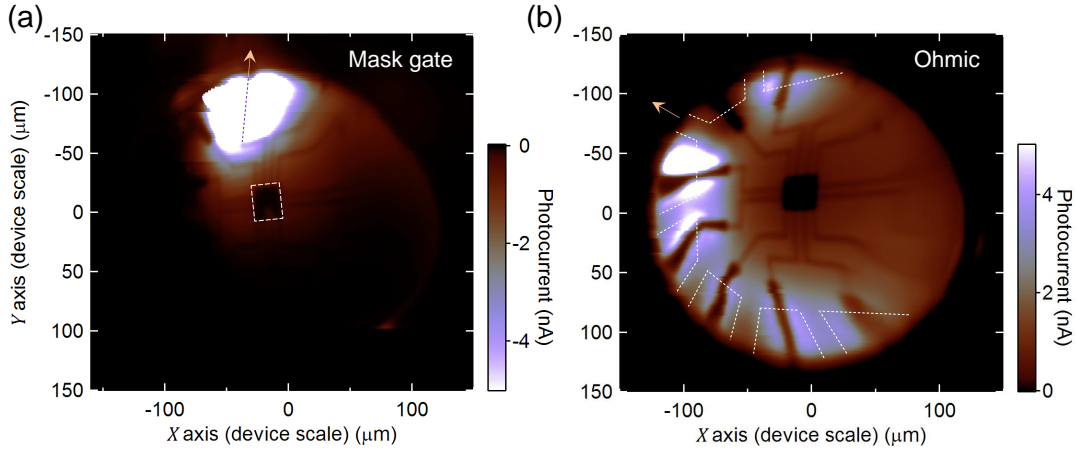


Figure 5.9: (a) An image of the photocurrent measured while scanning the laser beam. The current was measured through the electrode of the mask gate. The dashed rectangle shows the area of the mask gate. The arrow shows the direction of the connected electrode. (b) Similar plot with the photocurrent measured through one of the Ohmic contacts. The dashed line outlines the MESA. The arrow is the path towards the connected Ohmic contact.

ervation of the photocurrent of the sample does not affect the sample quality as long as it is performed at room temperature. However at low temperatures some of the photo-generated carriers would freeze in the doping layer and change the intrinsic electrostatic potential from the initial condition. Therefore reducing the area of irradiation to the MESA structure is crucial for our low temperature irradiation measurements. The sample is irradiated with a continuous wave mode laser beam after sufficient beam focusing to resolve the gate patterns. Figures 5.9(a) and 5.9(b) are the images taken while scanning the laser beam over an aspheric lens with effective focal length of 2.75 mm ‘C390TME-B’ (Thorlabs). The lens is mounted on a sample holder and fixed at a distance slightly offset from the focal length. With this offset we can tune how far the beam spot can be moved laterally on the sample. The beam is moved by changing the angle of the steering mirror. The laser spot on the sample surface is focused below 10 μm width, checked using a beam profiler in advance. The figures showed the gate electrodes with width of 2 μm at laser intensities over a

few 100 μW . From the positions and shape of the obtained photocurrent images, we align the beam at the center of the mask gate.

Chapter 6

Single photoelectron trapping in a double quantum dot

In this chapter we demonstrate one and two photoelectron trapping and the subsequent dynamics associated with inter-dot tunneling in DQDs over a time scale much smaller than the typical spin relaxation time. Photoelectron trapping in single QDs has been demonstrated using a nearby charge sensor [27, 28, 30, 89] but progress in spin detection was limited due to the destructiveness of the photoelectrons. Although charge sensing is accurate enough to detect the spins in a single-shot manner, photo-irradiation has non-negligible influence on dot energy levels as well as signal to noise level. Irradiation can induce additional current fluctuations on the charge sensor signal due to persistent photoconductivity that would reduce the fidelity of charge and spin detection. In order to overcome this difficulty, non-destructive spin detection with double quantum dots (see §3.3.3) could offer a better detection scheme. The first step towards this goal is to observe the single photoelectron trapping and its subsequent inter-dot tunneling in a double quantum dot.

6.1 Photoelectron trapping process

Two types of wafers are discussed in this chapter. The first is the single hetero-
junction wafer (referred as a ‘HEMT’ wafer). The single electron-hole pair ex-
citation mechanism and photoelectron trapping in a single QD is well explained
in Reference [30]. To compare the improvements made for a DQD, we initially
measured photoelectron trapping on a DQD fabricated on the HEMT wafer.
The second is the double heterostructure wafer (referred to as ‘QW’ wafer). By
following this measurement technique previously developed the HEMT sample,
we can confidently search the appropriate excitation wavelength and absorption
efficiency in the QW wafer. A double heterojunction has a non-uniform photon
absorption spectrum due to additional confinement of holes. Therefore, inves-
tigation of photoelectron trapping by varying the incident photon wavelength
to selectively excite the HH and LH states is important compared to the single
heterostructure case. A HEMT wafer (S-72) and a QW wafer with well width
of 7.3 nm (B-14155) was used for the measurements. The wafer specifics and
each of the used electronics and optics setups are explained in Ch. 5.

In the HEMT sample, photons are mainly absorbed in the GaAs buffer
layer under the DQD, and then the built-in electric field of the heterostructure
separates the electron-hole pair [30]. The potential drives only the electron into
the DQD, resulting in a single photoelectron trapping in the DQD. On the other
hand, for a QW sample, after an electron-hole pair creation in the DQD (Fig.
6.1(a)) the hole would move laterally towards the negatively biased electrodes
since surface gates efficiently separate the electron-hole pair [90]. This would
also result in a single photoelectron trapping in the DQD. After trapping the
photoelectron, non-destructive photoelectron detection is achieved by setting
the DQD on a resonance condition so that the electron tunnels between the
dots from either side (Fig. 6.1(b)). The inter-dot tunneling signal is detected by
the nearby charge sensor in a real-time manner. The detection resolution of the
single inter-dot tunneling is determined by the band width of the setup, however,
repetitive inter-dot tunneling provides a more favorable detection signal since

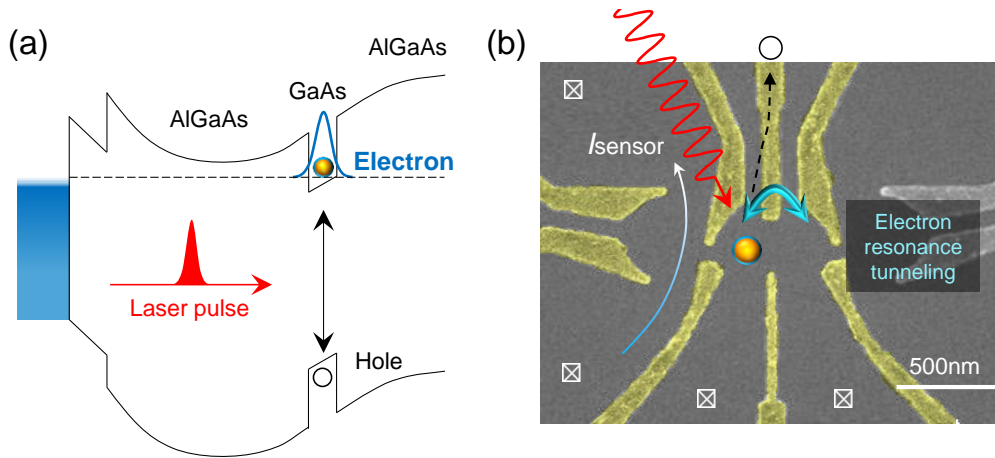


Figure 6.1: (a) A schematic representing the photo-excitation of a QW using the band energy profiles. Filled and open circles represent the excited electron and hole respectively. (b) After an electron-hole pair is created the hole is removed (dashed black line) and only the electron is trapped in the QD due to the external electric field created by the electrodes. Our scheme of photoelectron trapping is to detect the resonance tunneling of a photo-excited electron in a real-time manner.

it offers step signals for multiple times. As we will see, this detection scheme does not only improve the signal visibility against current fluctuations but also reveals the spin dynamics while trapped in the DQD.

6.2 Non-destructive photon detection in a double quantum dot

Measurement condition (S-72 sample)

First, the DQD is tuned to a tunneling condition where the inter-dot tunneling is observed in real-time. The charge states in the DQD were measured with a QPC charge sensor which has sufficiently higher sensitivity to the charge occupation in the right dot compared to the left dot. The electron number in each dot was counted by analyzing the QPC transconductance $G_{\text{QPC}} = dI_{\text{QPC}}/dV_L$, where I_{QPC} is the QPC current and V_L is the voltage applied to gate L. A lock-in

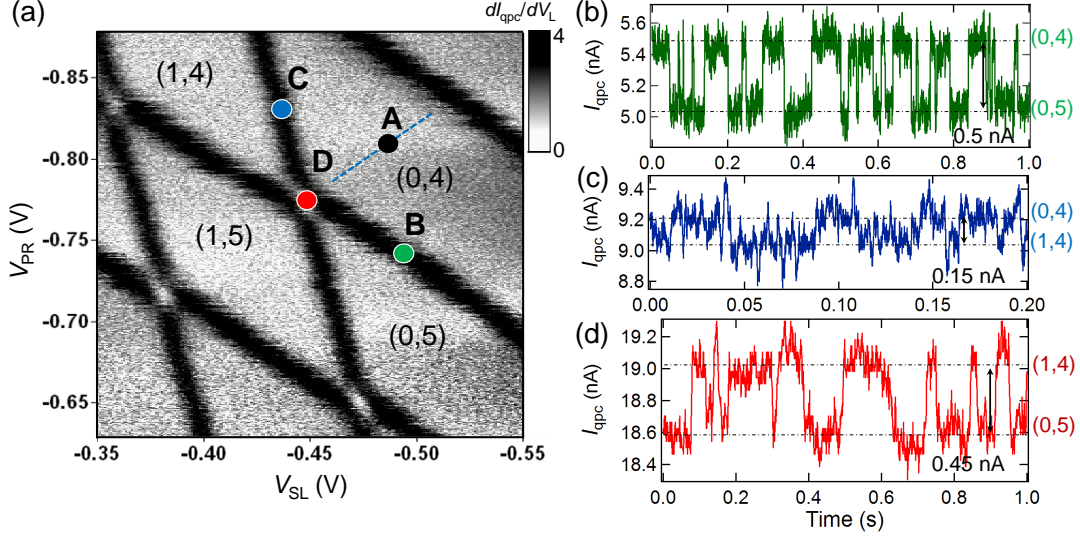


Figure 6.2: (a) Stability diagram of the DQD. The dot was initialized to state A(0,4) before light irradiation. (b-d) Real-time charge sensing traces of the DQD measured at the resonance points B(0,4)-(0,5), C(1,4)-(0,4) and D(1,4)-(0,5). The 0.5 nA step height in (d) indicates the inter-dot tunneling event of a single electron charge. Measurements were done at 0.4 K

technique with a modulation frequency of $f_m = 223$ Hz was used to obtain the charge stability diagram in Fig. 6.2(a). The (0,0) state was confirmed by applying sufficiently large negative voltages to the gates to ensure that no further lines appeared. Then the tunneling rates were tuned to be lower than the bandwidth of our setup so that real-time charge transitions were measurable. The QPC sensitivities were $2.5\% \times e^2/h$ (0.5 nA in Fig. 6.2(b)) for the right dot-lead tunneling, $0.5\% \times e^2/h$ (0.15 nA in Fig. 6.2(c)) for left dot-lead tunneling, and $2.0\% \times e^2/h$ (0.45 nA in Fig. 6.2(d)) for the inter-dot tunneling. Note that the signal amplitude of the inter-dot tunneling is mainly important in this study.

The initial charge state was set in the center of the (0,4) Coulomb blockade region ((A) in Fig. 6.2(a)) before laser irradiation. The inter-dot tunneling rate was adjusted ranging from $\Gamma_C = 10$ Hz to 1 kHz and the tunneling rate of the left (right) barrier was tuned to $\Gamma_L \approx 0.1$ Hz ($\Gamma_R \approx 1$ Hz) which is slower

than the inter-dot tunneling rate. This prevents the photoelectrons to escape from the DQD before the inter-dot tunneling is observed. After tuning the tunneling rates, the charge state was only able to be tuned to the (0,4) charge state. Here we set the (1,4) and (0,5) excited states on resonance (**A** in Fig. 6.2(a)). The number of electrons inside the DQD is not a fundamental matter in the measurements discussed in this chapter. Laser pulses are irradiated at this condition and, the charge number will increase to either (1,4) or (0,5) state by trapping a photoelectron. Inter-dot tunneling of this photoelectron is expected after a time depending on the inter-dot tunneling rate.

Non-destructive single photon detection

Figure 6.3 shows the the temporal charge sensor current (I_{QPC}) response upon laser pulse irradiation. The average incident photon flux was ~ 1.03 photon/pulse on the QD. Therefore, we expect the number of trapped photoelectrons varying from zero to one or two electrons upon a single pulse irradiation. When no photoelectrons are trapped, the irradiation response would only show a background shift (Fig. 6.3(a)). This is a persistent photoconductivity effect observed after every pulse irradiation that will be neglected from the irradiation response hereon. Figures 6.3(b) and 6.3(c) show the single photoelectron trapping by the left dot (b) and by the right dot (c), respectively. Single photoelectrons can be trapped by either dot because the aperture extend over both dots. After the initial increase of photoconductivity upon photon irradiation we observe an abrupt decrease of I_{QPC} by 0.5 nA at $t_{\text{trapL}} = 4.1$ ms in (b) and an I_{QPC} increase by 0.5 nA at $t_{\text{trapR}} = 4$ ms in (c). The I_{QPC} change is almost the same as observed in Fig. 6.2(d). Therefore the former is assigned to the charge state change from (1,4) to (0,5) and the latter to that from (0,5) to (1,4).

Figure 6.4 displays the single photoelectron trapping signal over a longer time range until the photoelectron escapes from the DQD. Upon laser pulse irradiation at time $t = 0$ the I_{QPC} abruptly increases and simultaneously starts to oscillate between two levels 0.5 nA apart. The first abrupt increase in the current is due to the addition of the persistent photoconductivity. The oscillat-

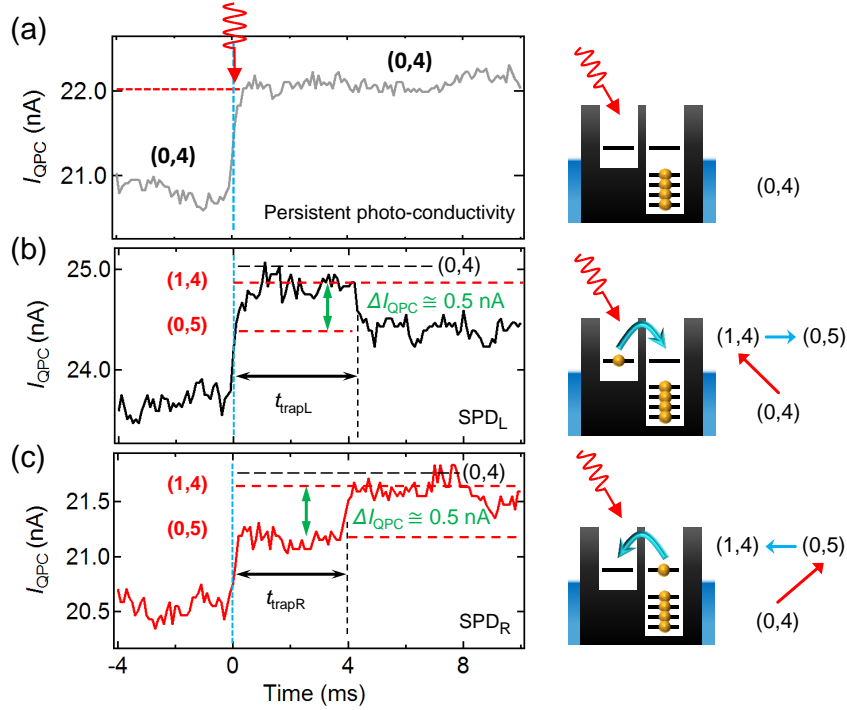


Figure 6.3: (a) Typical irradiation response with no electron trapped in the dot. (b, c) Real-time single-shot measurement of a single photon detection. The electrons are trapped initially (b) in the left dot or (c) in the right dot. The trapped electron resonantly tunnels non-destructively to the right dot with a given inter-dot tunneling rate. The captured position is inferred by the sign of the subsequent tunneling after irradiation. The average incident photon flux was ~ 1.0 photon/pulse on the QD.

ing signal represents the repetitive inter-dot tunneling of the photo-generated electron between the $(1,4)$ and $(0,5)$ states on resonance. Since the side barriers are made opaque enough, the photoelectron can repeatedly tunnel between the dots in the DQD for over 100 times before it escapes from the DQD. Thus the single photoelectron trapping measurement is non-destructive while the 0.5 nA fluctuation is observed. In the end, the dot is re-initialized to $(0,4)$ state when the electron escapes from the DQD, leaving a 0.15 nA increase on the current. Note that the I_{QPC} fluctuation due to resonant tunneling between $t = 0$ and t_{trap} is clearly larger than the noise fluctuations in I_{QPC} for $t < 0$ before the light irradiation and $t > t_{\text{trap}}$ after the escape of the photo-generated electron

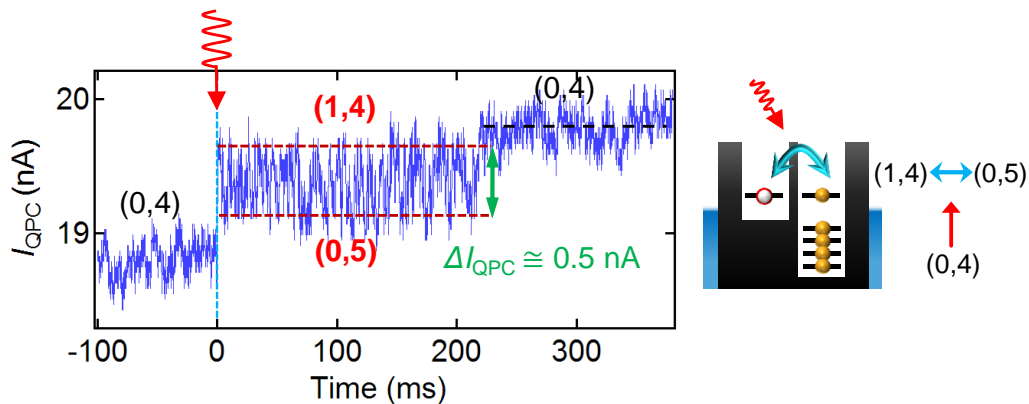


Figure 6.4: Single photoelectron trapping signal in a longer time range. The excess single electron shows repetitive inter-dot tunneling between (1,4) and (0,5) state as a large fluctuation in the QPC current. The electron escapes from the dot with a tunneling rate respective to either side of the barriers.

to the leads.

In a single QD, the photoelectron trapping was determined from the amplitude of a single step in the real-time signals. Persistent photoconductivity and low signal to noise ratio made the condition of this destructive detection very complicated. Here, the demonstrated non-destructive photoelectron trapping signal shows current fluctuation larger than the back ground noise, making the distinction between single photon detection and additional noise much easier.

Two photoelectron trapping

The fluctuation signal of single photoelectron trapping can be applied to investigate two photoelectron dynamics as well. Figures 6.5(a) and 6.5(b) show different types of I_{QPC} traces of two photoelectron trapping in the DQD. The traces were obtained in the same irradiation condition as in the previous section, but the detection rate of two photoelectrons was an order of magnitude lower than that of single photoelectrons. We see here that the inter-dot tunneling of photoelectrons were affected by the additional Coulomb interaction. For the two photoelectron trapping, the resonant fluctuation of I_{QPC} appears

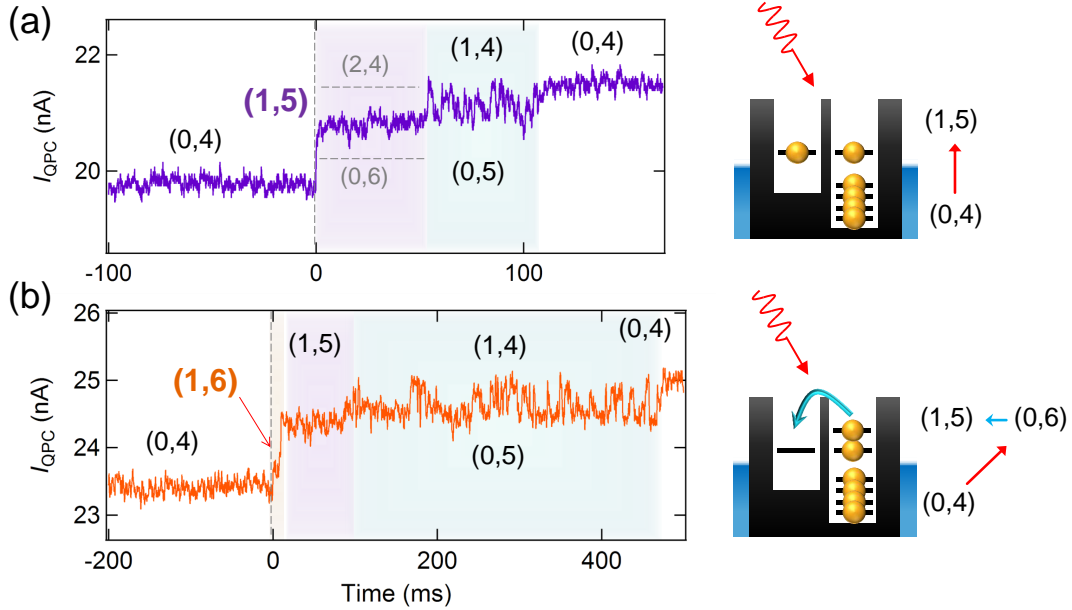


Figure 6.5: (a) Signal indicating two photon detection. After the irradiation, two photoelectrons fill each QD upon pulse irradiation. The sensor current starts to fluctuate after one of the two photo-generated electrons escapes from the DQD. (b) Signal when two photo-generated electrons were trapped both in the right dot. One of the trapped electron subsequently tunnels to the left and recovers an analogous signal to (a).

after an interval at a constant current. Considering that I_{QPC} is more largely reduced by charging of the right dot than that of the left dot, the region after irradiation in (a) is assigned to the (1,5) state (other possibilities of expected electron numbers are represented by the dashed lines). The two photoelectrons would occupy both of the resonant states and prevent the inter-dot tunneling due to Coulomb repulsion. As soon as one of the two photo-generated electrons tunnels off the DQD, the resonant tunneling is resumed. The rest of the signal is similar to the indication of single photoelectron trapping. Figure 6.5(b) shows a trapping event of two photoelectrons both trapped in the right dot. One of the two photoelectrons subsequently tunnels to the left, and then an analogous signal to Fig. 6.5(a) is recovered. Again the repetitive signal is only seen for the last photoelectron, since the first tunneling would be an inelastic process

that will not be repeated unless an additional energy is provided to overcome the Coulomb repulsion.

We performed 595 single-shot irradiation measurements and the resulting trapping rates of a photoelectron on the left dot, the right dot and two photoelectrons were 14.1 %, 19.3 % and 2.7 %, respectively. From these rates, the average rate of photons trapped in the dot is calculated as 0.39 per shot. The average photon flux was 1.03 photons per pulse on the dot, which gives the quantum efficiency of trapping a single photoelectron in the DQD as 38 %. We compare the trapping rate results with the expected statistics of a Poisson distribution,

$$P(X = k) = \frac{\lambda^k e^{-\lambda}}{k!}, \quad (6.1)$$

where $P(X)$ is the probability of detecting X photons in the DQD, k is the detected photon number and λ is the average trapping probability. When $\lambda = 38$ %, the probabilities are $\{P(0), P(1), P(2), P(3)\} = \{0.68, 0.26, 0.049, 0.006\}$. Compared to the calculation, the measured probability of the two photoelectron trapping is lower than expected. The decrease in efficiency implies that the intrinsic efficiency of two photoelectron excitation is lower and/or anti-bunching effect decreased the rate of trapping of two photoelectrons in a single event. We also compare with the trapping efficiency in a single QD of 15 % obtained in Reference [30]. The efficiency of single photon detection became almost twice for the DQD, indicating that the in-plane area of the dot could contribute on the trapping efficiency.

6.3 Photoelectron trapping in a double heterostructure device

Measurement conditions (B-14155 sample)

The photoelectron trapping measurements were next done in a double heterostructure QW based DQD. The wafer specifics, measurement electronics and

optics setups were explained in Ch. 5. The laser beam alignment and focusing was first tuned at room temperature (see §5.3). The position was later fine tuned onto the dot after cooling down the sample. With an improved design, the DQD was successfully tuned to the (0,0) electron number, with tunable tunneling rates in the kHz to Hz range for each barriers. In this section, the (0,1) and (1,0) excited states were tuned on resonance. The charge states were measured with a sensor on the left side that was preferentially formed as a QD rather than a QPC to improve the signal to noise ratio by increasing the charge sensitivity.

The single photon detection response is only obtained by tuning the excitation laser wavelength and laser pulse power. The wavelength needed for HH excitation was estimated numerically from band calculations ($\lambda = 791$ nm) and experimentally from photoluminescence measurements ($\lambda = 788$ nm). The expected absorption efficiency of the QW was estimated as ~ 1 % using the absorption coefficient $\alpha = 10^4$ cm⁻¹. Single-shot irradiations were first carried out at various excitation wavelengths around the expected wavelength to observe the photoelectron trapping signals.

6.3.1 Single photon detection

Figure 6.6 shows the typical single pulse responses of no photon detection (top) and single photon detection (bottom) around wavelength $\lambda = 785$ nm. In the presented condition, the laser power was considerably high as compared to the previous condition, and obtained a trapping rate of ~ 30 %. Persistent photoconductivity is greatly reduced owing to the better focused laser beam. In the case of no photoelectron trapping in Fig. 6.6, the increase in the sensor current at $t = 0$ is much smaller than those obtained in the previous experiment (Fig. 6.3(a)). Experiments with larger beam widths showed no such reduction, therefore this improvement is nothing to do with any inherent differences between the current and previous wafers. When irradiated outside the metal mask with the focused laser beam, induced photoconductivity varied with sign, amplitude

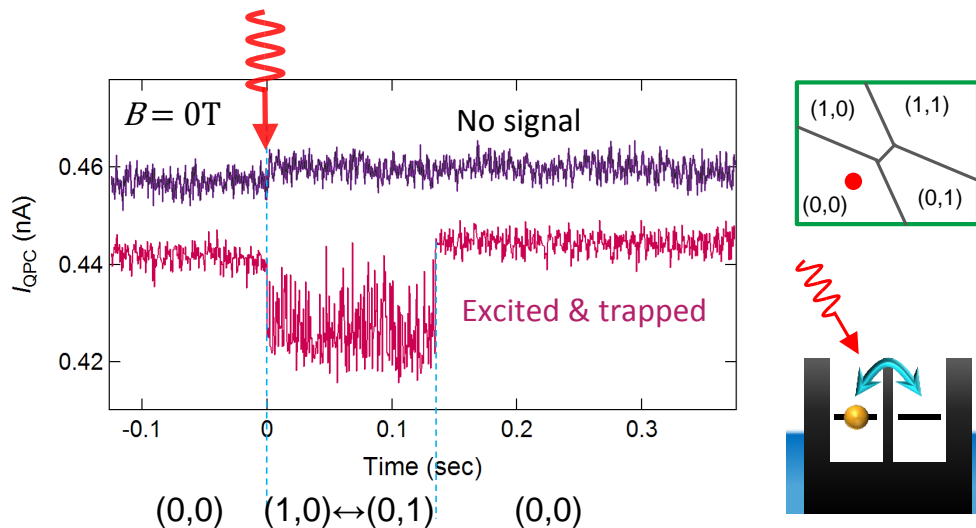


Figure 6.6: Typical photon irradiation signals in a QW based DQD. The initial condition is in the $(0,0)$ electron number Coulomb blockade region. The $(0,1)$ and $(1,0)$ excited states are on resonance. The bottom signal shows single photon detection in a reduced effect of persistent photoconductivity.

and relaxation times depending on the beam position. The physical background behind the different responses are partially explained by various trapping and hopping mechanisms of photo-induced carriers in the deep donor levels (DX centers) spreading over the mesa area [91, 92]. However, external potential induced by the gate voltages makes it difficult to infer the actual response respect to beam position. The beam alignment is completed by measuring the beam position dependence of the single photoelectron trapping efficiency.

The repetitive inter-dot tunneling is not always clearly observed for every photoelectron trapping. The inter-dot detuning can suddenly change upon light pulse irradiation due to a non-uniform charging of the impurity states. The shift usually occurs after a few 100 shots identified by a lack of resonant tunneling. In addition, fast escape of the photoelectron from the DQD can influence the photoelectron trapping signal. We have set the side tunneling rate in the order of Hz but since electron tunneling is a probabilistic process, the escape can

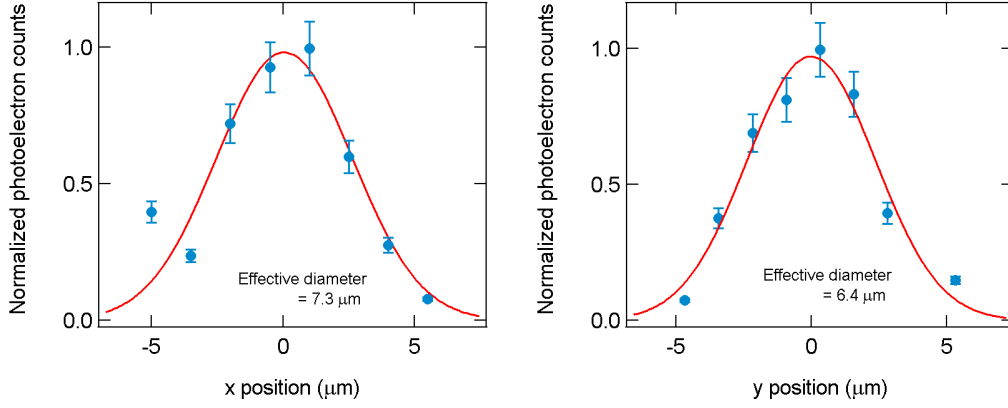


Figure 6.7: Plots of counts of photon detections as a function of laser beam position respect to maximum trapping efficiency position. Counts are normalized to the maximum count rate.

happen faster than the inter-dot tunneling time.

Beam positioning with photon detection

Figure 6.7 is a plot of the measured photon detection rate by taking multiple signals of pulse irradiation signals for different beam positions. The beam position coordinates are calculated from the aspect ratio between the voltage swept on the steering mirror and the actual length scale obtained by laser scanning. Notably, each point is obtained after hundreds of single-shot measurements with an intensity of 200 photons per pulse on the dot. Stable conditions with such an intense power suggest the robustness of this photon detection scheme. From a Gaussian fitting of the plot, the beam diameter ($2\sqrt{2}\sigma$, σ : standard deviation) at the mask position can be derived as $7.3 \mu\text{m}$ and $6.4 \mu\text{m}$ for the x and y directions respectively. The resolution of the beam scanning is roughly 300 nm which is restricted by the resolution of the voltage source. The broad peak could come from the optics, and more improvement may be done if we adjust the sample closer to the focal length of the aspheric lens.

6.3.2 Wavelength selectivity of photon response

The distinctive photoresponse of the double heterostructure compared to the single heterostructure should appear in the spectrum of the photon absorption efficiency. We measured the photon detection rate as we varied the wavelength of the laser. The result is shown in Fig. 6.8. The gray curve represents the initial rough measurement taken for the search of distinct peaks in the spectrum. The statistics were taken from approximately 100 single-shots with the previously mentioned laser condition. The error bars are a standard deviation of a Gaussian distribution estimated solely from the measured counting probability. We see that this approximation does not hold for probability near 0 % where the error bars are unrealistically zero. The result shows a large peak in the trapping rate near 1.58 eV ($\lambda = 785\text{nm}$). Below the energy of this peak, photoelectrons were hardly observed. Whereas at higher energies there were finite trapping rates for which it was hard to resolve a distinct peak in this rough measurement.

The red and blue traces were obtained from a high-resolution measurement around the expected wavelength of HH and LH excitation, which was additionally measured in a ^3He setup with a sample from the same fabrication batch [81]. Comparing with the band calculation for the HH and LH excitation energies (Fig. 6.8(inset)), the photon energy was varied nearby the largest peak and the energy 0.025 eV higher. Results show peaks of the counting probability centered at 1.579 eV ($\lambda = 785.5\text{ nm}$) and 1.602 eV ($\lambda = 774\text{ nm}$) attributed to the HH and LH excitation, respectively. The measured quantum efficiency at the highest peak is of the order of 1 %, which is consistent with our estimation for the absorption rate in a QW. The efficiency of the lower peak is about 1/3 of that of the larger peak, which can also be explained in terms of the absorption rate difference between the HH and LH excitation with the selection rules. Both peaks have a broadening of 2-3 nm in a wavelength scale, which is relatively larger than the typical broadening of the GaAs HH and LH photoluminescence excitation spectrum at low temperature [93,94]. A monolayer fluctuation of the QW layer might be one of the origins of the peak broadening. In addition, volt-

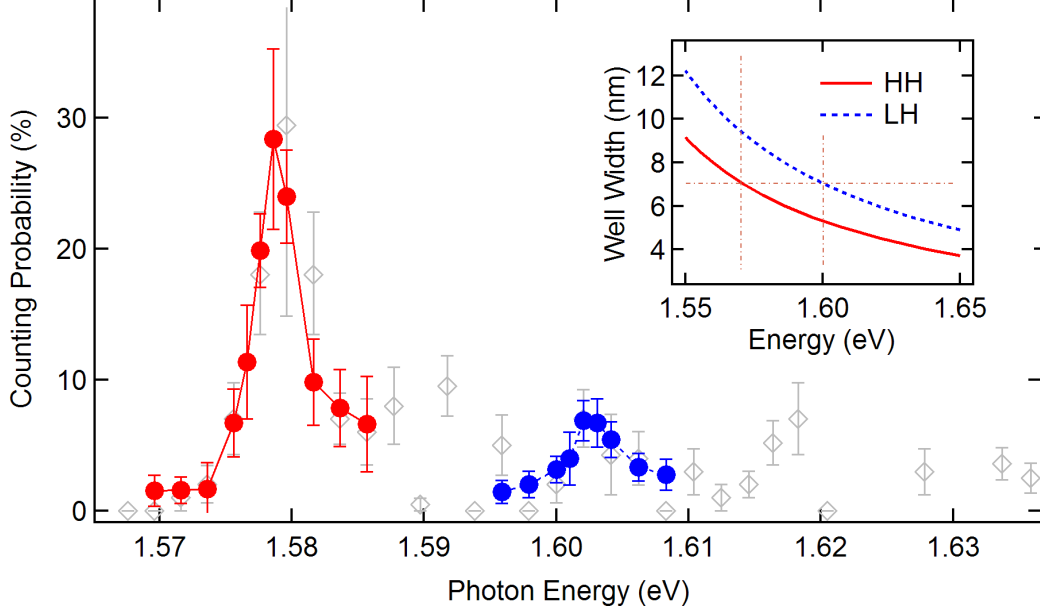


Figure 6.8: Incident photon wavelength dependence of photon detection count rate for several hundred single-shot irradiations. The red trace was taken with 100-200 shots and the blue trace was taken with 200-300 shots. The gray trace was taken with ~ 100 shots for a rough search of peaks.

age applied to the surface metal gates induce a non-uniform electric field near the dot region, which might give a spatial distribution of the excitation energy in the QW [95]. The perpendicular electric field applied to the sample could cause additional peak shift towards higher energy [96], causing the difference from previous photoluminescence measurements [81].

The origin of the finite absorption rate outside the HH, LH excitation peak is still under discussion. Direct excitation of the QD states formed in the QW layer could have just a few % contribution which is significantly smaller than the peaks in Fig. 6.8 [97]. The absorption tail in the higher energy of the peak could be explained by this, but the discrete levels of the QD in the meV order were not resolved in this measurement. The first excited state of the HH could contribute to the absorption above an energy near the LH resonance [94]. An absorption peak could be present at higher energy to the LH excitation,

where the impurity states in the AlGaAs doping layer comes into effect [98]. More detailed measurements with higher spectral resolution and efficiency will be needed to determine the origin of these additional absorptions.

6.3.3 Initial evidence of photoelectron spin detection

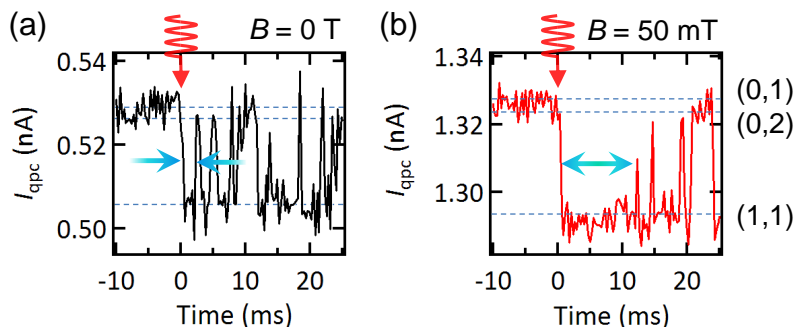


Figure 6.9: Single photoelectron trapping in (0,1) initialized charge state with (1,1) and (0,2) excited states on resonance measured at (a) $B = 0$ T and (b) $B = 50$ mT. Photoelectrons are initially trapped in the left dot and resonantly tunnel into the right dot after $t = 2.3$ ms and $t = 12.0$ ms respectively. The elongated tunneling time at finite magnetic field indicates the observation of electrons with parallel spin excited into the spin blockade configuration.

Finally we briefly show that our scheme for detecting the resonant inter-dot tunneling of photoelectrons provides a fast enough performance to extract its spin information. Figure 6.9 shows the typical single photoelectron trapping signals for a (0,1) initialized charge state with the (1,1) and (0,2) excited states on resonance, where we expect the spin blockade effect to appear at a finite magnetic field. Figure 6.9 shows the measured I_{QPC} at $B = 0$ T in (a) and $B = 50$ mT in (b). The photons were linearly polarized so parallel and anti-parallel spins are created with equal probability. In both measurements a single photoelectron was initially trapped in the left dot seen as a 30 pA downward step at $t = 0$ ms. All data of photoelectron trapping at $B = 0$ T showed instant resonant tunneling as in Fig. 6.9(a) whereas at $B = 50$ mT some data showed that the first inter-dot tunneling appeared at a delayed time such as

$t = 12.0$ ms in Fig. 6.9(b). The elongated inter-dot tunneling time indicates that a parallel spin configuration was instantly established. The lifetime of the blockade here is determined by the hyperfine interaction with nuclear spins in the low magnetic field region, but more details on the spin dependent tunneling will be later discussed in Ch. 7. This result shows that our time scale used to resolve the real-time inter-dot tunneling events is small enough to trace the dynamics of photoelectron spins. This further motivated us to investigate the photoelectron spins created by circularly polarized photons, explained in Ch. 8.

6.4 Conclusions

In this chapter we demonstrated single photon detection in a DQD formed in a double heterostructure QW which is an extension of our previous work in a single dot. A double dot can detect the trapping of a single photoelectron in a non-destructive manner through the resonant inter-dot tunneling of the photoelectron. Multiple photon detection is possible by using this resonance as the indicator of a single excess electron. The characteristics of measuring in a QW was revealed by observing distinct peaks in the spectrum of the photoelectron trapping rate. Each of the peaks were assigned to the HH and LH excitation by comparing with the band energy calculation and the absorption rates from selection rules. Finally, the detection of trapping is completed faster than the typical spin flip rate. This photon detection scheme provides the possibility of trapping electron spins created by selective excitation from the hole states with subsequent manipulation or measurement procedures.

Chapter 7

Spin dependent tunneling in a double quantum dot

In this chapter we discuss the spin dependent tunneling from (1,1) to (0,2) charge states obtained from time resolved measurements for the DQD in Pauli spin blockade. The electron tunneling event is distinguished between the parallel and anti-parallel spin states in a single-shot measurement. Deeper analysis of the spin relaxation mechanisms as demonstrated from observation of two tunneling rates for up and down spin. In this measurement condition, spin measurement is also possible while sitting on a resonance condition of the (1,1) and (0,2) states.

7.1 Pauli spin blockade

Spin blockade in kHz tunneling rates (stability diagram)

Initial confirmation of Pauli spin blockade is performed by taking conventional stability diagrams around the two electron state regions, as explained in §3.2.2. When the over all tunneling rate exceeds GHz, measurements can be done observing the dot current. When the tunneling rate is lowered down to the order of MHz, current through the dot is not visible, but charge sensing signals

are still observed. We used a DQD made in a QW structure (B-14155) to measure the stability diagram in a dilution fridge setup and confirmed the spin blockade in both dot current and charge sensor currents.

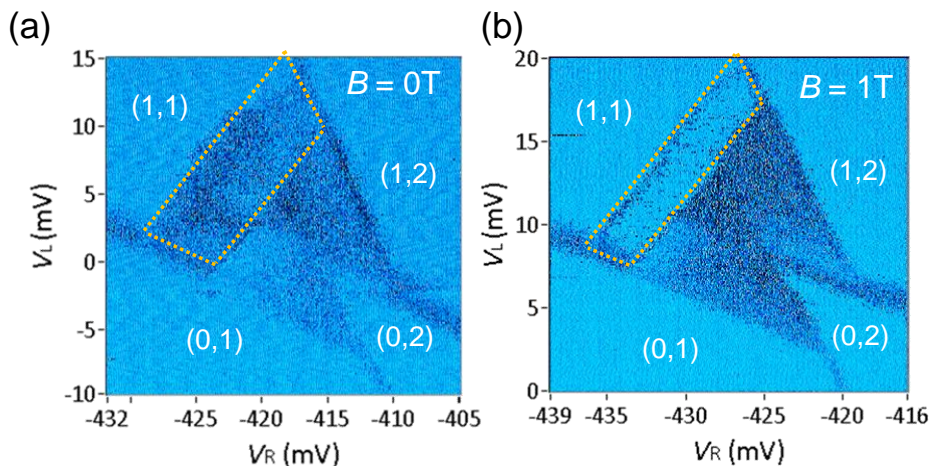


Figure 7.1: (a, b) Charge stability diagrams around (1,1) and (0,2) inter-dot charge transition regions with the inter-dot tunneling rate in the order of kHz. In conditions when tunneling rates are comparable to the sweeping time, electron tunneling appears in the diagram as a large current fluctuation. At $B = 1\text{T}$ tunneling through the ground state (inside trapezoidal region) is suppressed by spin blockade.

When the tunneling times become larger than the order of ms comparable to the voltage sweep rate, single electron tunneling events start to appear in the diagram. Figure 7.1 shows stability diagrams in such a condition. Each of the electron tunneling events are now visible as large fluctuations in the sensor current, seen in the inner region of the bias triangles in Figure 7.1(a). When the magnetic field is turned on, the tunneling signal in the trapezoidal region in orange, indicating the ground state tunneling, is suppressed due to spin blockade 7.1(b). The decreased height of the trapezoid in (b) is due to the decreased energy of the first excited state in a perpendicular magnetic field. The whole region where spin blockade is expected is now visible in the diagram. Difference of the tunneling times between the zero and finite magnetic field can be roughly estimated from the density of fluctuation in the diagram. Here, the

difference is over 10 times, inferring a good distinguishability of the spin states in this region.

To observe spin blockade at a more reduced tunneling time requires time resolved measurements. From hereon the real-time charge sensing is used to detect the electron tunneling events and the single electron tunneling time is obtained by analyzing the change of the charge sensing current.

7.2 Real-time measurement of spin blockade

Here we introduce several regimes of electron tunneling in a DQD observed in a real time manner. Different types of sensor current signals are obtained for two dots out of or on resonance. The most deeply studied condition was in the resonance condition of an unbiased DQD where we observed repetitive transition between parallel and anti-parallel spin states.

Real-time charge sensing in a biased double dot

In order to observe an electron that tunnels through the DQD, we sit inside the region of a bias triangle and continuously measure the sensor current. Figure 7.2 show the typical real-time traces at the given positions in the diagram but now the tunneling times are of the order of 10 ms. Inside the bias triangle, sequential single electron tunneling is observed (Fig. 7.2(a)). The the electron occupation in the left or right dot is well distinguished in the different sensitivity by a factor of 4 to 5. This helps for detection of the inter-dot tunneling which is of our main concern. The inter-dot tunneling is directly observed as the steps indicating transition from the (1,1) to (0,2) state in Fig. 7.2(a). The tunneling observed here can vary with the position inside the triangle as discussed in Reference [99] and this was indeed observed as for example reduction of the inter-dot tunneling rate as a function of detuning energy ε . Depending on the dot level respect to the Fermi level, another electron can tunnel into the left dot from the left side with one already in the right dot. This tunneling condition is sometimes referred to as a ‘hole’ tunneling and could offer an additional photon

detection condition [81]. These tunneling signals are distinguished from the next mentioned on resonance condition.

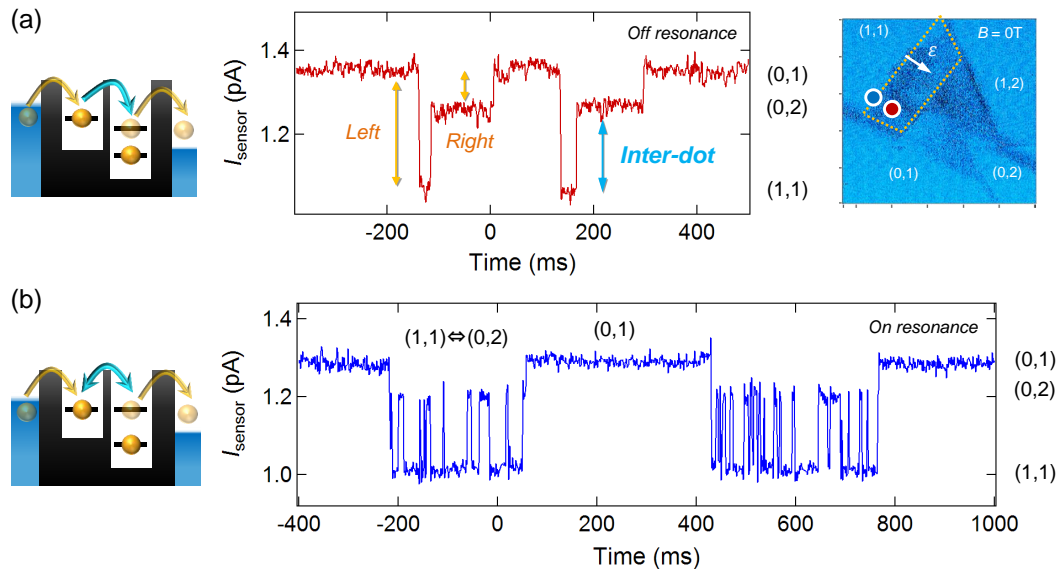


Figure 7.2: (a) Sequential single electron tunneling through the DQD from the left side to the right. (b) Electron tunneling in a resonance condition of (1,1) and (0,2) state. The inter-dot tunneling rate is set faster than the side barriers.

When we trap an additional electron inside the (0,1) DQD, we can repeatedly observe the inter-dot tunneling of the (1,1) and (0,2) states on resonance (Fig. 7.2(b)). Here the side barrier tunneling time is made longer than the inter-dot tunneling time. This resonance tunneling presents a similar signal shown for the single photon detection. Such bidirectional tunneling was previously studied in Reference [100] but with a different electron number.

One technical care that must be taken here is to sufficiently reduce the voltage bias applied to the charge sensor. It is known that nearby charge sensors can induce opposite or enhanced tunneling due to back-action on the dot state through shot-noise energy which is dependent on the sensor bias and conductivity [101, 102]. The effect can be seen in stability diagrams and therefore can influence the tunneling time analysis [103]. The sensor was used under the con-

dition of a bias voltage of 500 μV and a current around 1 nA and then no sign of back-action was observed in the stability diagram.

Real-time measurement of spin blockade in a biased dot

Applying a magnetic field under the above conditions reveals spin related tunneling events. In a finite magnetic field, the triplet states (T_{\pm}) are energetically separated from the singlet state (S) by Zeeman energy $g_e\mu_B B$. The spin effect first appears when this energy exceeds the nuclear spin field fluctuation (B_{nuc}), because the triplet states become decoupled from the $S(0, 2)$ [104]. In our condition, the tunnel coupling is weak, of the order of neV, therefore the $T_0(1, 1)$ and $S(1, 1)$ states are assumed as being hybridized by the inhomogeneous nuclear spin field. As a consequence mainly two configurations are expected to be distinctly resolved: the parallel spin configuration ($\{|T_{\pm}\rangle$ or $\{|\uparrow\uparrow\rangle, |\downarrow\downarrow\rangle\}$) suppressing the inter-dot tunneling and the anti-parallel configuration ($\{|T_0, S\rangle$ or $\{|\uparrow\downarrow\rangle, |\downarrow\uparrow\rangle\}$) not suppressing the inter-dot tunneling.

Figure 7.3(a) shows the typical real-time charge sensor data for the two electron DQD at $B = 1.5$ T with a finite detuning or under the off resonance condition. For the parallel spin configuration of (1,1), the inter-dot tunneling is suppressed and a long residing time is observed as in the red region. The signal afterwards shows that the electron eventually escapes from the DQD through the right dot. The other (1,1) state with residing times are in the anti-parallel spin configuration.

To examine the difference of the tunneling time between the two spin configurations real-time traces on resonance was measured for the biased DQD under the (1,1)-(0,2) resonance condition. We detected signals that are mainly divided into two cases as in Fig. 7.3(b). The first shows resonant inter-dot tunneling as soon an additional electron enters the (0,1) dot, which is similar to the zero field signals in Fig. 7.2. No blocked region is observed so this signal can be interpreted as a creation of anti-parallel spin state that is preserved while a number of inter-dot tunnelings occur before the electron escapes from the DQD. The other shows a long stable current at the (1,1) state before an electron starts

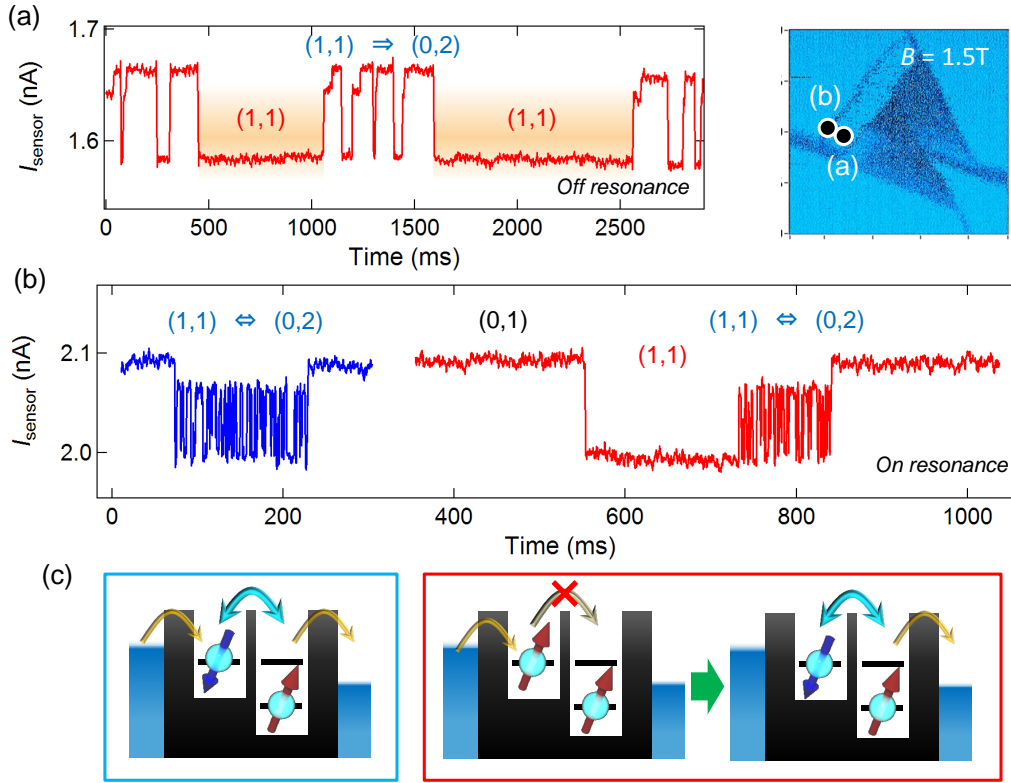


Figure 7.3: (a) Typical real-time signals representing anti-parallel and parallel spin configuration in a biased condition. (b) A real-time trace in the resonance condition. The left trace is a resonance tunneling similar to that in zero magnetic field whereas the right curve has a stable region at $(1,1)$ state. (c) Schematics of the electron dynamics respect to spin configurations corresponding to the colored traces.

to tunnel resonantly between the two dots. This signal represents a formation of the parallel spin state in $(1,1)$ state that subsequently transits to the anti-parallel configuration. Figure 7.3(c) illustrates these situations schematically.

Under the biased condition we can clearly observe that the two spin configurations are created upon two electron spin state formation. Such a situation of adding an electron from the reservoir is analogous to adding a photoelectron, thus presenting us an expectation that we would obtain for a photoelectron spin measurement. The technique using resonant transitions for spin detection was originally proposed for optical measurement of spin states in atomic sys-

tems [105, 106]. This was eventually utilized for optical spin detection in self assembled quantum dots aiming for all optical single-shot measurements towards quantum computing [80, 107]. Unlike optical measurements, where high photon collection efficiency is needed, electrical spin measurements have enabled a high fidelity read-out in a single dot [71]. However, as discussed in Ch. 6, the lateral dot is not completely stable to photon irradiation to perform this precise measurement because electrons can eventually tunnel out to the leads. Therefore we introduce this spin detection in a resonant condition to obtain higher distinguishability of the single-shot photoelectron spin measurements. This way of measurement has never been performed for electrically gated double dots.

7.3 Analysis of real-time spin blockade

The tunneling rate in GaAs based lateral DQDs has been theoretically studied including the spin relaxation mechanisms [108] but they were not in the range of tunneling rates that we discuss here. We analyzed our real-time data by comparing several theoretical and experimental results and found some robust dependences on the applied magnetic field which are governed by nuclear field fluctuation. Over the ranges where hyperfine interaction dominates, the transition rate between the two spin configurations is largely different. We observe that the condition holds for a wide range of magnetic field which indicates the feasibility of our spin detection technique for single photogenerated electrons.

7.3.1 Evaluation of spin dependent tunneling times

Spin blockade in an unbiased condition

When the side tunneling barriers between the leads and dots are thick enough or when no bias is applied on the dot, an electron can be trapped in the DQD on resonance for a sufficiently long time to observe the spin dynamics in real-time. Figure 7.4(a) shows such an example for repeated inter-dot tunneling measured at zero bias for $\tau_C = 1.34$ ms and $B = 80$ mT. Two distinct regions,

the repetitive inter-dot tunneling region and the stable region, are observed. Figure 7.4(b) shows spin blockade for a different condition, $\tau_C = 15$ ms and $B = 1.5$ T. We observe that the blocked time increases by an order of magnitude and the counts of inter-dot tunneling events under resonance also increases. The difference of these two conditions implies that the time of transition between the two spin configurations (depicted in Fig. 7.4(c)) may depend on the inter-dot tunneling time as well as magnetic field. We will analyze and discuss the real-time signals to reveal the dominant source of the changes in the spin transition times.

Tunneling time evaluation

The characteristic tunneling times were extracted from the real-time traces by first taking a histogram of the tunneling times. We directly measured the tunneling times in the time domain by an appropriate thresholding on the sensor current, I_{sensor} [109]. We plot histograms of the (1,1) state residing time to unveil the different time constants. Figure 7.5 shows examples of the histograms at a zero magnetic field (a) and a finite magnetic field of $B = 80$ mT (b). A single exponential histogram is observed for the $B = 0$ case showing that the tunneling is governed by a single time constant. This is expected from the fact that the two different spin states are hybridized. On the other hand in (b), the hybridization of spins is lifted due to the magnetic field and two time constants with a fast one (τ_f) and a slow one (τ_s) appear as represented by the biexponential histogram (Fig. 7.5(b)). We extract the τ_f representing the anti-parallel spin tunneling and the τ_s representing the parallel spin lifetime.

The most sharp feature that we noticed in the time constants, when varying several conditions, is that even though τ_f and τ_s easily varied respect to the inter-dot tunneling time τ_C , the ratio of those two constants τ_s/τ_f did not easily vary. This implies that instead of observing solely the relaxation time of a two electron spin flipping, as we can measure the single spin relaxation time in single dots, we can observe a transition time that can range below ms to over 100 ms that implicitly includes the effect of the inter-dot coupling. We will

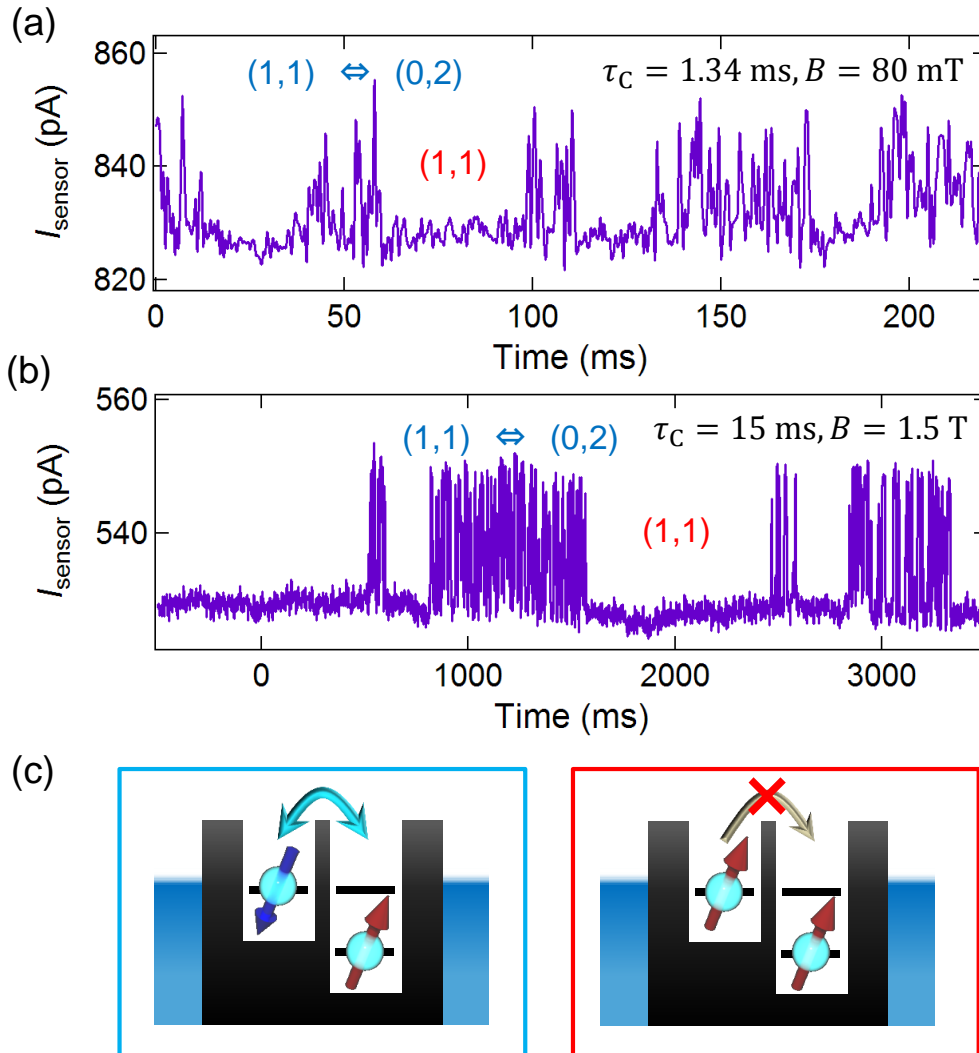


Figure 7.4: (a) Real-time measurement of resonant inter-dot tunneling in $B = 80$ mT. Two distinct regions with a repetitive inter-dot tunneling and a suppressed tunneling repeatedly appears in a single trace. (b) Resonant inter-dot tunneling tuned to conditions with longer tunneling times using inter-dot tunneling rate and magnetic field. (c) Schematics of spin states in (blue) an anti-parallel and (red) a parallel configuration expected in each corresponding regions. The two spin configurations exchange by an abrupt spin-flip.

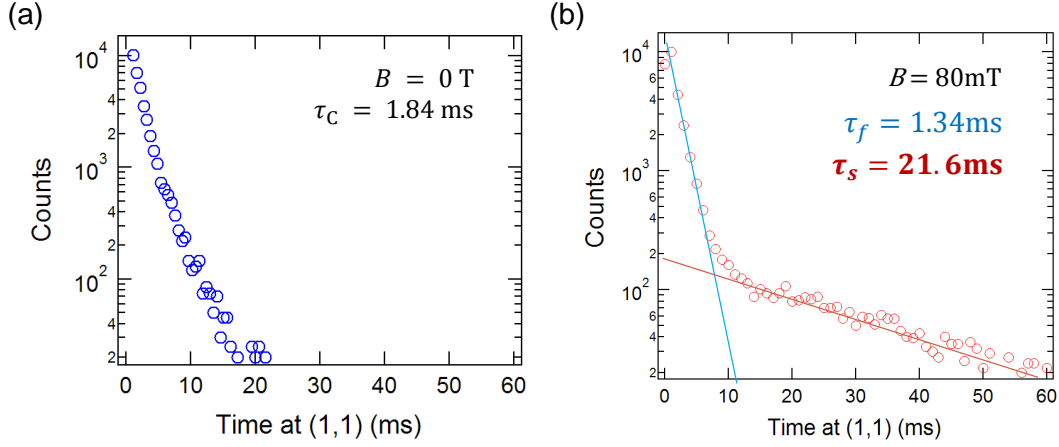


Figure 7.5: (a) Histogram of the residing time in (1,1) state at zero magnetic field. (b) Histogram at finite magnetic field. Distinct slopes with two different tunneling rates appear.

more deeply examine the dependence of the measured ratio τ_s/τ_f in the next part.

Magnetic field dependence of tunneling time constant ratio

Figure 7.6 plots the magnetic field dependence of τ_s/τ_f . The plot of $B < 100$ mT shows a clear dependence on B . For example the two data points at 40 mT have a similar value of $\tau_s/\tau_f = 21.9$ ms/4.7 ms = 4.6 and $\tau_s/\tau_f = 148$ ms/29.3 ms = 5.1 but τ_C is differed by an order of magnitude. The plots above 100 mT deviate from the low magnetic field region and saturated at certain values depending on the dot conditions (red, orange and blue points in Fig. 7.6). The different conditions are realized when the voltages of gate TL and TR (see Fig. 5.5) are tuned relatively different. The maximum ratio of τ_s/τ_f obtained is 132 (= 656 ms/5.0 ms) at $B = 1.9$ T. For a more higher magnetic field, the first excited state starts to overlap with the ground state, due to the wavefunction shrinking in a perpendicular magnetic field. Parallel spins are no longer blocked in this case, so both spin configurations show similar tunneling times, making $\tau_s/\tau_f \sim 1$.

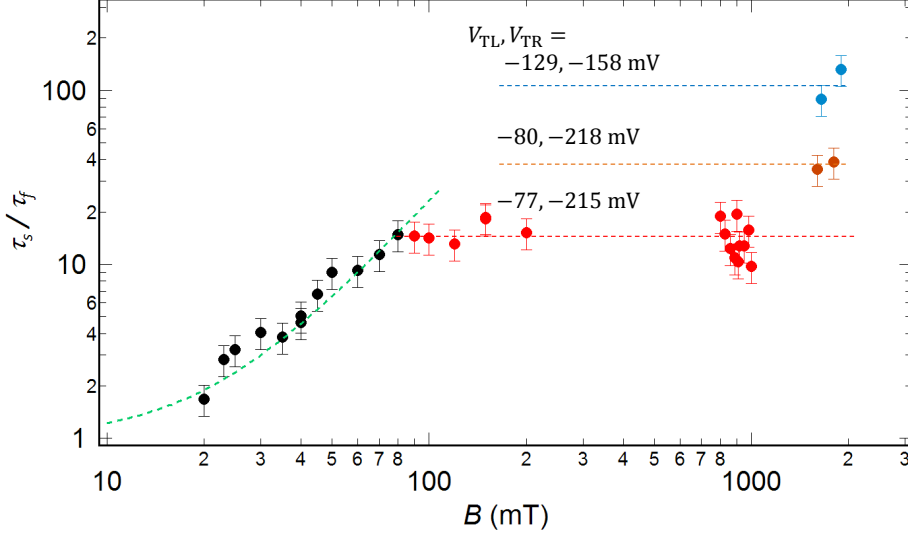


Figure 7.6: Tunneling time ratio plotted as a function of magnetic field. Fast and slow tunneling rates are derived from the biexponential histogram. The plot under $B = 100$ mT is fitted with Eq. 7.1 giving $B_{nuc} = 25$ mT. Over 100 mT the different colored symbols show measurement at different dot conditions. Gate voltages are shown for the possible effect to the dot asymmetry.

We compare the region $B < 100$ mT with theoretically deduced equations for a hyperfine-driven decay reported in the supplementary of Reference [110]. The corresponding tunneling rates of the parallel and anti-parallel spin configurations are given by, $\Gamma_{\pm\frac{1}{2},\pm\frac{1}{2}} = \frac{\Gamma_{in}}{4} \frac{B_{nuc}^2}{B_{nuc}^2 + B^2}$ and $\Gamma_{\pm\frac{1}{2},\mp\frac{1}{2}} = \frac{\Gamma_{in}}{2} \left[1 - \frac{B_{nuc}^2}{2(B_{nuc}^2 + B^2)} \right]$, where $\Gamma_{\pm\frac{1}{2},\pm\frac{1}{2}}$, $\Gamma_{\pm\frac{1}{2},\mp\frac{1}{2}}$ and Γ_{in} are the spin flipped, spin preserved and bare inter-dot tunneling rates, respectively. B_{nuc} is the root-mean-square magnitude of an effective magnetic field due to the randomly fluctuating nuclei. The calculation of $\Gamma_{\pm\frac{1}{2},\pm\frac{1}{2}}$ and $\Gamma_{\pm\frac{1}{2},\mp\frac{1}{2}}$ being proportional to Γ_{in} supports our observation of the variation of blockade lifetimes. We can apply these decay rates to our result by $\Gamma_{\pm\frac{1}{2},\pm\frac{1}{2}} = 1/\tau_s$ and $\Gamma_{\pm\frac{1}{2},\mp\frac{1}{2}} = 1/\tau_f$, and calculate the ratio τ_s/τ_f as,

$$\frac{\tau_s}{\tau_f} = 1 + 2 \frac{B^2}{B_{nuc}^2}, \quad (7.1)$$

showing no dependence on inter-dot tunneling time. Our data is fitted by this equation (dashed curve in Fig. 7.6) with $B_{nuc} = 25$ mT as the only fitting parameter.

In Reference [110] the parameter B_{nuc} used for the GaAs QD is $B_{nuc} = 18\text{mT} \sqrt{\frac{\hbar\omega[\text{meV}]}{l[\text{nm}]}}$ where $\hbar\omega$ is the single particle level spacing and l is the thickness of the wavefunction. The coefficient is inversely proportional to the g -factor by definition (the formula used $|g_{\text{GaAs}}| = 0.44$). Inserting our estimation of $\hbar\omega = 1$ meV, $l = 7.3$ nm and $B_{nuc} = 25$ mT, we can expect our g -factor to be $g_e = 0.12$. This value is consistent with the value of 0.12 obtained from the ESR measurement performed on a 2DEG in the same configuration of perpendicular magnetic field. Our result still has an ambiguity in $\hbar\omega$ due to the asymmetry of the dot. If more evidence can be collected to confirm the correspondence, this analysis of spin dependent tunneling time could offer a novel way to determine the QD g -factor.

There are still no measurements above the magnetic fields where hyperfine-driven decay dominates. Therefore we show a possible formula for τ_s/τ_f due to the contribution of spin-orbit interaction [111]. When we assume that the charge noise or phonon drives the two electron spin states via spin-orbit interaction, the transition of $T_{\pm}(1, 1) \leftrightarrow S(0, 2)$ can occur because the effective spin-orbit magnetic field is perpendicular to the external magnetic field. We compare the calculated transition rate with the bare tunneling of $S(1, 1) \leftrightarrow S(0, 2)$ and we get the following formula,

$$\frac{\tau_s}{\tau_f} = \left(\frac{l_{SO}}{d} \right)^2, \quad (7.2)$$

where l_{SO} is the spin orbit length and $2d$ is the separation between the two dots. This equation gives a constant value independent of the magnetic field that could explain the saturation we observed in Fig. 7.6. l_{SO} is in the order of a few μm [112] and d could be in the order of a few 100 nm. We see that the obtained τ_s/τ_f is in the expected order varying from a few tens to hundreds. Different tunneling rates can give a different d and in addition the shape of the dot with

respect to the crystallographic direction can give a different l_{SO} [113]. This could account for the different mean values of data points shown with different color plots in Fig. 7.6, but a more systematic study of the used parameters is needed to reach a clear conclusion for the validity of this equation.

Additionally, measurement at higher magnetic field is desired to investigate how far our assumptions hold. Measurement in an in-plane magnetic field could realize higher magnetic field, since the excited states would not affect the ground state tunneling.

7.3.2 Distinguishability of electron spins

Here we show that the spin dependent tunneling rate ratios are tuned by a factor of 2, resulting in a high distinguishability of the spin state measurement. The accuracy of our spin detection scheme is evaluated in terms of ‘distinguishability’. Distinguishability is the lower bound of the visibility of the measurement. This can be calculated from the fast and slow time constants when assuming an equal probability of the measured spin states. We set this assumption here because we lack the initialization process needed to evaluate the ‘visibility’ (termed in Ref. [71]).

The spin states are determined in a single-shot by setting a threshold time τ_{th} on the first tunneling time t . If $t < \tau_{th}$ the state is determined as an anti-parallel spin configuration and if $t > \tau_{th}$ the state is determined as a parallel configuration. Due to the exponential behavior of tunneling time, the statistics of the measurement would give unavoidable errors. From the time constants τ_f and τ_s measured in advance we calculate the best thresholding time to minimize the error probability α (probability of measuring ‘slow’ though it was originally ‘fast’) + β (probability of measuring ‘fast’ though it was originally ‘slow’). To minimize $\alpha + \beta$, the thresholding time t_{th} is set at,

$$t_{th} = \frac{\tau_s \tau_f}{\tau_s - \tau_f} \ln \left(\frac{\tau_s}{\tau_f} \right) \quad (7.3)$$

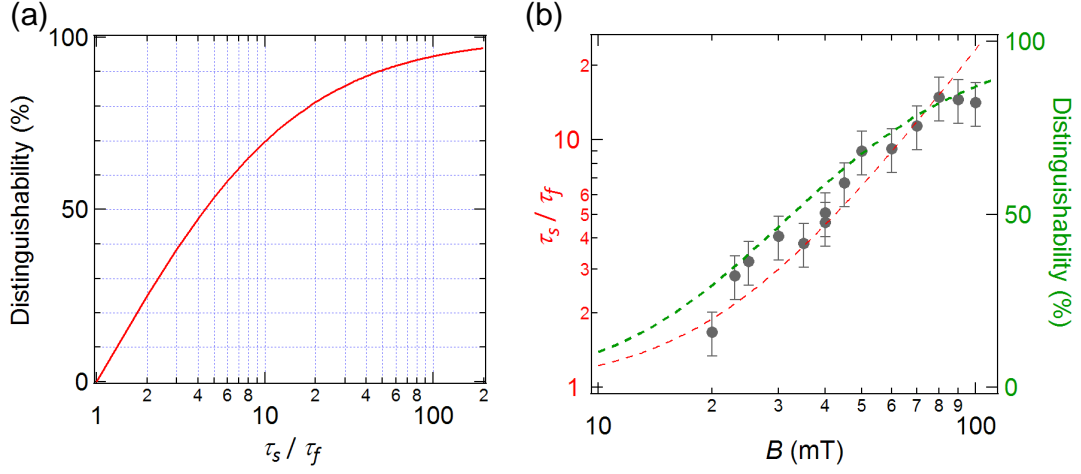


Figure 7.7: (a) Distinguishability as a function of τ_s/τ_f . (b) Distinguishability calculated from the fitted hyperfine mediated region. Plots are taken from the lower magnetic field region of Fig. 7.6.

in an equal spin injection assumption. This t_{th} is inserted to the error rates, and then the distinguishability ($D(\tau_s/\tau_f) \equiv 1 - \alpha - \beta$) is calculated as,

$$D(\tau_s/\tau_f) = r^{-1/(r-1)} - r^{-r/(r-1)} : \left(r = \frac{\tau_s}{\tau_f} \right). \quad (7.4)$$

The result is plotted in Fig. 7.7(a). The distinguishability starts from $D(1) = 0$ % at $\tau_s/\tau_f = 1$ and increases with τ_s/τ_f exceeding 90 % for $\tau_s/\tau_f > 50$. The best realized condition was $\tau_s/\tau_f = 132$, $D(132) = 96$ %. Figure 7.7(b) shows the distinguishability calculated from the fitted τ_s/τ_f function to the plots in the low magnetic field region. The obtained distinguishabilities are less than 80 % in the hyperfine dominating region.

7.4 Conclusions

In this chapter we observed the spin blockade in a real-time manner through the inter-dot tunneling from the (1,1) to (0,2) state in a DQD formed in a QW. A short and a long tunneling time constant was obtained from the double

exponential histogram, and attributed to the anti-parallel spin tunneling time and the parallel spin tunneling time. One characteristic of the blocked tunneling time is that it can be tuned with the inter-dot tunneling time so that it becomes longer than the measurement bandwidth. By taking the ratio of the long and short tunneling times we could reveal the underlying spin flip mechanisms such as hyperfine mediated tunneling. Under the higher magnetic field conditions the certainty of spin detection is tunable to some extent. The accuracy of spin detection was discussed in terms of distinguishability. At the best condition, the distinguishability became 96 %. Especially in a resonance condition it is possible to implement the analogy of quantum jump technique to detect the difference of two electron spin configurations, parallel and anti-parallel, with high visibility in a real-time manner [80, 107]. The resonance condition is indeed a compatible condition with the high resolution photoelectron detection scheme discussed in Ch. 6. Combining these schemes would realize photoelectron trapping and subsequent spin detection.

Chapter 8

Transfer of single photon polarization to single electron spin

We show in Ch. 6 that the single photoelectrons were detected in a non-destructive manner and in Ch. 7 that the electron spin configurations are measured by observing the spin blockade in a real-time manner. Combining these techniques, we can measure a single photoelectron spin if we can initialize an electron spin in the $(0,1)$ state as a reference spin. Furthermore, HH excitation can create polarized spins following the selection rules. Therefore, detecting the single photoelectron spin created from a circular polarized photon will provide the verification of angular momentum transfer between single quanta i.e. single photons and single electrons. This is an indispensable step towards coherent transfer from single photon polarizations to single electron spins.

8.1 Single photoelectron spin detection

Preparation

The measured sample and measurement condition are the same as written in the previous chapter. Here the DQD is tuned around the (1,1) and (0,2) inter-dot transition region (Fig. 8.1(a)). The photon irradiation measurements are mainly done at the triangle point of (0,1) state (\blacktriangle in Fig. 8.1(a)). At the square point of (1,1)-(0,2) state (\blacksquare in Fig. 8.1(a)) single photon detection with

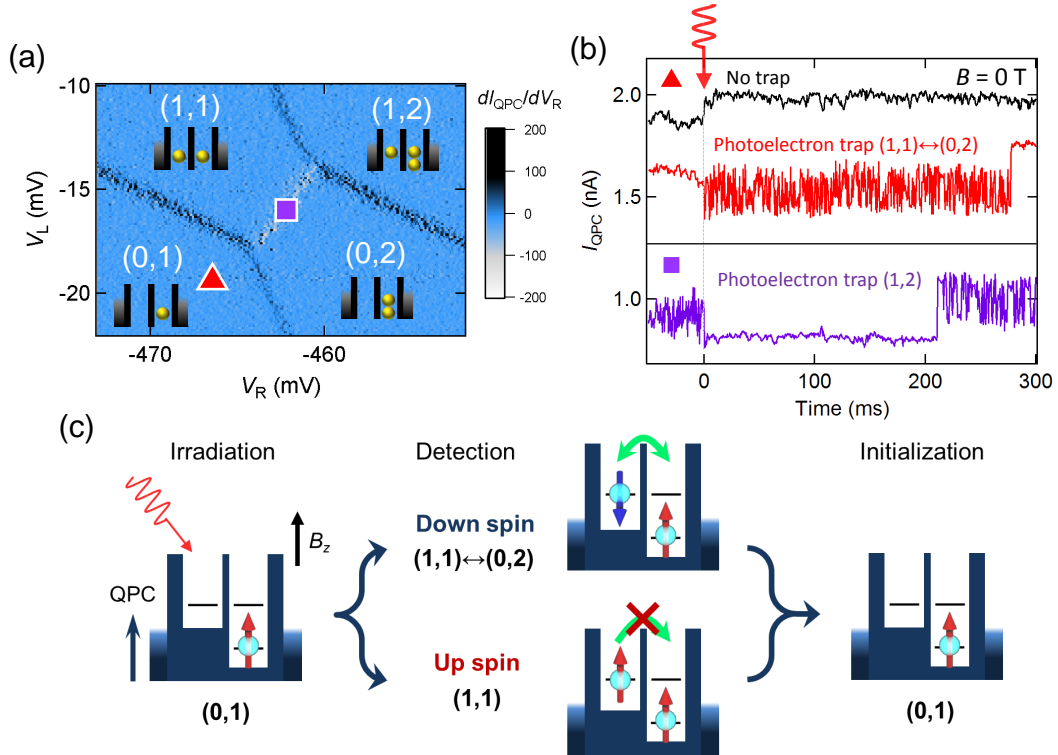


Figure 8.1: (a) A stability diagram around the (1,1) and (0,2) inter-dot charge transition line. The position on the white diagonal line corresponds to (1,1) and (0,2) states on resonance. (b) Typical photoelectron trapping signals at zero magnetic field. Gate voltages are initialized on \blacktriangle and \blacksquare in figure (a). Initialization at \blacktriangle gives the same signal as the (0,0) initialized condition. The signal initialized at \blacksquare shows (1,2) state subsequent to irradiation which is distinguished from spin blockade signals. (c) The procedure to detect a single photoelectron utilizing real-time spin blockade.

an additional electron is performed for comparison. Figure 8.1(b) shows the typical pulse irradiation responses of I_{QPC} at $B = 0$ T, similar to those shown in Ch. 6. Single photon detection at the square point is shown in the bottom figure. The I_{QPC} starts with a stable current slightly lower than that due to the subsequent resonance tunneling.

The scheme of detecting a single photoelectron spin at the triangle point in Fig. 8.1(a) is as follows (Fig. 8.1(c)):

- (i) Initialization: The DQD is initialized at the (0,1) state with the (1,1) and (0,2) photogenerated states on resonance. The prepared spin will point towards the applied perpendicular magnetic field.
- (ii) Irradiation and trapping: A single laser pulse is irradiated and photoelectron trapping is detected by the real-time charge sensor signal.
- (iii) Spin detection: Observation repeated resonant tunneling in I_{QPC} is an indication of down-spin trapping, whereas that of a no fluctuation in I_{QPC} is an indication of up-spin trapping.

The dot will be initialized again by the tunneling of the excess electron to the leads in a sufficiently long waiting.

In Ch. 7 we show that at higher fields the distinguishability of spins can be tuned by changing the gate voltages. We apply the distinguishability for the photoelectron spin measurement here. Single photoelectrons are generated by the HH excitation with incident photon wavelength of $\lambda = 785$ nm and a laser intensity giving one photoelectron trapping per ~ 20 shots.

Photoelectron spin detection

Figure 8.2 shows the typical single photoelectron spin detection signals in I_{QPC} obtained from the condition explained above. Figure 8.2(a) is the detection of a down-spin photoelectron. The resonant tunneling is observed immediately after irradiation, inferring an anti-parallel spin configuration created between the photoelectron spin and the prepared up-spin. The I_{QPC} signal becomes

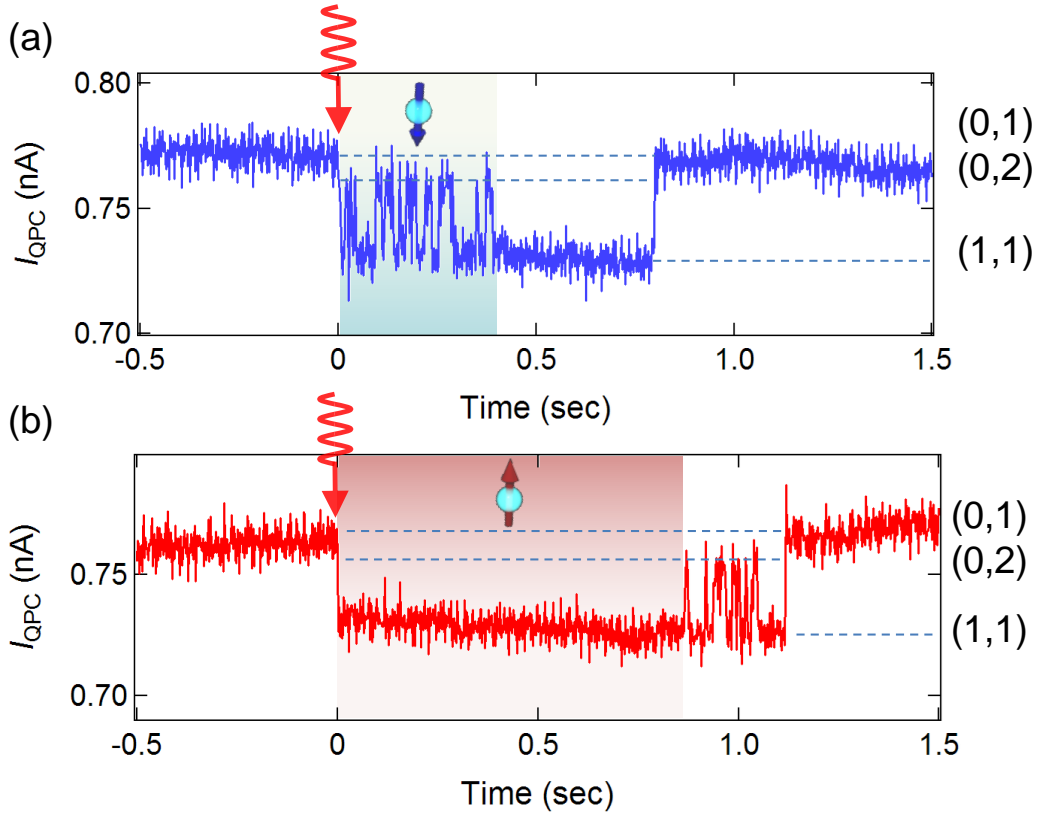


Figure 8.2: Typical real-time traces of single photoelectron spin detection signals measured at $B = 1.65$ T. (a) Resonant tunneling signal is immediately observed after irradiation indicating a down spin detection of the photoelectron. (b) The other type of spin signal with a stable current observed at (1,1) state subsequent to irradiation indicating an up spin detection of the photoelectron. Both spin configurations eventually flipped to the other spin configuration and reinitialized by a single electron escaping from the DQD.

stable at the (1,1) state when the configuration transits to the parallel spin configuration, that would be spin-blocked. An electron finally escapes from the left dot, and then the (0,1) state is recovered. Figure 8.2(b) shows the up-spin photoelectron detection which a stable I_{QPC} at the (1,1) state subsequent to the photon irradiation. The first blocked signal of I_{QPC} indicates formation of the parallel spin configuration of the photoelectron spin and the prepared spin. This parallel spin configuration can also transit to the anti-parallel configuration

after τ_s . In either case we observe the transition of the spin configuration in a sufficiently long time indicating the robustness of the detection of photoelectron spins.

8.2 Angular momentum transfer between single quanta

Verification of angular momentum transfer

We irradiated over 1000 shots of laser pulses for each polarization and magnetic field. The achieved photon trapping rate was ~ 50 out of 1000 shots. We analyzed the statistics of the single photon detection signals, expecting a weighting in the detected number of spins if one of the spin states is created preferentially by the photon polarization. All the other signals for no trapping, two photon trapping, and so on are excluded from the counts.

Figure 8.3 shows the photon polarization dependence of the blocked I_{QPC} signal rate. The polarization is varied from left circular polarization $|\sigma^- \rangle$ to the right circular polarization $|\sigma^+ \rangle$ via horizontal polarization $|H \rangle$ by rotating the $\lambda/4$ plate angle θ from $-\pi/4$ to $\pi/4$. The error bars are the standard deviation of the counted spin measurements. The two different color plots are taken for the opposite magnetic field directions. For example, for the positive magnetic field the blocked probability is the maximum (minimum) for the $|\sigma^- \rangle$ ($|\sigma^+ \rangle$) excitation. This indicates the up-spin creation by the $|\sigma^- \rangle$ irradiation and the down-spin creation by the $|\sigma^+ \rangle$ irradiation. The two plots obtained for the opposite magnetic field directions are independently fitted using the expected sine functions of Eq. 8.6 discussed in the next part. The good fitting to both plots indicate the successful measurement of the photoelectron spins.

Expected spin polarization

The laser source is linearly polarized in the plane of the optics table ($|H \rangle$). We rotated a $\lambda/4$ plate to change the incident photon polarization from the

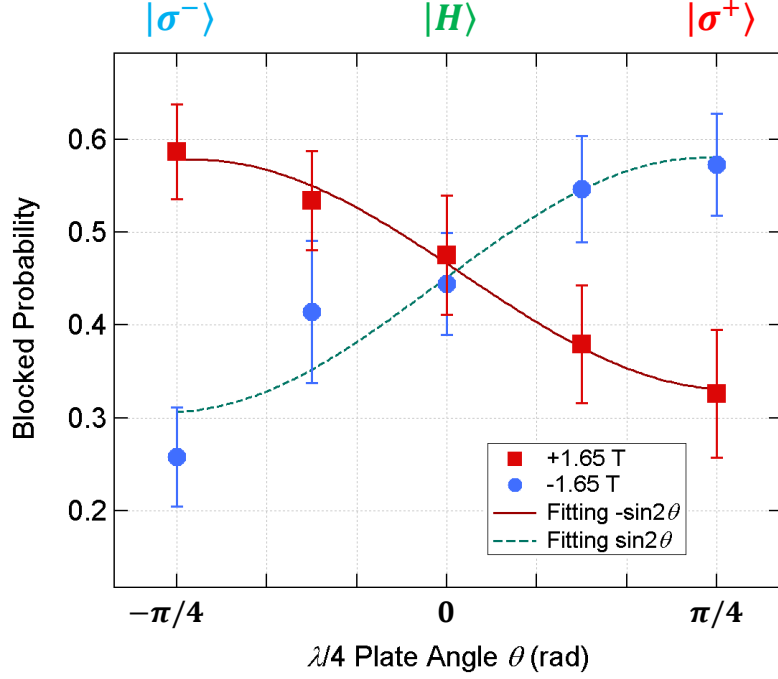


Figure 8.3: Polarization dependence of parallel spin detection probability. Red and blue dots show results for positive and negative magnetic field where the detected spins would be opposite due to opposite prepared spins. Points are fitted to a sine function.

left circular polarization ($|\sigma^- \rangle$) to the right circular polarization ($|\sigma^+ \rangle$) in the experiment of photon-electron angular momentum transfer. We will discuss the intermediate polarizations and the expected spin signals by expressing the polarization of light, propagating in the z direction, in a Jones vector,

$$|H\rangle = \begin{pmatrix} 1 \\ 0 \end{pmatrix}, |V\rangle = \begin{pmatrix} 0 \\ 1 \end{pmatrix}, |\sigma^+\rangle = \frac{1}{\sqrt{2}} \begin{pmatrix} 1 \\ -i \end{pmatrix}, |\sigma^-\rangle = \frac{1}{\sqrt{2}} \begin{pmatrix} 1 \\ +i \end{pmatrix}. \quad (8.1)$$

The Jones matrix $M(\theta)$ for rotating the fast axis of the $\lambda/4$ plate from the $|H\rangle$ direction by an angle θ is expressed as,

$$M(\theta) = R(\theta)MR(-\theta) \quad (8.2)$$

$$= \begin{pmatrix} \cos \theta & -\sin \theta \\ \sin \theta & \cos \theta \end{pmatrix} \begin{pmatrix} 1 & 0 \\ 0 & i \end{pmatrix} \begin{pmatrix} \cos \theta & \sin \theta \\ -\sin \theta & \cos \theta \end{pmatrix} \quad (8.3)$$

where M is the matrix of the $\lambda/4$ plate with the fast axis in the $|H\rangle$ direction and $R(\theta)$ is the rotation matrix. The resulting polarization is thus,

$$M(\theta)|H\rangle = \begin{pmatrix} \cos^2 \theta + i \sin^2 \theta \\ (1 - i) \cos \theta \sin \theta \end{pmatrix} \quad (8.4)$$

$$= e^{i\theta} \sqrt{\frac{1 + \sin 2\theta}{2}} |\sigma^+\rangle + e^{-i\theta} \sqrt{\frac{1 - \sin 2\theta}{2}} |\sigma^-\rangle. \quad (8.5)$$

The probability of detecting $|\sigma^\pm\rangle$ is represented by the square of the respective coefficients in Eq. 8.5. The selection rules of the HH excitations are, $|\sigma^+\rangle \rightarrow |\downarrow\rangle$ and $|\sigma^-\rangle \rightarrow |\uparrow\rangle$. Therefore, the expected probability of detecting the up- or down-spin for the HH excitation is,

$$\frac{1 - \sin 2\theta}{2} \text{ for } |\uparrow\rangle \text{ and } \frac{1 + \sin 2\theta}{2} \text{ for } |\downarrow\rangle, \quad (8.6)$$

respectively.

8.3 Discussions on single photon polarization detection

The total fidelity of spin detection obtained in Fig. 8.3 is about 60% for the circular polarized irradiation. The possible sources of the deviation from an ideal curve could be (i) statistical errors, (ii) degradation of photon polarization and (iii) insufficient initialization of the reference electron spin. Here, the resulting fidelity below unity and the slight shift of the spin detection rates from 0.5 are

discussed.

An un-avoidable error comes from the statistical property of the tunneling times. The tunneling time constants measured in advance was $\tau_f = 20$ ms and $\tau_s = 500$ ms. The calculation of distinguishability gives 92 % and a threshold of 67 ms. A spin detection fidelity of 96 % is expected in this condition if the electron spins are perfectly injected by the circularly polarized photons. This is the maximum amplitude of the curve that we expect and other contribution of errors will further degrade the signal. As explained in §6.3, the escape of photoelectrons to the reservoir and sudden dot potential shift can additionally affect the statistics. The procedure of excluding photoelectron trapping data during the restoration of the DQD condition can be a reason for the vertical shift from 0.5.

The silver coated steering mirror placed after the wavelength plate can distort the polarization by a few % in the used wavelength range. Additionally, photon polarization can be distorted through the 400 nm diameter aperture of the metal mask and onto the sample structure with the fine gate patterns. We simulated the light propagation using a FDTD method and derived the polarization distortion of about 1 %, which is negligibly small.

On the other hand a larger influence on the spin detection fidelity can arise from the temperature. While waiting for the initialization longer than the spin relaxation time, the reference electron spin would distribute between the two spin states in a Boltzmann distribution [114]. We calculate the error rate of having the reference electron in the Zeeman split excited state by,

$$error = \frac{\exp\left(-\frac{g_e \mu_B B}{k_B T}\right)}{1 + \exp\left(-\frac{g_e \mu_B B}{k_B T}\right)}. \quad (8.7)$$

The expected blocked probability as a function of incident photon polarization is plotted in Fig. 8.4. The parameters of $g_e = 0.12$ and $T = 130$ mK in Eq. 8.7 are used to compare with the experimental data at $B = 1.65$ T. The estimate of the effective electron temperature in the dot T here is an upper bound. If we include

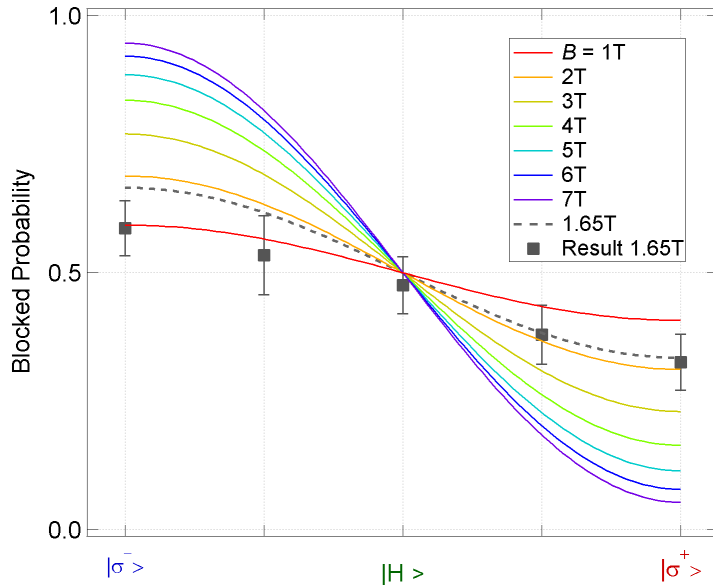


Figure 8.4: Calculation of the expected polarization dependence of the blocked probability of photoelectron spin detection. The probability is calculated from the error rate from the Boltzmann distribution. The distinguishability in our condition, $g_e = 0.12$ and $T = 130$ mK is included in the calculation.

the factors that contribute to the degradation other than thermal effect, the estimate of T will decrease but a more systematic investigation is required. In this figure we see that the blocked probability or spin distinguishability increases as the magnetic field increases simply because the Zeeman energy increases to decrease the error in Eq. 8.7. However, the out of plane magnetic field in our setup restricts the maximum field of observing spin blockade (Ch. 7). If we use an in-plane magnetic field, which is also appropriate for the coherent transfer scheme, the magnetic field could be further increased exceeding $B = 1.65$ T. Then the spin detection probability $> 90\%$ can be obtained at $B = 7$ T.

8.4 Conclusions

In this chapter, we combined the photoelectron detection technique mentioned in the previous chapters and the photoelectron spin readout technique in a single-shot manner. The DQD, formed in a near zero electron g -factor QW, was tuned to the (1,1)-(0,2) transition point when photoelectron is newly trapped by the DQD. Then spin blockade, or repeated inter-dot tunneling occurs depending on which of the two-electron spin configurations, parallel or anti-parallel is established by the photon trapping. By tuning the incident laser wavelength to the HH excitation, we successfully trapped a single photoelectron in the DQD and measured its spin state in terms of the instant inter-dot tunneling signal upon photon irradiation. Large distinguishability between the parallel and anti-parallel spin configurations made possible the accurate determination of photoelectron spin orientation, up or down. We finally confirmed the detection of single angular momentum transfer from circularly polarized photons to electron spins by the polarization dependence of the statistically derived electron spin states. We found the fidelity of photon polarization to electron spin conversion is limited by the thermal effect on the reference spin. This can be greatly improved by using an in-plane magnetic field instead of an out of plane magnetic field used here. It can open a way towards the manipulation of the stored photon information using the existing techniques in DQDs, therefore it can be useful in quantum information processing combining the photon polarization and the electron spin.

Chapter 9

Summary and future prospects

In summary, we have developed a scheme using a gate defined GaAs DQD with a $g_e \approx 0$ QW for detecting single photoelectron spins and finally achieved the angular momentum transfer from a circularly polarized photon to an electron spin. Firstly, we characterized the g -factor several QW wafers with different well widths to derive the g vs. well width. Single and double quantum dots were fabricated on the QW structure to confirm the electronic transport and spin related phenomena associated with the g -factor. Then single photon responses were investigated in the DQDs made in these QWs. Here we developed a new technique of real-time observation of resonant inter-dot tunneling to increase the photoelectron detection accuracy compared to that previously obtained with single dots. We applied this technique together with the scheme of spin blockade to distinguish between the parallel and anti-parallel spin configuration formed by the addition of a single photoelectron to the one-electron DQD. Distinguishability of the two spin configurations was adapted to the single photoelectron trapping measurements. We measured the photoelectron spin in a finite perpendicular magnetic field and observed two distinctive signals of blocked and repeated inter-dot tunneling signals indicating detection of up and down photoelectron spins. Finally we confirmed the correctly transferred angular momentum from circularly polarized single photons to single electron by varying the circular polarization of incident photons and then observing the

cosine like curve in the measured statistics of electron spins.

To improve the fidelity of photoelectron spin detection we proposed that the Zeeman splitting of the reference single spin in the DQD must be increased. This contradicts to the need of $g_e \approx 0$ for implementing the coherent photon to spin transfer. Though, we could have the electron g -factor or Zeeman energy as large as the laser light bandwidth with keeping the LH spin split larger than the laser light bandwidth. Another option is to decrease the electron temperature by additional thermal filtering in the cryostat or further reducing the irradiation effect to reduce the probability of exciting impurity states.

The trapping efficiency of a single photon through the aperture is currently $\sim 1\%$ and this can be increased by embedding the QW in a cavity structure. By growing alternating GaAs/AlGaAs layers, a dielectric Bragg reflector can be placed underneath the 2DEG. Evaporating thin metals on the surface can act as the other side of the cavity. This could give an intensity of orders of magnitude higher at the 2DEG. Calculations of electro-magnetic field in such cavity was made for the application to QWs, but whether we can use the new structure to form QDs is still under discussion. Another merit that we could obtain from a cavity structure is that impurity states could be spatially avoided by placing the node of the resonant light on that depth.

Increasing the absorption efficiency including all the irradiated photons outside the aperture, currently $\lesssim 0.01\%$, is important for actual application for information transfer. The efficiency can be increased for instance by creating a solid immersion lens directly on top of the sample to focus the laser beam below the diffraction limit [17]. This way most of the photons could transmit through the aperture and with a cavity structure embedded we expect $\sim 10\%$ of an overall absorption efficiency in our QWs. However after the increase of photon to electron coupling can also increase excitation of the impurity states. We need the mentioned node in the cavity structure or we could ultimately use an un-doped structure that has negligible impurity states.

Once the coherent transfer is realized, we can think of various applications and additional requirements related to the photoelectron spin measurement.

To finally apply the quantum dot to a quantum repeater, entanglement creation of two photoelectron spins and subsequent Bell state measurement will be necessary. In principle the measurement here must be completed within the coherence time. The fast detection could also be preferable for the investigation of electron spin and entangled photon-spin physics. The shortest time necessary for the present photoelectron spin detection is less than $100 \mu\text{s}$, shorter than the decoherence time of 200 to $300 \mu\text{s}$ [3]. Currently we are developing a radio frequency reflectometry setup for fast charge sensing and single photon detection that can possibly be performed within a μsec .

Appendix A

g -factors in quantum dots

A.1 g -factor evaluation from Kondo effect

The Kondo effect

In order to evaluate the electron g -factor in a quantum dot, the Kondo effect in the many electron regime is investigated. We fabricated a sample of single quantum dot on a wafer N-J65. The Kondo effect in single quantum dots is expected to emerge when the tunnel coupling to the right and left leads are strong. In such a condition, we observed pairing of Coulomb peaks, which is shown in Fig. A.1(a). The enhanced conductance in the Coulomb blockade regions at $N = 21$ and $N = 23$ suggests the presence of the Kondo effect in odd number electrons with half-integer spin. The even-odd parity of the electron occupation is more conspicuous in temperature dependence of the valley conductance. For instance, conductance at the $N = 23$ Coulomb blockade region decreases with increasing temperature from 140 mK to 800 mK, while conductance at the $N = 22$ and $N = 24$ increases with increasing temperature. The conductance measured at a local minimum point in the $N = 23$ region as a function of temperature is depicted in the inset, showing a logarithmic increase with cooling electron temperature. This logarithmic behavior of valley conductance is a positive proof of the Kondo effect in this electron number

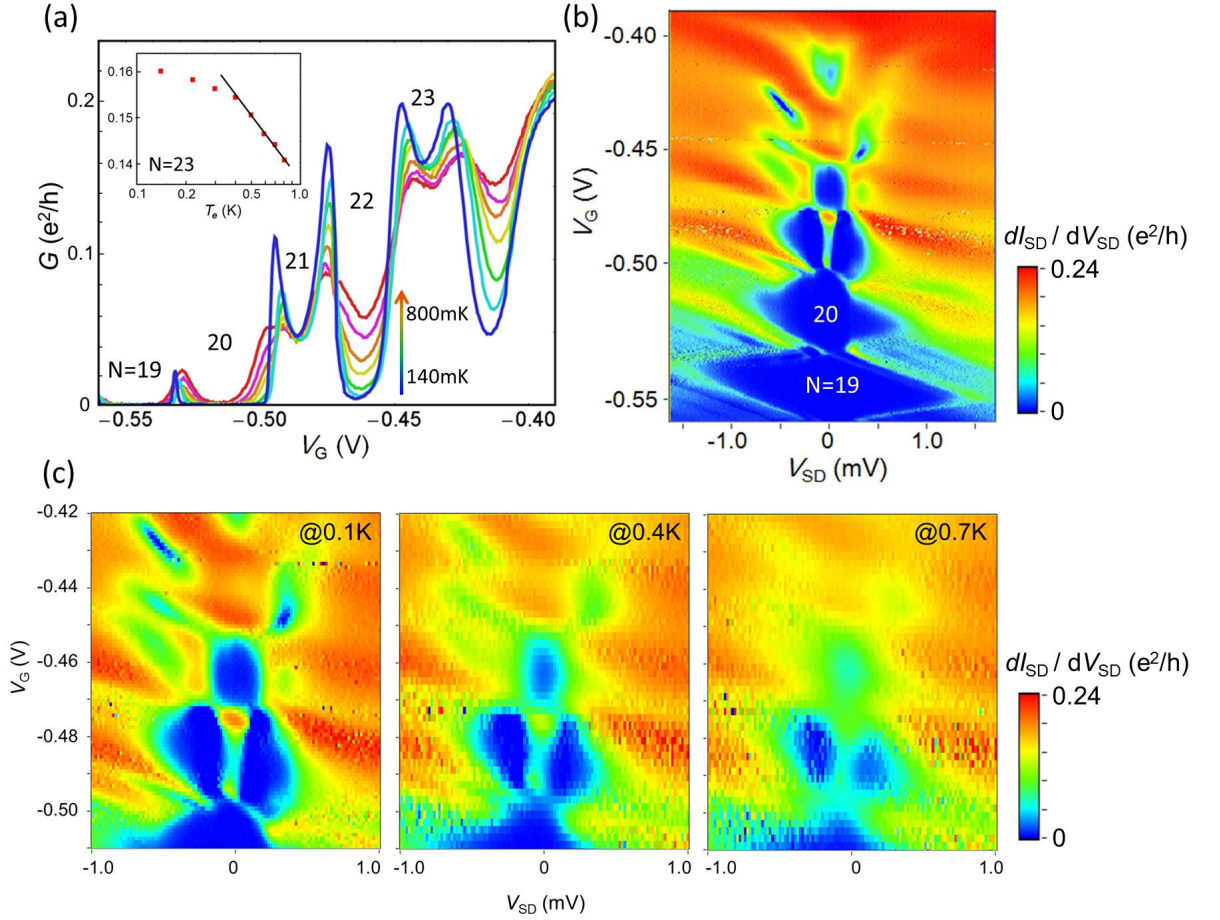


Figure A.1: (a) The temperature dependence of the Coulomb oscillations in a strong coupling regime. The even-odd parity of the electron occupation strongly indicates the existence of the Kondo effect. Inset is the differential conductance at the center of $N = 23$ valley. The black solid line indicating the logarithmic behavior of the conductance is a guide to eye. (b) The typical Coulomb diamonds measured at the same gate voltage condition as (a). (c) The detailed plots of the Coulomb diamonds at 0.1 K, 0.4 K, and 0.7 K.

regime. A similar increasing behavior of valley conductance is observed at $N = 21$, but the temperature dependence is much weaker compared to $N = 23$, seemingly due to a relatively weaker tunnel coupling to leads, leading to a lower Kondo temperature in this region.

Fig. A.1(b) is the corresponding Coulomb diamond measurement. Consis-

tent with the above Coulomb oscillation, enhancement of differential conductance is found at the center of Coulomb diamonds for $N = 21$ and $N = 23$. The observed zero-bias anomaly of differential conductance is further strong evidence of the Kondo effect. It should be mentioned that the zero-bias anomaly at $N = 23$ becomes unclear by vertical inelastic cotunneling lines at $V_{SD} = 0.2$ mV. The FWHM of the Kondo zero-bias anomaly is known to be of the order of $4k_B T_K/e$ [115]. From this expression, the Kondo temperature at $N = 21$ is estimated to be about 0.1 K, which is in good agreement with the weak temperature dependence in this electron number. Figure A.1(c) is the Coulomb diamond measured at 0.1 K, 0.4 K and 0.7 K. As temperature increases, background conductance increases and zero-bias anomalies fade.

***g*-factor evaluation in a single dot**

To confirm that the electron *g*-factor in a fabricated single quantum dot is considerably small compared to the GaAs bulk value -0.44, we investigated cotunneling spectroscopy and the Kondo effect under perpendicular and in-plane magnetic field. The Kondo peak splitting and cotunneling spectroscopy are widely used methods to measure precisely the electron *g*-factor in quantum dot systems. Systematic study of the *g*-factor evaluation methods in a few electron quantum dots is reported in Ref. [116, 117]. As shown in Fig. A.2(a), differential conductance under finite magnetic field shows a dip structure around zero-bias point of width $2g\mu_B|B|$. Inelastic spin-flip cotunneling event via the Zeeman split two levels in a quantum dot with odd electron number is allowed to occur when source-drain bias exceeds the splitting width, i.e. $e|V_{SD}| > g\mu_B|B|$. As a result, step-like structure of differential conductance is observed for both positive and negative bias, with the width of twice as much as the Zeeman splitting energy.

In detail, the step-like structure in differential conductance coming from

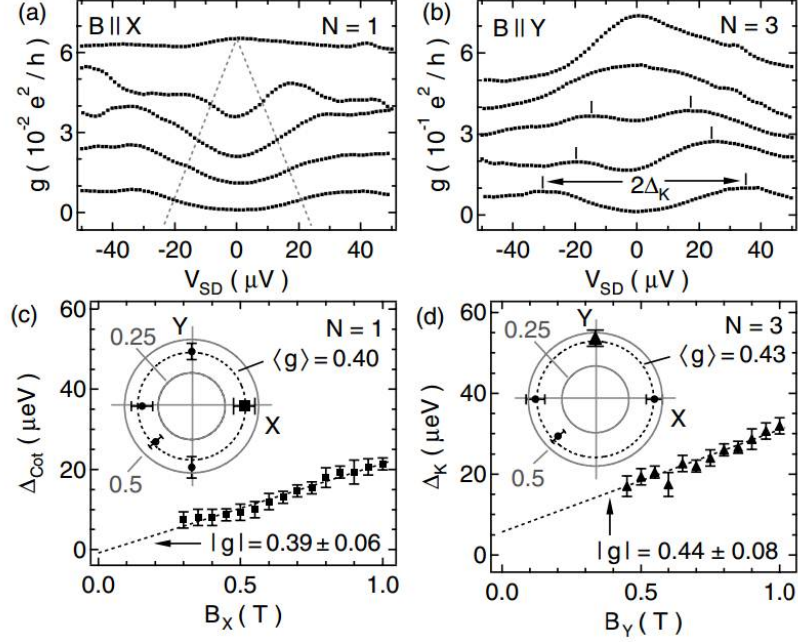


Figure A.2: (a) Differential conductance through a single quantum dot as a function of V_{SD} in the $N = 1$ diamond for in-plane fields $B_X = 0, 0.4, 0.6, 0.8, 1$ T, (top to bottom, curves offset) [116]. Dashed gray lines are guides to the eye showing the cotunneling gap. (b) A zero-bias peak in the $N = 3$ valley that splits in an in-plane field $B_Y = 0, 0.25, 0.45, 0.7, 0.95$ T (top to bottom, curves offset). (c), (d) splitting energies versus magnetic field as in (a) and (b) with linear fits. Insets: angular dependence of the g -factor in the plane of the 2DEG indicating isotropic behavior.

inelastic cotunneling is expressed by the following equation:

$$\frac{dI}{dV_{sd}} = A_e + A_i \left[F\left(\frac{eV_{sd} + \Delta}{k_B T}\right) + F\left(\frac{-eV_{sd} + \Delta}{k_B T}\right) \right], \quad (\text{A.1})$$

where A_e is the conductance from elastic cotunneling, Δ corresponds to the Zeeman splitting energy, and F is given by $F(x) = [1 + (x-1)\exp(x)]/[\exp(x)-1]^2$. The voltage difference between the center of the steps is given by $\Delta V_{sd} = 2\Delta/e$, and the temperature broadening of this step is $5.4k_B T/e$. This method is believed to achieve more precise evaluation of the electron g -factor than the conventional electron addition spectroscopy for the following two reasons. First,

the cotunneling spectrum is independent of the chemical potential of the dot, and is not affected by small charge fluctuations near the measured quantum dot. Second, resolution to probe Zeeman splitting width in this method is limited only by temperature, while that in electron addition spectroscopy method is determined by both temperature broadening and charging peak width, or coupling to the leads.

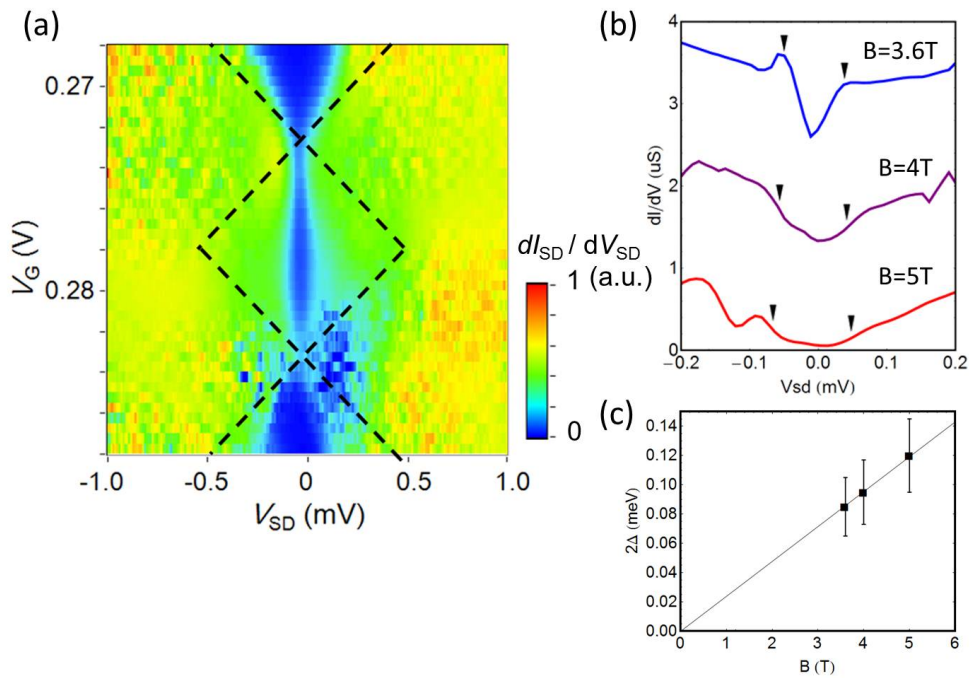


Figure A.3: (a) Typical Coulomb diamond under the perpendicular magnetic field $B = 4$ T, where the inelastic cotunneling effect is observed. (b) 1D traces of differential conductance at $B = 3.6, 4, 5$ T. As the magnetic field increased, the spacing of the step structure monotonically increased. (c) The splitting energies extracted from (b) as a function of magnetic field. Linear increase implies that the inelastic cotunneling effect arises from the Zeeman splitting of the degenerate energy levels.

Figure A.3(a) is a Coulomb diamond at $N = 25$ measured under perpendicular magnetic field $B = 4$ T. We observed a step-like structure in differential conductance, indicating the contribution from inelastic cotunneling events. The energy scale of the broadening of the step is roughly 0.05 meV, which is con-

sistent with the expected broadening width $5.4k_B T = 0.06$ meV in the experimental setup. The cotunneling curves at $B = 3.6, 4$ and 5 T are plotted in Fig. A.3(b), offset by $1 \mu\text{S}$. At $B = 3.6$ T, relics of the Kondo peak are seen at the top of the step structure, and the small peaks disappear at larger magnetic field. The energy splitting width is estimated at the marked point, assuming that the Kondo effect still exists at $B = 3.6$ T, but completely suppressed at $B = 4$ and 5 T, where only cotunneling steps are detected. The splitting widths are plotted in Fig. A.3(c) as a function of magnetic field. One can see that splitting energy is proportional to the applied magnetic field, giving a strong evidence that the observed cotunneling signals come from inelastic spin-flip cotunneling. From linear fitting, the electron g -factor for the perpendicular magnetic field is estimated to be $g_e^\perp = 0.20 \pm 0.05$, which is in good agreement with the value 0.18 deduced from electron spin resonance technique for the same wafer in Sec. 5.1.

Attention should be paid to the fact that the evaluated g -factor in a perpendicular magnetic field includes the effect of the splitting of Landau levels, resulting in the formation of edge channels. The spin split edge channels in the leads cause the asymmetry of the tunnel rate for up- and down-spins. A revolutionary idea is that in a single quantum dot with exactly zero g -factor under perpendicular magnetic field, interplay between the Kondo effect and edge states accompanied by asymmetric spin screening can be experimentally studied, while the Kondo effect is completely suppressed in such a high magnetic field in the case of conventional HEMT.

Similar measurements are performed for the in-plane magnetic field in a 0.3 K cryostat. We fabricated a different sample with a double quantum dot gate design on the same wafer N-J65 (see Fig. 5.6(c)). Again the Kondo zero-bias anomaly is observed in the Coulomb diamond measurement, and we found no splitting of the Kondo peak with the in-plane magnetic field up to 6 T. Figure A.4(a) is a Coulomb diamond at $B = 6$ T, and the corresponding zero-bias anomaly is plotted in Fig. A.4(b). The zero-bias peak has the FWHM of $130 \mu\text{eV}$. It should be noted that the Kondo effect in quantum dots under such a

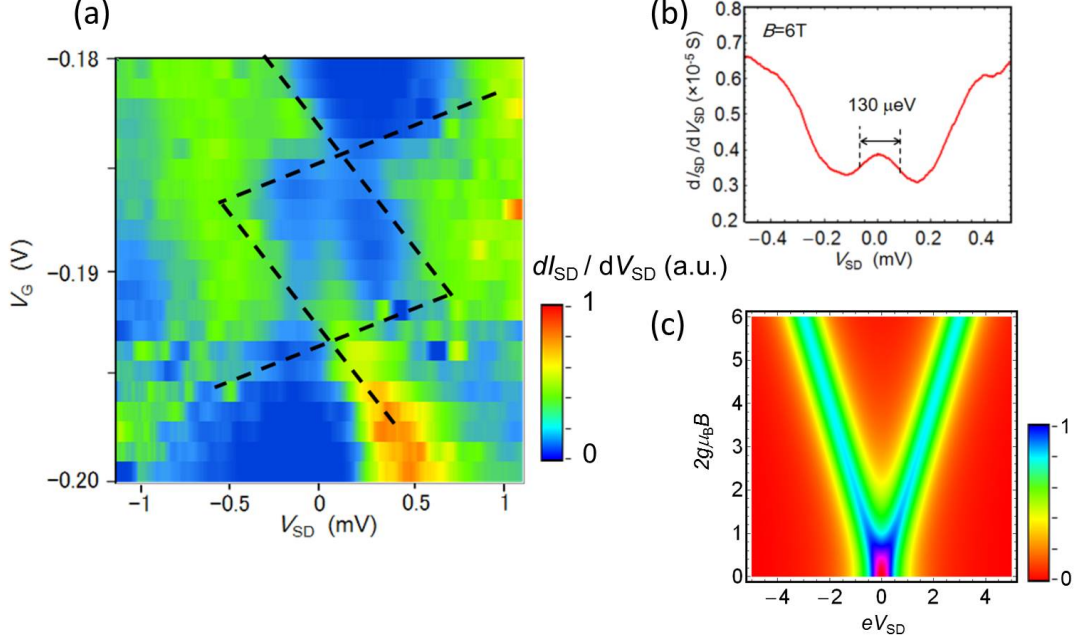


Figure A.4: (a) Typical Coulomb diamond measured under an in-plane magnetic field $B = 6$ T, where the Kondo zero-bias anomaly is observed. (b) 1D trace of the differential conductance. The absence of splitting of the zero-bias anomaly in a high magnetic field is strong evidence of the small electron g -factor. (c) Calculation result of a splitting of two identical Lorentzian peaks. The energy scales are normalized by the FWHM of the peak.

high magnetic field has not been reported so far.

From the fact that energy splitting $2g_e \mu_B B$ is within the range of observed peak width, we can determine the upper bound of the electron g -factor for the in-plane magnetic field. Figure A.4(c) shows a simulation result of the Kondo peak splitting, where we assumed the congruent Lorentzian peaks splitting by $2g_e \mu_B B$. For simplicity, the energy scale is normalized by the FWHM of the peak at $B = 0$. Two peaks start to be resolved when $2g_e \mu_B B$ exceeds 1, or the FWHM. In other words, two peaks are not resolved when $2g_e \mu_B B$ is less than the FWHM. Based on the obtained relation $2g_e \mu_B B < 130 \mu\text{eV}$, we estimated an upper bound of the electron g -factor, $|g_e^{\parallel}| < 0.19$, which is considerably small compared to the g -factor for bulk GaAs.

Note that in the above simulation the Lorentzian peak shape is assumed, but one can also deduce an upper bound of the *g*-factor relying on some preceding works. For instance, T. A. Costi [118] theoretically predicted the critical magnetic field B_c to see the splitting of the Kondo peak as $g_e\mu_B B_c = 1.06k_B T_K$ in the limit of zero-temperature. In GaAs lateral quantum dot systems, the value of B_c is deduced to be $g_e\mu_B B_c = k_B T_K$. Using the relation $\text{FWHM} = 4k_{\text{r.m.}}T_K$, we can get an even lower value of 0.10 for the upper bound of the electron *g*-factor in our system. Comparably small in-plane *g*-factor compared to the value in ESR measurement can be explained by anisotropy of the *g*-factor. In Ref. [44] the in-plane *g*-factor in a GaAs/AlGaAs quantum well with well width 7 nm is smaller than the perpendicular *g*-factor by 0.07, which gives us a prospect that the in-plane *g*-factor in our quantum well system is roughly 0.10. To obtain the upper limit of the *g*-factor more precisely, we need to focus on the Kondo effect with the considerably higher Kondo temperature compared to electron temperature, while keeping T_K smaller than the desired resolution of the peak splitting.

A.2 Nuclear spin effect in double quantum dots

The suppression of nuclear field by magnetic field is further examined. We set the voltage condition on a zero-detuning line, and probed the leakage current with sweeping magnetic field from negative to positive side. The characteristic of leakage current is significantly dependent on the sweep rate of magnetic field. With a higher sweep rate $dB/dt > 3$ mT/s, the leakage current was found unstable and hysteretic, whereas leakage current became relatively stable with lower sweep rate $dB/dt < 1$ mT/s. Typical magnetic field dependence of the leakage current with sweep rate of 1 mT/s is exhibited in Fig. A.5. A current peak is clearly observed at $B = 0$, which result from interaction between electron spin and nuclear spins as introduced above.

Noticeably, the peak width of the leakage current is broader than that measured in conventional GaAs/AlGaAs HEMT [59] with its width $\Delta B \approx 15$ mT.

We set the inter-dot tunnel coupling weaker compared to the coupling to leads. To discuss the origin of peak broadening, we fitted the experimental data with the following equation:

$$\begin{aligned}
 \langle I \rangle / e &= \Gamma_{in} S(\sqrt{3}B/B_N), \\
 S(x) &\equiv 4/x^2 - 6/x^4 + \sqrt{2\pi} \operatorname{erfi}(x/\sqrt{2})(6/x^5 - 2/x^3) \\
 &\times \exp(-x^2/2) - 3\pi \operatorname{erfi}^2(x/\sqrt{2}) \exp(-x^2)/x^6,
 \end{aligned} \tag{A.2}$$

where $\operatorname{erfi}(x)$ is the imaginary error function, Γ_{in} is the inter-dot tunnel rate, and B_N is the effective magnetic field arising from random configuration of many nuclear spins [104]. We performed fitting with three fitting parameters Γ_{in} , B_N and the constant background current C , and the curve fitted with the above equation is plotted as a black solid line in Fig. A.5, giving good agreement with the experimental result. The obtained fitting parameters are $\Gamma_{in} = 1.95 \times 10^7$

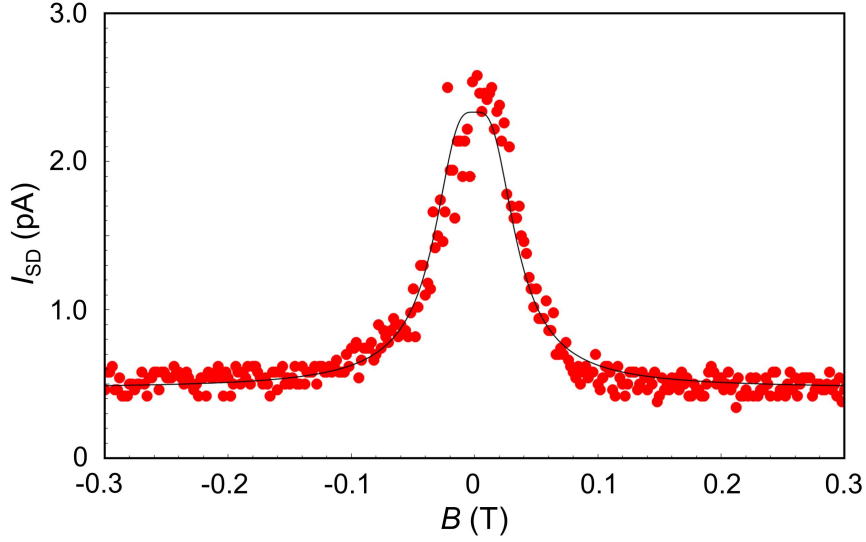


Figure A.5: The leakage current near zero-detuning line as a function of magnetic field. The current peak at $B = 0$ T is due to the mixing of the singlet and triplet states by random nuclear field fluctuation. The black solid line is the fitted curve using an equation in Ref. [104].

Hz and $B_N = 21.5$ mT. Here, we note that the effective magnetic field formed by nuclear spins is defined as follows,

$$\left(\sum_k^N A_k \mathbf{I}_k\right) \cdot \mathbf{S} = g\mu_B \mathbf{B}_N \cdot \mathbf{S}. \quad (\text{A.3})$$

When we assume that the number of nuclear spins interacting with the electron spin in our quantum well system is identical to that in the HEMT case and $(\sum_k^N A_k \mathbf{I}_k)$ is equal for both systems, the effective nuclear field B_N scales as $1/g_e$. We compared the value of B_N in our system to the value introduced in Ref. [104] for HEMT, and the estimated electron g -factor in the quantum well is 0.09 for in-plane magnetic field, which is slightly smaller than the value 0.12 for perpendicular magnetic field deduced by the ESR technique. Based on these values of the in-plane and perpendicular g -factors, the anisotropy of the electron g -factor in this system is not significant compared to the previous report, which may be due to additional electrical confinement in the 2DEG plane, since it reduces the anisotropy of confinement effect. We have to note that the energy of inter-dot coupling that came out from the fitting could be comparable with hyperfine interaction. In that case a formula for the opposite condition must be fitted, but the ones shown in Reference [104] cannot be fitted to our data before knowing the side tunnel coupling.

Appendix B

Calculation of photon absorption

The aperture diameter used in this study, which is 400 nm, is smaller than the wavelength of the incident photon, around 780 nm. Photon transmission through such small apertures should be carefully treated for the evaluation of photon absorption rates [119]. Change in shape, thickness and surface patterns could greatly influence the transmission efficiency and the polarization. The ability to modify light using nanostructured patterns leads to many useful applications for photonic devices. However, undisturbed polarization transmission is needed for accurate transfer of photon polarization information to the electron spins in QDs, while reducing unwanted irradiation outside of the QD. A circular aperture is a simple enough structure for our purpose. We have simulated light propagation to the heterostructure through a circular aperture opened on a metal mask.

FDTD calculation

A conventional simulation method of finite-difference time-domain (FDTD) method was used for the numerical analysis. FDTD modeling offers fast and reliable calculation depending on the domain size in time and space. Various dielectric and magnetic materials can be specified for the computational domains. The gridded domain must be sufficiently fine to resolve the smallest structures, but computational resource was sometimes limited for our calcula-

B. Calculation of photon absorption

tion. We finely simulated for structures near the aperture but outer structure were sometimes rough, therefore quantitative analysis in outer regions are not considered in this section. Commercial software that are specialized for optics purposes, ‘Poynting’ (Fujitsu) and ‘FDTD Solutions’ (Lumerical Solutions Inc.), were used to run the simulations.

Mask thickness dependence

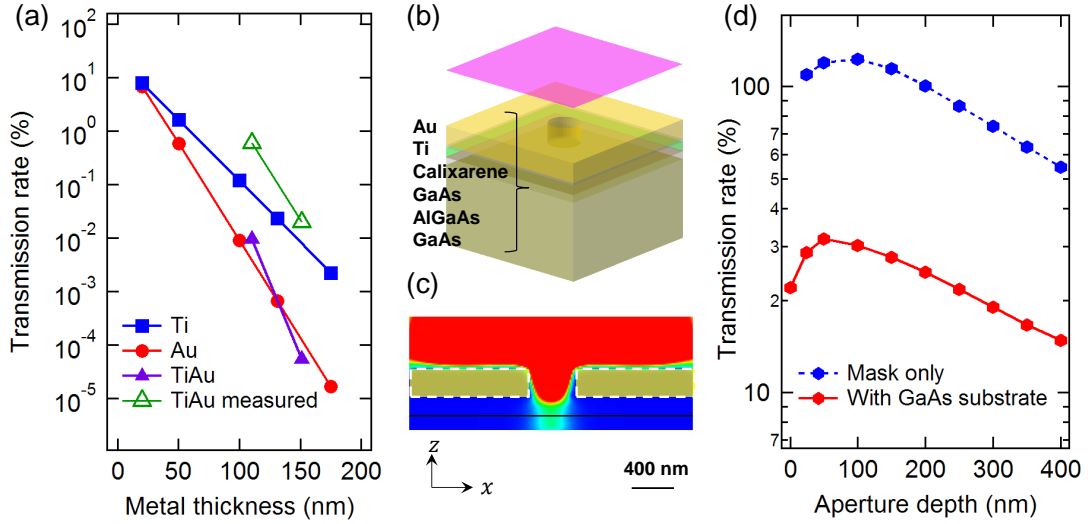


Figure B.1: (a) Plot of the transmission rate through a metal thin film. Calculation shows exponential decay whereas the measured transmission shows an additional offset. (b) Schematic of the simulated structure of a metal mask on a GaAs heterostructure. (c) An example side view plot of the calculated power at a plane including the aperture center. (d) Plot of the calculated peak transmission rate to the 2DEG. Solid line plot includes the GaAs heterostructure.

The easily tunable parameters, considering fabrication of the metal mask with a small aperture, are the thickness of the metal and the diameter of the aperture. Making the metal mask thicker increases the reflectivity of light, reducing photon propagation outside the dot with exponential behavior (Fig. B.1(a)). The measured transmission through a thin metal film showed a deviation from the calculation, however at least over 150 nm we can reduce the light

propagation by a factor of 4. However a thick metal would also decrease the light transmission through the aperture. We see how the center transmission rate of light varies with the metal thickness. Fig. B.1(b) is a picture of the calculated structure. Light propagates from the top plane and irradiated on a metal mask with a 400 nm diameter aperture. Underneath are a 120 nm Calixarene insulator (refractive index: $n = 1.56$), 5 nm GaAs capping layer ($n = 3.571$), 95 nm $\text{Al}_{0.265}\text{Ga}_{0.735}\text{As}$ layer ($n = 3.395$) and a GaAs buffer layer. The calculation was performed for a single heterostructure but it also gives a good estimate for a double heterostructure owing to the small difference in the refractive index of the AlGaAs barrier layer. We assume that the 2DEG exists at the interface of the AlGaAs and GaAs buffer layer, therefore we calculated the light intensity at 100 nm below the GaAs surface (black horizontal line in Fig. B.1(c)). We focused at the peak intensity and plotted as a function of the mask thickness or the aperture depth (Fig. B.1(d)). The initial increase of transmission around 100 nm depth may come from a resonance condition of propagation through a metal tube, inferred from the similar dependence calculated from the bare metal mask structure. The plot is followed by an exponential decay of transmission rate. A mask thickness of 250 nm gives an estimation of $\sim 25\%$ transmission through the aperture.

Aperture diameter dependence

The diameter of the aperture would give a large dependence on the transmission rate, which is estimated to be proportional to $(d/\lambda)^4$ when the aperture diameter is smaller than half of the incident wavelength ($2d < \lambda$) [120]. The power dependence holds for $d < 390$ nm in our experiments. Aiming for a higher transmission rate we simulated for a larger aperture, here with the surface gate patterns included (Fig. B.2(a)). Figure B.2(b) plots the calculated results for the peak transmission for each aperture diameter. The dashed curve is a trace proportional to $(d/\lambda)^4$, assuming that the dependence fits near the 400 nm data.

The effect of the surface fine gate patterns can be observed in the in-plane pattern of the transmitted light. Figure B.2(c) plots the light intensity from

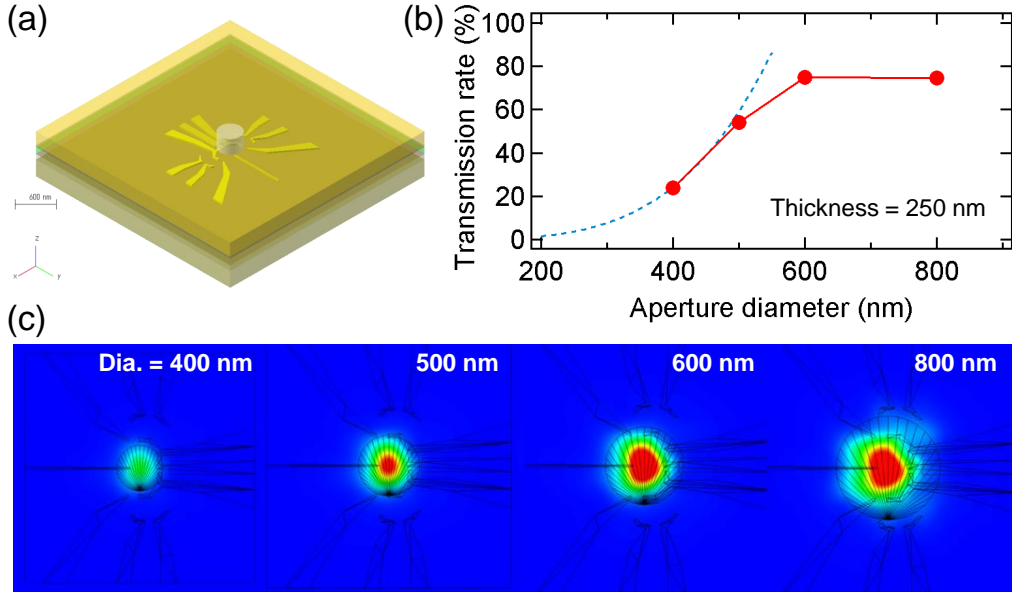


Figure B.2: (a) A picture of the simulated sample structure with fine gate patterns (thickness: 60 nm) taken into account. (b) A plot of transmission rate as a function of aperture diameter. The dashed curve is the estimated dependence of power of 4 from a theoretical formula. (c) A top view 2D plot of the light power at 100 nm below the GaAs surface. The saturation of the beam diameter is seen due to finite reflection at the surface gates.

a top view at the 2DEG depth with different aperture diameters. At 400 nm the power distribution is relatively close to the cylindrical shape of the aperture. As the aperture diameter is increased, the shape of the transmitted beam starts to differ from a circular shape. At 800 nm, although the peak intensity is maintained, the power under the gate patterns becomes lower. Here, the distribution of light intensity in the in-plane direction must be taken into account to calculate the total laser power transmission. However, the patterns in this scale could possibly vary on each fabrication process which is difficult to include in the calculation. The surface gates irradiated by a pulsed laser could also largely affect the measurements by inducing additional photoconductivity with decay time of the order of 10 ms, reducing the distinguishability of charge trapping events [30]. As a consequence, the optimal diameter of the aperture was set

between 400 nm and 500 nm for maximizing the photon collection rate while keeping the sample stable to irradiation.

References

- [1] I. Žutić, J. Fabian and S. Das Sarma, “Spintronics: Fundamentals and applications.” *Rev. Mod. Phys.* **76**, 323–410 (2004). 3
- [2] D. Loss and D. P. DiVincenzo, “Quantum computation with quantum dots.” *Phys. Rev. A* **57**, 120–126 (1998). 3
- [3] H. Bluhm, S. Foletti, I. Neder, M. Rudner, D. Mahalu, V. Umansky and A. Yacoby, “Dephasing time of GaAs electron-spin qubits coupled to a nuclear bath exceeding 200 μ s.” *Nature Physics* **7**, 109–113 (2010). 3, 117
- [4] F. H. L. Koppens, C. Buizert, K.-J. Tielrooij, I. T. Vink, K. C. Nowack, T. Meunier, L. P. Kouwenhoven and L. M. K. Vandersypen, “Driven coherent oscillations of a single electron spin in a quantum dot.” *Nature* **442**, 766–771 (2006). 3
- [5] S. Foletti, H. Bluhm, D. Mahalu, V. Umansky and A. Yacoby, “Universal quantum control of two-electron spin quantum bits using dynamic nuclear polarization.” *Nature Physics* **5**, 903–908 (2009). 3
- [6] R. Brunner, Y.-S. Shin, T. Obata, M. Pioro-Ladrière, T. Kubo, K. Yoshida, T. Taniyama, Y. Tokura and S. Tarucha, “Two-qubit gate of combined single-spin rotation and interdot spin exchange in a double quantum dot.” *Phys. Rev. Lett.* **107**, 146801 (2011). 3
- [7] M. D. Shulman, O. E. Dial, S. P. Harvey, H. Bluhm, V. Umansky and A. Yacoby, “Demonstration of entanglement of electrostatically coupled singlet-triplet qubits.” *Science* **336**, 202–205 (2012). 3
- [8] F. Meier and B. P. Zakharchenya, eds., *Optical Orientation*. (Elsevier, Amsterdam, 1984). 3, 9

REFERENCES

- [9] V. Scarani, H. Bechmann-Pasquinucci, N. J. Cerf, M. Dušek, N. Lütkenhaus and M. Peev, “The security of practical quantum key distribution.” *Rev. Mod. Phys.* **81**, 1301–1350 (2009). 3
- [10] C. H. Bennett, G. Brassard, C. Crépeau, R. Jozsa, A. Peres and W. K. Wootters, “Teleporting an unknown quantum state via dual classical and einstein-podolsky-rosen channels.” *Phys. Rev. Lett.* **70**, 1895–1899 (1993). 3
- [11] R. Vrijen and E. Yablonovitch, “A spin-coherent semiconductor photo-detector for quantum communication.” *Physica E: Low-dimensional Systems and Nanostructures* **10**, 569–575 (2001). 3, 20
- [12] R. Ursin, F. Tiefenbacher, T. Schmitt-Manderbach, H. Weier, T. Scheidl, M. Lindenthal, B. Blauensteiner, T. Jennewein, J. Perdigues, P. Trojek *et al.*, “Entanglement-based quantum communication over 144 km.” *Nature Physics* **3**, 481–486 (2007). 3
- [13] B. B. Blinov, D. L. Moehring, L.-M. Duan and C. Monroe, “Observation of entanglement between a single trapped atom and a single photon.” *Nature* **428**, 153–157 (2004). 3
- [14] J. Volz, M. Weber, D. Schlenk, W. Rosenfeld, J. Vrana, K. Saucke, C. Kurtsiefer and H. Weinfurter, “Observation of entanglement of a single photon with a trapped atom.” *Phys. Rev. Lett.* **96**, 030404 (2006). 3
- [15] T. Wilk, S. C. Webster, A. Kuhn and G. Rempe, “Single-atom single-photon quantum interface.” *Science* **317**, 488–490 (2007). 3
- [16] K. De Greve, L. Yu, P. L. McMahon, J. S. Pelc, C. M. Natarajan, N. Y. Kim, E. Abe, S. Maier, C. Schneider, M. Kamp *et al.*, “Quantum-dot spin-photon entanglement via frequency downconversion to telecom wavelength.” *Nature* **491**, 421–425 (2012). 3
- [17] W. B. Gao, P. Fallahi, E. Togan, J. Miguel-Sanchez and A. Imamoglu, “Observation of entanglement between a quantum dot spin and a single photon.” *Nature* **491**, 426–430 (2012). 3, 116
- [18] W. B. Gao, P. Fallahi, E. Togan, A. Delteil, Y. S. Chin, J. Miguel-Sanchez and A. Imamoglu, “Quantum teleportation from a propagating photon to a solid-state spin qubit.” *Nature Communications* **4**, 2744 (2013). 3

-
- [19] J. R. Schaibley, A. P. Burgers, G. A. McCracken, L.-M. Duan, P. R. Berman, D. G. Steel, A. S. Bracker, D. Gammon and L. J. Sham, “Demonstration of quantum entanglement between a single electron spin confined to an InAs quantum dot and a photon.” *Phys. Rev. Lett.* **110**, 167401 (2013). 3
- [20] E. Togan, Y. Chu, A. S. Trifonov, L. Jiang, J. Maze, L. Childress, M. V. G. Dutt, A. S. Sørensen, P. R. Hemmer, A. S. Zibrov *et al.*, “Quantum entanglement between an optical photon and a solid-state spin qubit.” *Nature* **466**, 730–734 (2010). 3
- [21] H. Bernien, L. Childress, L. Robledo, M. Markham, D. Twitchen and R. Hanson, “Two-photon quantum interference from separate nitrogen vacancy centers in diamond.” *Phys. Rev. Lett.* **108**, 043604 (2012). 3
- [22] H. Bernien, B. Hensen, W. Pfaff, G. Koolstra, M. S. Blok, L. Robledo, T. H. Taminiau, M. Markham, D. J. Twitchen, L. Childress *et al.*, “Heralded entanglement between solid-state qubits separated by three metres.” *Nature* **497**, 86–90 (2013). 3
- [23] R. Hanson, L. P. Kouwenhoven, J. R. Petta, S. Tarucha and L. M. K. Vandersypen, “Spins in few-electron quantum dots.” *Rev. Mod. Phys.* **79**, 1217–1265 (2007). 3, 27, 29
- [24] E. Yablonovitch, H. Jiang, H. Kosaka, H. D. Robinson, D. S. Rao and T. Szkopek, “Optoelectronic quantum telecommunications based on spins in semiconductors.” *Proceedings of the IEEE* **91**, 761–780 (2003). 3
- [25] H. Kosaka, H. Shigyou, Y. Mitsumori, Y. Rikitake, H. Imamura, T. Kutsuwa, K. Arai and K. Edamatsu, “Coherent transfer of light polarization to electron spins in a semiconductor.” *Phys. Rev. Lett.* **100**, 096602 (2008). 4, 22, 23
- [26] H. Kosaka, T. Inagaki, Y. Rikitake, H. Imamura, Y. Mitsumori and K. Edamatsu, “Spin state tomography of optically injected electrons in a semiconductor.” *Nature* **457**, 702–705 (2009). 4, 24
- [27] H. Kosaka, D. S. Rao, H. D. Robinson, P. Bandaru, K. Makita and E. Yablonovitch, “Single photoelectron trapping, storage, and detection in a field effect transistor.” *Phys. Rev. B* **67**, 045104 (2003). 4, 73

REFERENCES

- [28] M. Kuwahara, T. Kutsuwa, K. Ono and H. Kosaka, “Single charge detection of an electron created by a photon in a g-factor engineered quantum dot.” *Applied Physics Letters* **96**, 163107 (2010). 4, 54, 73
- [29] H.-J. Briegel, W. Dür, J. I. Cirac and P. Zoller, “Quantum repeaters: The role of imperfect local operations in quantum communication.” *Phys. Rev. Lett.* **81**, 5932–5935 (1998). 4
- [30] A. Pioda, E. Totoki, H. Kiyama, T. Fujita, G. Allison, T. Asayama, A. Oiwa and S. Tarucha, “Single-shot detection of electrons generated by individual photons in a tunable lateral quantum dot.” *Phys. Rev. Lett.* **106**, 146804 (2011). 4, 52, 73, 74, 81, 132
- [31] T. Asayama, T. Fujita, H. Kiyama, A. Oiwa and S. Tarucha, “Angular momentum transfer between a circularly polarized photon and an electron spin in double quantum dots.” *AIP Conference Proceedings* **1399**, 1009–1010 (2011). 4
- [32] R. Winkler, *Spin-orbit coupling effects in two-dimensional electron and hole systems*. (Springer, 2003). 9
- [33] S. Pfalz, R. Winkler, T. Nowitzki, D. Reuter, A. D. Wieck, D. Hägele and M. Oestreich, “Optical orientation of electron spins in GaAs quantum wells.” *Phys. Rev. B* **71**, 165305 (2005). 13
- [34] H. Kosaka, Y. Mitsumori, Y. Rikitake and H. Imamura, “Polarization transfer from photon to electron spin in g-factor engineered quantum wells.” *Applied Physics Letters* **90**, – (2007). 13
- [35] R. Winkler, “Excitons and fundamental absorption in quantum wells.” *Phys. Rev. B* **51**, 14395–14409 (1995). 13
- [36] R. C. Miller, D. A. Kleinman, W. T. Tsang and A. C. Gossard, “Observation of the excited level of excitons in GaAs quantum wells.” *Phys. Rev. B* **24**, 1134–1136 (1981). 14
- [37] J. C. Maan, G. Belle, A. Fasolino, M. Altarelli and K. Ploog, “Magneto-optical determination of exciton binding energy in GaAs-Ga_{1-x}Al_xAs quantum wells.” *Phys. Rev. B* **30**, 2253–2256 (1984). 14

-
- [38] E. E. Mendez, G. Bastard, L. L. Chang, L. Esaki, H. Morkoc and R. Fischer, “Effect of an electric field on the luminescence of GaAs quantum wells.” *Phys. Rev. B* **26**, 7101–7104 (1982). 14
- [39] M. Kroutvar, Y. Ducommun, D. Heiss, M. Bichler, D. Schuh, G. Abstreiter and J. J. Finley, “Optically programmable electron spin memory using semiconductor quantum dots.” *Nature* **432**, 81–84 (2004). 14
- [40] L. M. Roth, B. Lax and S. Zwerdling, “Theory of optical magneto-absorption effects in semiconductors.” *Phys. Rev.* **114**, 90–104 (1959). 14
- [41] C. E. Pryor and M. E. Flatté, “Landé g factors and orbital momentum quenching in semiconductor quantum dots.” *Phys. Rev. Lett.* **96**, 026804 (2006). 15
- [42] G. Lommer, F. Malcher and U. Rössler, “Reduced g factor of subband landau levels in AlGaAs/GaAs heterostructures.” *Phys. Rev. B* **32**, 6965–6967 (1985). 15
- [43] E. L. Ivchenko and A. A. Kiselev, “Electron g -factor of quantum wells and superlattices.” *Soviet physics. Semiconductors* **26**, 827–831 (1992). 15, 16
- [44] P. L. Jeune, D. Robart, X. Marie, T. Amand, M. Brousseau, J. Barrau, V. Kalevich and D. Rodichev, “Anisotropy of the electron Landé g factor in quantum wells.” *Semiconductor Science and Technology* **12**, 380 (1997). 15, 16, 61, 62, 126
- [45] M. J. Snelling, E. Blackwood, C. J. McDonagh, R. T. Harley and C. T. B. Foxon, “Exciton, heavy-hole, and electron g factors in type-I GaAs/Al _{x} Ga _{$1-x$} As quantum wells.” *Phys. Rev. B* **45**, 3922–3925 (1992). 17, 18
- [46] H. W. van Kesteren, E. C. Cosman, W. A. J. A. van der Poel and C. T. Foxon, “Fine structure of excitons in type-II GaAs/AlAs quantum wells.” *Phys. Rev. B* **41**, 5283–5292 (1990). 17
- [47] V. F. Sapega, M. Cardona, K. Ploog, E. L. Ivchenko and D. N. Mirlin, “Spin-flip Raman scattering in GaAs/Al _{x} Ga _{$1-x$} As multiple quantum wells.” *Phys. Rev. B* **45**, 4320–4326 (1992). 17

REFERENCES

- [48] X. Marie, T. Amand, P. Le Jeune, M. Paillard, P. Renucci, L. E. Golub, V. D. Dymnikov and E. L. Ivchenko, “Hole spin quantum beats in quantum-well structures.” *Phys. Rev. B* **60**, 5811–5817 (1999). 17
- [49] A. A. Kiselev, K. W. Kim and E. Yablonovitch, “In-plane light-hole g factor in strained cubic heterostructures.” *Phys. Rev. B* **64**, 125303 (2001). 18
- [50] M. Durnev, M. Glazov and E. Ivchenko, “Giant Zeeman splitting of light holes in GaAs/AlGaAs quantum wells.” *Physica E: Low-dimensional Systems and Nanostructures* **44**, 797 – 802 (2012). 18
- [51] D. M. Hofmann, K. Oettinger, A. L. Efros and B. K. Meyer, “Magnetic-circular-dichroism study of heavy- and light-hole g factors in $\text{In}_x\text{Ga}_{1-x}\text{As}/\text{InP}$ quantum wells.” *Phys. Rev. B* **55**, 9924–9928 (1997). 18
- [52] Y. H. Chen, X. L. Ye, B. Xu, Z. G. Wang and Z. Yang, “Large g factors of higher-lying excitons detected with reflectance difference spectroscopy in GaAs-based quantum wells.” *Applied Physics Letters* **89**, – (2006). 18
- [53] J. L. O’Brien, G. J. Pryde, A. G. White, T. C. Ralph and D. Branning, “Demonstration of an all-optical quantum controlled-NOT gate.” *Nature* **426**, 264–267 (2003). 18
- [54] H. J. Kimble, “The quantum internet.” *Nature* **453**, 1023–1030 (2008). 18
- [55] W. J. Munro, A. M. Stephens, S. J. Devitt, K. A. Harrison and K. Nemoto, “Quantum communication without the necessity of quantum memories.” *Nature Photonics* (2012). 18
- [56] J. S. Neergaard-Nielsen, Y. Eto, C.-W. Lee, H. Jeong and M. Sasaki, “Quantum tele-amplification with a continuous-variable superposition state.” *Nature Photonics* **7**, 439–443 (2013). 18
- [57] J. M. Elzerman, R. Hanson, J. S. Greidanus, L. H. Willems van Beveren, S. De Franceschi, L. M. K. Vandersypen, S. Tarucha and L. P. Kouwenhoven, “Few-electron quantum dot circuit with integrated charge read out.” *Phys. Rev. B* **67**, 161308 (2003). 30, 40

-
- [58] K. Ono, D. G. Austing, Y. Tokura and S. Tarucha, “Current rectification by pauli exclusion in a weakly coupled double quantum dot system.” *Science* **297**, 1313–1317 (2002). 34, 35
- [59] F. H. L. Koppens, J. A. Folk, J. M. Elzerman, R. Hanson, L. H. W. van Beveren, I. T. Vink, H. P. Tranitz, W. Wegscheider, L. P. Kouwenhoven and L. M. K. Vandersypen, “Control and detection of singlet-triplet mixing in a random nuclear field.” *Science* **309**, 1346–1350 (2005). 34, 36, 126
- [60] A. C. Johnson, J. R. Petta, C. M. Marcus, M. P. Hanson and A. C. Gosard, “Singlet-triplet spin blockade and charge sensing in a few-electron double quantum dot.” *Phys. Rev. B* **72**, 165308 (2005). 34, 37
- [61] R. J. Schoelkopf, P. Wahlgren, A. A. Kozhevnikov, P. Delsing and D. E. Prober, “The radio-frequency single-electron transistor (RF – SET): A fast and ultrasensitive electrometer.” *Science* **280**, 1238–1242 (1998). 38
- [62] B. J. van Wees, H. van Houten, C. W. J. Beenakker, J. G. Williamson, L. P. Kouwenhoven, D. van der Marel and C. T. Foxon, “Quantized conductance of point contacts in a two-dimensional electron gas.” *Phys. Rev. Lett.* **60**, 848–850 (1988). 39
- [63] C. Barthel, M. Kjærgaard, J. Medford, M. Stopa, C. M. Marcus, M. P. Hanson and A. C. Gossard, “Fast sensing of double-dot charge arrangement and spin state with a radio-frequency sensor quantum dot.” *Phys. Rev. B* **81**, 161308 (2010). 41, 65
- [64] W. Lu, Z. Ji, L. Pfeiffer, K. W. West and A. J. Rimberg, “Real-time detection of electron tunnelling in a quantum dot.” *Nature* **423**, 422–425 (2003). 41
- [65] R. Schleser, E. Ruh, T. Ihn, K. Ensslin, D. C. Driscoll and A. C. Gosard, “Time-resolved detection of individual electrons in a quantum dot.” *Applied Physics Letters* **85**, 2005–2007 (2004). 41, 42
- [66] R. Blatt and P. Zoller, “Quantum jumps in atomic systems.” *European Journal of Physics* **9**, 250 (1988). 42

REFERENCES

- [67] M. Friesen, C. Tahan, R. Joynt and M. A. Eriksson, “Spin readout and initialization in a semiconductor quantum dot.” *Phys. Rev. Lett.* **92**, 037901 (2004). 43
- [68] H.-A. Engel, V. N. Golovach, D. Loss, L. M. K. Vandersypen, J. M. Elzerman, R. Hanson and L. P. Kouwenhoven, “Measurement efficiency and n -shot readout of spin qubits.” *Phys. Rev. Lett.* **93**, 106804 (2004). 43, 48
- [69] R. Ionicioiu and A. E. Popescu, “Single-spin measurement using spin-orbital entanglement.” *New Journal of Physics* **7**, 120 (2005). 43
- [70] A. D. Greentree, A. R. Hamilton, L. C. L. Hollenberg and R. G. Clark, “Electrical readout of a spin qubit without double occupancy.” *Phys. Rev. B* **71**, 113310 (2005). 43
- [71] J. M. Elzerman, R. Hanson, L. H. W. Van Beveren, B. Witkamp, L. M. K. Vandersypen and L. P. Kouwenhoven, “Single-shot read-out of an individual electron spin in a quantum dot.” *Nature* **430**, 431–435 (2004). 43, 95, 101
- [72] E. Onac, F. Balestro, L. H. W. van Beveren, U. Hartmann, Y. V. Nazarov and L. P. Kouwenhoven, “Using a quantum dot as a high-frequency shot noise detector.” *Phys. Rev. Lett.* **96**, 176601 (2006). 44
- [73] R. Hanson, L. H. W. van Beveren, I. T. Vink, J. M. Elzerman, W. J. M. Naber, F. H. L. Koppens, L. P. Kouwenhoven and L. M. K. Vandersypen, “Single-shot readout of electron spin states in a quantum dot using spin-dependent tunnel rates.” *Phys. Rev. Lett.* **94**, 196802 (2005). 46, 47
- [74] H.-A. Engel and D. Loss, “Fermionic bell-state analyzer for spin qubits.” *Science* **309**, 586–588 (2005). 48
- [75] T. Meunier, I. T. Vink, L. H. Willems van Beveren, F. H. L. Koppens, H. P. Tranitz, W. Wegscheider, L. P. Kouwenhoven and L. M. K. Vandersypen, “Nondestructive measurement of electron spins in a quantum dot.” *Phys. Rev. B* **74**, 195303 (2006). 48

-
- [76] D. Kim, S. E. Economou, i. m. c. C. Bădescu, M. Scheibner, A. S. Bracker, M. Bashkansky, T. L. Reinecke and D. Gammon, “Optical spin initialization and nondestructive measurement in a quantum dot molecule.” *Phys. Rev. Lett.* **101**, 236804 (2008). 49
- [77] L. Robledo, L. Childress, H. Bernien, B. Hensen, P. F. A. Alkemade and R. Hanson, “High-fidelity projective read-out of a solid-state spin quantum register.” *Nature* **477**, 574–578 (2011). 49
- [78] J. R. Petta, A. C. Johnson, A. Yacoby, C. M. Marcus, M. P. Hanson and A. C. Gossard, “Pulsed-gate measurements of the singlet-triplet relaxation time in a two-electron double quantum dot.” *Phys. Rev. B* **72**, 161301 (2005). 49
- [79] C. Barthel, D. J. Reilly, C. M. Marcus, M. P. Hanson and A. C. Gossard, “Rapid single-shot measurement of a singlet-triplet qubit.” *Phys. Rev. Lett.* **103**, 160503 (2009). 49
- [80] E. Pazy, T. Calarco and P. Zoller, “Spin state readout by quantum jump technique: for the purpose of quantum computing.” *Nanotechnology, IEEE Transactions on* **3**, 10–16 (2004). 50, 95, 103
- [81] K. Morimoto, T. Fujita, G. Allison, S. Teraoka, M. Larsson, H. Kiyama, S. Haffouz, D. G. Austing, A. Ludwig, A. D. Wieck, A. Oiwa and S. Tarucha, “Single photoelectron detection after selective excitation of electron-heavy hole and electron-light hole pairs in double quantum dots.” *ArXiv e-prints* (2014). 56, 85, 86, 92
- [82] S. Teraoka, A. Numata, S. Amaha, K. Ono and S. Tarucha, “Electron spin resonance and nuclear spin pumping in 2DEG quantum Hall system.” *Physica E: Low-dimensional Systems and Nanostructures* **21**, 928 – 932 (2004). 57, 61
- [83] R. J. Nicholas, R. J. Haug, K. v. Klitzing and G. Weimann, “Exchange enhancement of the spin splitting in a GaAs – Ga_xAl_{1-x}As heterojunction.” *Phys. Rev. B* **37**, 1294–1302 (1988). 59
- [84] M. Dobers, K. v. Klitzing and G. Weimann, “Electron-spin resonance in the two-dimensional electron gas of GaAs – Al_xGa_{1-x}As heterostructures.” *Phys. Rev. B* **38**, 5453–5456 (1988). 61

REFERENCES

- [85] M. Pioro-Ladrière, J. H. Davies, A. R. Long, A. S. Sachrajda, L. Gaudreau, P. Zawadzki, J. Lapointe, J. Gupta, Z. Wasilewski and S. Studenikin, “Origin of switching noise in GaAs/Al_xGa_{1-x}As lateral gated devices.” *Phys. Rev. B* **72**, 115331 (2005). 65
- [86] C. Buizert, F. H. L. Koppens, M. Pioro-Ladrière, H.-P. Tranitz, I. T. Vink, S. Tarucha, W. Wegscheider and L. M. K. Vandersypen, “*InSitu* reduction of charge noise in GaAs/Al_xGa_{1-x}As schottky-gated devices.” *Phys. Rev. Lett.* **101**, 226603 (2008). 65
- [87] D. J. Chadi and K. J. Chang, “Energetics of DX-center formation in GaAs and Al_xGa_{1-x}As alloys.” *Phys. Rev. B* **39**, 10063–10074 (1989). 69
- [88] L. X. He, K. P. Martin and R. J. Higgins, “Infrared quenching of persistent photoconductivity in GaAs/Al_xGa_{1-x}As heterostructures.” *Phys. Rev. B* **39**, 1808–1818 (1989). 69
- [89] D. S. Rao, T. Szkopek, H. D. Robinson, E. Yablonovitch and H.-W. Jiang, “Single photoelectron trapping, storage, and detection in a one-electron quantum dot.” *Journal of Applied Physics* **98**, 114507 (2005). 73
- [90] A. Schmeller, W. Hansen, J. P. Kotthaus, G. Tränkle and G. Weimann, “Franz–Keldysh effect in a twodimensional system.” *Applied Physics Letters* **64**, 330–332 (1994). 74
- [91] H. P. Hjalmarson and T. J. Drummond, “Deep donor model for the persistent photoconductivity effect.” *Applied physics letters* **48**, 656–658 (1986). 83
- [92] P. M. Mooney, “Deep donor levels (DX centers) in III-V semiconductors.” *Journal of applied physics* **67**, R1–R26 (1990). 83
- [93] E. S. Koteles and J. Y. Chi, “Experimental exciton binding energies in GaAs/Al_xGa_{1-x}As quantum wells as a function of well width.” *Phys. Rev. B* **37**, 6332–6335 (1988). 85
- [94] D. A. Broido, E. S. Koteles, C. Jagannath and J. Y. Chi, “Resonance broadening of the light-hole exciton in GaAs/Al_xGa_{1-x}As quantum wells.” *Phys. Rev. B* **37**, 2725–2728 (1988). 85, 86

-
- [95] L. Viña, R. T. Collins, E. E. Mendez and W. I. Wang, “Excitonic coupling in GaAs/GaAlAs quantum wells in an electric field.” *Phys. Rev. Lett.* **58**, 832–835 (1987). 86
- [96] D. A. B. Miller, D. S. Chemla, T. C. Damen, A. C. Gossard, W. Wiegmann, T. H. Wood and C. A. Burrus, “Electric field dependence of optical absorption near the band gap of quantum-well structures.” *Phys. Rev. B* **32**, 1043–1060 (1985). 86
- [97] K. Brunner, U. Bockelmann, G. Abstreiter, M. Walther, G. Böhm, G. Tränkle and G. Weimann, “Photoluminescence from a single GaAs/AlGaAs quantum dot.” *Phys. Rev. Lett.* **69**, 3216–3219 (1992). 86
- [98] L. Pavesi and M. Guzzi, “Photoluminescence of $\text{Al}_x\text{Ga}_{1-x}\text{As}$ alloys.” *Journal of Applied Physics* **75**, 4779–4842 (1994). 87
- [99] K. MacLean, S. Amasha, I. P. Radu, D. M. Zumbühl, M. A. Kastner, M. P. Hanson and A. C. Gossard, “Energy-dependent tunneling in a quantum dot.” *Phys. Rev. Lett.* **98**, 036802 (2007). 91
- [100] T. Fujisawa, T. Hayashi, R. Tomita and Y. Hirayama, “Bidirectional counting of single electrons.” *Science* **312**, 1634–1636 (2006). 92
- [101] D. Harbusch, D. Taubert, H. P. Tranitz, W. Wegscheider and S. Ludwig, “Phonon-mediated versus coulombic backaction in quantum dot circuits.” *Phys. Rev. Lett.* **104**, 196801 (2010). 92
- [102] U. Gasser, S. Gustavsson, B. Küng, K. Ensslin and T. Ihn, “Phonon-mediated back-action of a charge readout on a double quantum dot.” *Nanotechnology* **21**, 274003 (2010). 92
- [103] Y. Utsumi, D. S. Golubev, M. Marthaler, K. Saito, T. Fujisawa and G. Schön, “Bidirectional single-electron counting and the fluctuation theorem.” *Phys. Rev. B* **81**, 125331 (2010). 92
- [104] O. N. Jouravlev and Y. V. Nazarov, “Electron transport in a double quantum dot governed by a nuclear magnetic field.” *Phys. Rev. Lett.* **96**, 176804 (2006). 93, 127, 128
- [105] T. Sauter, W. Neuhauser, R. Blatt and P. E. Toschek, “Observation of quantum jumps.” *Phys. Rev. Lett.* **57**, 1696–1698 (1986). 95

REFERENCES

- [106] P. Zoller, M. Marte and D. F. Walls, “Quantum jumps in atomic systems.” *Phys. Rev. A* **35**, 198–207 (1987). 95
- [107] A. N. Vamivakas, C.-Y. Lu, C. Matthiesen, Y. Zhao, S. Fält, A. Badolato and M. Atatüre, “Observation of spin-dependent quantum jumps via quantum dot resonance fluorescence.” *Nature* **467**, 297–300 (2010). 95, 103
- [108] J. M. Taylor, J. R. Petta, A. C. Johnson, A. Yacoby, C. M. Marcus and M. D. Lukin, “Relaxation, dephasing, and quantum control of electron spins in double quantum dots.” *Phys. Rev. B* **76**, 035315 (2007). 95
- [109] Y. Yuzhelevski, M. Yuzhelevski and G. Jung, “Random telegraph noise analysis in time domain.” *Review of Scientific Instruments* **71**, 1681–1688 (2000). 96
- [110] A. C. Johnson, J. R. Petta, J. M. Taylor, A. Yacoby, M. D. Lukin, C. M. Marcus, M. P. Hanson and A. C. Gossard, “Triplet-singlet spin relaxation via nuclei in a double quantum dot.” *Nature* **435**, 925–928 (2005). 99, 100
- [111] P. Stano *Private discussion* 100
- [112] D. M. Zumbühl, J. B. Miller, C. M. Marcus, K. Campman and A. C. Gossard, “Spin-orbit coupling, antilocalization, and parallel magnetic fields in quantum dots.” *Phys. Rev. Lett.* **89**, 276803 (2002). 100
- [113] K. C. Nowack, F. H. L. Koppens, Y. V. Nazarov and L. M. K. Vandersypen, “Coherent control of a single electron spin with electric fields.” *Science* **318**, 1430–1433 (2007). 101
- [114] V. Srinivasa, K. C. Nowack, M. Shafiei, L. M. K. Vandersypen and J. M. Taylor, “Simultaneous spin-charge relaxation in double quantum dots.” *Phys. Rev. Lett.* **110**, 196803 (2013). 112
- [115] A. V. Kretinin, H. Shtrikman, D. Goldhaber-Gordon, M. Hanl, A. Weichselbaum, J. von Delft, T. Costi and D. Mahalu, “Spin-1/2 Kondo effect in an InAs nanowire quantum dot: Unitary limit, conductance scaling, and Zeeman splitting.” *Phys. Rev. B* **84**, 245316 (2011). 121

- [116] D. M. Zumbühl, C. M. Marcus, M. P. Hanson and A. C. Gossard, “Co-tunneling spectroscopy in few-electron quantum dots.” *Phys. Rev. Lett.* **93**, 256801 (2004). 121, 122
- [117] A. Kogan, S. Amasha, D. Goldhaber-Gordon, G. Granger, M. A. Kastner and H. Shtrikman, “Measurements of Kondo and spin splitting in single-electron transistors.” *Phys. Rev. Lett.* **93**, 166602 (2004). 121
- [118] T. A. Costi, “Kondo effect in a magnetic field and the magnetoresistivity of Kondo alloys.” *Phys. Rev. Lett.* **85**, 1504–1507 (2000). 126
- [119] C. Genet and T. W. Ebbesen, “Light in tiny holes.” *Nature* **445**, 39–46 (2007). 129
- [120] A. Degiron, H. Lezec, N. Yamamoto and T. Ebbesen, “Optical transmission properties of a single subwavelength aperture in a real metal.” *Optics Communications* **239**, 61 – 66 (2004). 131